Atomistic Simulation of Solid- and Liquid-Phase Redox Processes in Iron–Oxygen System

Zur Erlangung des akademischen Grades eines

DOKTORS DER NATURWISSENSCHAFTEN

(Dr. rer. nat.)

von der KIT-Fakultät für Chemie und Biowissenschaften

des Karlsruher Instituts für Technologie (KIT)

genehmigte

DISSERTATION

von

M.Sc. Aleksandr Maliugin

Tag der mündlichen Prüfung:	22.04.2026
1. Referent:	Prof. Dr. Felix Studt
2. Referent:	Prof. Dr. Olaf Deutschmann

Kurzfassung

Die effiziente Nutzung von Energieressourcen gewinnt heutzutage zunehmend an Bedeutung. Die Verbrennung fossiler Brennstoffe ist nach wie vor die am leichtesten zugängliche Energiequelle, doch ihre Nutzung verschärft die Umweltprobleme weiter. Daher besteht ein dringender Bedarf an alternativen Ansätzen. Die Entwicklung alternativer Energiequellen hat sich zu einem der vielversprechendsten und wichtigsten Bereiche in Wissenschaft und Technik entwickelt.

Diese Arbeit präsentiert theoretische Ansätze zur Beschreibung der Oxidation von Eisen und der Reduktion seiner Oxide. Das Hauptziel ist die Entwicklung einer konsistenten Methodik, die sowohl qualitative als auch quantitative Einblicke in Redoxprozesse im Fe-O-System im festen und flüssigen Zustand ermöglicht. Zu diesem Zweck kombiniert die Studie moderne Methoden der statistischen Physik und der Festkörperphysik, um thermodynamische (Wärmekapazität, Enthalpie, Gibbs-Energie) und kinetische Eigenschaften (Diffusionskoeffizienten, Viskosität, Wärmeleitfähigkeit) zu berechnen. Darüber hinaus werden Molekulardynamiksimulationen auf Basis maschinell gelernter interatomarer Potenziale in die Forschung einbezogen, wodurch die zugänglichen Längen- und Zeitskalen deutlich über die rechenintensiven Ab-initio-Berechnungen hinaus erweitert werden.

Um die Genauigkeit der Ab-initio-Methoden zu validieren, werden die thermodynamischen Funktionen von Eisen und seinen Oxiden berechnet und mit experimentellen Referenzdaten verglichen, wobei eine gute Übereinstimmung erzielt wird. Diese Daten werden anschließend verwendet, um Phasengleichgewichtsdiagramme für das Fe-O-System unter oxidierenden und reduzierenden Bedingungen zu erstellen. Es wird angenommen, dass ein durch Leerstellen vermittelter Diffusionsmechanismus (Schottky-Typ) den Stofftransport in Eisenoxiden während Redoxreaktionen bestimmt. Daher werden die Abhängigkeiten der Leerstellenkonzentration von der Temperatur und dem chemischen Potenzial für jedes der Eisenoxide berechnet. Schließlich werden alle relevanten Migrationswege berücksichtigt und die entsprechenden Übergangszustände und Aktivierungsbarrieren berechnet, um Diffusionsprozesse zu beschreiben. Die resultierenden kinetischen Parameter werden im Kinetic Monte Carlo (KMC)-Code verwendet, der zur Berechnung der Diffusionskoeffizienten von Eisen und Sauerstoff und zur Abschätzung der Oxidationsgeschwindigkeitskonstanten im Rahmen der Wagner-Theorie eingesetzt wird.

Die Untersuchung elementarer Oberflächenprozesse liefert Einblicke in das Adsorptionsverhalten von Wasserstoff- und Sauerstoffspezies auf Eisen- und Fe_2O_3-Oberflächen. Mithilfe von Ab-initio-Berechnungen werden die quantitativen Adsorptionseigenschaften bestimmt und der Bildungsmechanismus des Wassermoleküls auf der Fe_2O_3 (0001)-Oberfläche betrachtet. Darüber hinaus wird das Verhalten von Wasserstoff und Wasser in Zwischengitterplätzen von Fe_2O_3 untersucht, um die Durchführbarkeit eines Reduktionswegs im Volumen zu bewerten.

Für das flüssige Fe-O-System erwies sich die DFT-basierte Molekulardynamik als rechentechnisch nicht realisierbar, was die Entwicklung eines hochgenaues interatomaren Potentials motivierte, das auf DFT-Referenzdaten für groß angelegte Simulationen basiert. Mithilfe von Molekulardynamik und dem trainierten Potential wurde die Mischungslücke in flüssigem Fe-O analysiert. Dies umfasste die Bestimmung der Löslichkeitsgrenzen sowie die Bewertung der thermodynamischen und Transport-Eigenschaften der koexistierenden Flüssigkeiten L_1 und L_2. Abschließend wurde die Oxidation einer Eisenplatte und eines flüssigen Eisen-Nanopartikels unter Sauerstoffffluss simuliert. Die so gewonnenen atomistischen Trajektorien ermöglichten die Beurteilung der Oxidationsmorphologie und der Entstehung von Hochtemperatur-Clustern.

Abstract

The rational use of energy resources becomes increasingly important nowadays. The combustion of fossil fuels remains the most accessible energy source, yet its utilisation continues to deepen environmental problems. Therefore, there is an urgent need for other approaches. The development of alternative energy sources has become one of the most promising and significant areas in science and technology.

The work presents theoretical approaches to describe the oxidation of iron and the reduction of its oxides. The primary aim is to develop a consistent methodology that provides both qualitative and quantitative insight into redox processes in the Fe–O system in solid and liquid states. For this purpose, the study merges modern methods of statistical physics and solid-state physics to compute thermodynamic (heat capacity, enthalpy, Gibbs free energy) and kinetic properties (diffusion coefficients, viscosity, thermal conductivity). In addition, molecular dynamics simulations based on machine-learned interatomic potentials are involved in the research, substantially extending the accessible size and time scales beyond computationally demanding first-principles calculations.

In order to validate the accuracy of the *ab initio* approaches, the thermodynamic functions of iron and its oxides are calculated and compared with experimental reference data, yielding good agreement. Further, these data are used to construct phase-equilibrium diagrams for the Fe–O system under oxidising and reducing conditions. A vacancy-mediated diffusion mechanism (Schottky-type) is assumed to govern mass transport in iron oxides during redox reactions. Therefore, the dependences of the vacancy concentration with respect to the temperature and chemical potential are calculated for each of the iron oxides. Finally, all relevant migration pathways are considered and the corresponding transition states and activation barriers are calculated to describe diffusion processes. The resulting kinetic parameters are used with the Kinetic Monte Carlo (KMC) algorithm, which is applied to compute the diffusion coefficients of iron and oxygen in iron oxides and then the oxidation rate constants are estimated within the Wagner theory.

An investigation of elementary surface processes provides insight into the adsorption behaviour of hydrogen and oxygen species on iron and Fe_2O_3 surfaces. Using first-principles calculations, the quantitative adsorption characteristics are determined, and the mechanism of formation of the water molecule on the Fe_2O_3 (0001) surface is considered. In addition, the behaviour of

hydrogen and water in interstitial sites of Fe_2O_3 is explored to assess the feasibility of a bulk reduction pathway.

For the liquid Fe–O system, DFT-based molecular dynamics was found to be computationally prohibitive, motivating the development of a high-accuracy interatomic potential trained on DFT reference data for large-scale simulations. Using molecular dynamics with the trained potential, the immiscibility gap in liquid Fe–O was estimated, including the determination of miscibility limits and the calculation of the thermodynamic and transport properties of the coexisting liquids L_1 and L_2. Finally, oxidation of an iron slab and a liquid iron nanoparticle was simulated under oxygen flux, providing atomistic trajectories for assessing oxidation morphology.

Contents

Kurzfassung . . . . . **i**

Abstract . . . . . **iii**

Acronyms and symbols . . . . . **ix**

1 Introduction **1**
1.1 Motivation 1
1.2 Iron as a promising energy carrier 3
1.3 Physical and chemical properties 4
1.3.1 Iron 4
1.3.2 Wüstite 6
1.3.3 Magnetite 8
1.3.4 Hematite 10
1.4 Scope of this work 12

2 Computational methods **15**
2.1 Electronic Structure Therory 15
2.1.1 Hohenberg–Kohn Theorems 15
2.1.2 Kohn–Sham Equations 16
2.1.3 Bloch Theorem 18
2.1.4 Plane-Wave Basis Set 19
2.1.5 Pseudopotential Method 20
2.1.6 Exchange–Correlation Functionals 22
2.1.7 Hubbard correction 29
2.2 Statistical Mechanics 31
2.2.1 Quantum Molecular Dynamics 32
2.2.2 Monte Carlo method 33
2.2.3 Quasi-Harmonic Approximation 36
2.2.4 Moment Tensor Potential 38
2.2.5 Linear responce theory 40
2.2.6 Two-Phase Thermodynamics 43

3 Thermodynamic properties of iron and iron oxides . . . 47
3.1 Introduction . . . 47
3.2 Methodology . . . 47
3.2.1 DFT calculations . . . 47
3.2.2 Thermodynamic properties . . . 48
3.3 Results . . . 50
3.4 Conclusions . . . 58

4 Diffusion phenomena in iron and iron oxides . . . 61
4.1 Introduction . . . 61
4.2 Methodology . . . 61
4.3 Results . . . 62
4.3.1 Calculation of vacancy concentration . . . 62
4.3.2 KMC simulations of diffusion coefficients . . . 64
4.3.3 Diffusion coefficient . . . 67
4.3.4 Oxidation rate constants . . . 70
4.4 Conclusions . . . 72

5 Diffusion and adsorption of hydrogen and oxygen on iron . . . 75
5.1 Introduction . . . 75
5.2 Methodology . . . 75
5.3 Results . . . 76
5.3.1 Adsorption onto (110) iron surface . . . 76
5.3.2 Diffusion in iron . . . 77
5.3.3 Generalized coordination number . . . 78
5.4 Conclusions . . . 81

6 Reduction of hematite using hydrogen . . . 83
6.1 Introduction . . . 83
6.2 Methodology . . . 84
6.3 Results . . . 84
6.3.1 Formation of water on the surface of hematite . . . 84
6.3.2 Diffusion of hydrogen and water in hematite . . . 87
6.4 Conclusions . . . 88

7 Thermodynamic and transport properties of the liquid Fe-O system . . . 91
7.1 Introduction . . . 91
7.2 Methodology . . . 92
7.3 Results . . . 92
7.3.1 Simulation within DFT-MD . . . 92
7.3.2 Training MLIP . . . 97

7.3.3 Thermodynamic properties . . . 99
7.3.4 Transport properties . . . 101
7.3.5 Immiscibility gap . . . 103
7.4 Conclusions . . . 106

8 Molecular dynamics study of iron oxidation . . . 109
8.1 Introduction . . . 109
8.2 Results . . . 110
8.2.1 Mass and Thermal accommodation coefficients . . . 110
8.2.2 Oxidation of iron slab . . . 111
8.2.3 Oxidation of iron nanoparticle . . . 111
8.3 Conclusions . . . 114

9 Simulation of the liquid In-Me slab using machine learning force field . . . 117
9.1 Introduction . . . 117
9.2 Methodology . . . 119
9.2.1 MLFF training . . . 120
9.3 Results . . . 121
9.3.1 Analysis of the position of the catalytically active center . . . 121
9.3.2 Coordination number (CN) analysis . . . 123
9.3.3 Adsorption on the liquid surface . . . 123
9.4 Conclusions . . . 125

10 Summary and Outlook . . . 127

11 Appendix . . . 131
11.1 Phase diagrams under oxidizing and reducing conditions in solid and gas phases . . . 131
11.2 Migration pathways of iron atoms in Fe_3O_4 . . . 132
11.3 Oxidation of iron nanoparticle . . . 132
11.4 Oxidation of iron slab . . . 132

List of Figures . . . 139

List of Tables . . . 147

List of Publications . . . 149
Journal articles . . . 149
Conference contributions . . . 149

Bibliography . . . 151

Acronyms and symbols

Acronyms

DFT	Density Functional Theory
MD	Classical Molecular Dynamics
QMD	Quantum Molecular Dynamics
KMC	Kinetic Monte Carlo
MLIP	Machine Learning Interatomic Potential
MTP	Moment Tensor Potential
VASP	Vienna Ab initio Simulation Package
LAMMPS	Large-scale Atomic/Molecular Massively Parallel Simulator
QHA	Quasi-harmonic approximation
MSD	Mean squared displacements
2PT	Two-phase thermodynamics
VACF	Velocity autocorrelation function
VDOS	Vibrational density of states
DFPT	Density Functional Perturbation Theory
NEB	Nudged Elastic Band method

Constants

π	Pi: $3{,}14159\ldots$
k_B	Boltzmann constant: $1{,}38065\ldots \times 10^{-23}\mathrm{J}\cdot\mathrm{K}^{-1} = 8{,}61733 \times 10^{-5}\mathrm{eV}\cdot\mathrm{K}^{-1}$

R	Molar gas constant: $8{,}31446\ldots\,\mathrm{J}\cdot\mathrm{K}^{-1}\cdot\mathrm{mol}^{-1}$
h	Planck constant: $6{,}62607\ldots\times10^{-34}\,\mathrm{J}\cdot\mathrm{s}$
$\hbar$	Reduced Planck constant: $1{,}05457\ldots\times10^{-34}\,\mathrm{J}\cdot\mathrm{s}$

Symbols and variables

$n(\mathbf{r})$	Density of electrons (or n)
$\omega_{\mathbf{q}i}$	Angular frequency of the i-th phonon mode at wave vector $\mathbf{q}$
μ_m	Magnetic moment of an atom
V	Total volume of a system
Ω	Volume of a unit cell
E	Internal energy
F	Helmholtz free energy
G	Gibbs free energy
S	Entropy
C_v	Heat capacity at constant volume
C_p	Heat capacity at constant pressure
C_m	Magnetic contribution to heat capacity
μ_i	Chemical potential of species i
D_i	Diffusion coefficient of species i
$C_{\mathrm{vac},i}$	Vacancy concentration of species i
ν_{att}	Attempt frequency
E_{a}	Activation energy (barrier)
a_i	Chemical activity of species i

1 Introduction

1.1 Motivation

At present, the issue of the utilisation of energy resources is becoming increasingly critical. The development of efficient and safe energy generation technologies represents one of the highest priorities of modern science and engineering. Although fossil fuel combustion remains the most accessible source of energy, it is far from ecologically benign. Excessive and poorly regulated exploitation of fossil fuels has significant adverse consequences, mainly associated with emissions of carbon dioxide, methane, and other greenhouse gases, which cause climate change and global warming.

In response to these challenges, in 2015, the leaders of 196 countries adopted the Paris Agreement, committing to limit the global average temperature increase to 1.5 °C above pre-industrial levels over the course of the current century.[1] However, assessments based on the current state of the global industry indicate a projected temperature increase of approximately 2.5 to 3 °C. Therefore, to achieve the stated climate targets, a gradual transition from fossil energy sources to clean and renewable alternatives that do not adversely affect the environment or the global climate system is required.

In general, a substantial fraction of current energy production based on coal and natural gas can be replaced by renewable energy sources such as wind and solar power. The generation of solar and wind energy is strongly governed by the geographical and climatic conditions of a given region, including the level of solar irradiance, the average wind speed, and their seasonal variability. As a consequence, the efficiency and stability of power generation are significantly dependent on the location of the power plants, leading to spatially heterogeneous electricity production. This location dependence requires the development of extended electrical transmission networks and balancing systems to enable the effective integration of renewable energy sources into a unified power system.[2,3]

Classic energy storage technologies, such as mechanical storage and pumped hydroelectric power plants, are limited in scalability and cannot efficiently provide energy storage at the terawatt-hour scale required for energy systems with a high share of renewable sources. In particular, Stadler

and Sterner[4] emphasise that chemical forms of energy storage, characterised by high energy density and the ability to store long-term and seasonal, are fundamentally more promising to balance renewable generation. The use of chemical energy carriers, including materials capable of reversible redox reactions, is therefore considered a key component of future sustainable energy systems.

In the works of Julien[5] and Bergthorson,[5,6] a systematic analysis of various metals as potential energy carriers for future sustainable energy systems is presented. The authors formulate key requirements for such materials, including high energy density, stability of the reduced state during long-term storage, and the ability to be safely transported over long distances. Particular emphasis is placed on volumetric energy density, as it directly affects storage efficiency and logistics and represents one of the major limitations of hydrogen and hydrogen-based energy carriers. It is demonstrated that metallic energy carriers can substantially reduce the requirements for storage volume and transport infrastructure. Furthermore, the importance of material abundance and recyclability is highlighted to guarantee the sustainability and scalability of the energy cycle. Similar conclusions regarding the prospects of metals as chemical energy carriers are also supported by the review by Rivard[7] and co-workers, which discusses materials and technologies for energy storage based on solid chemical carriers.

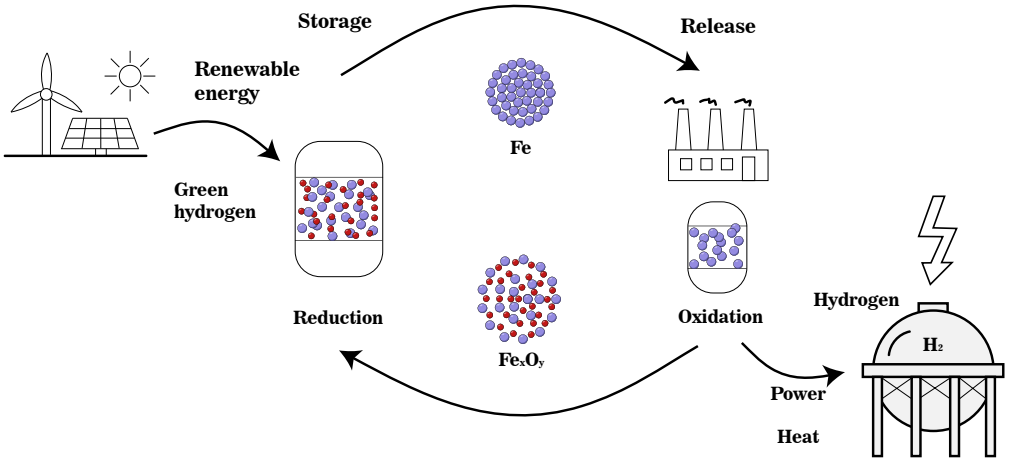

Figure 1.1: Principle of a metal fuel cycle for energy storage and conversion based on iron. Energy is released through the oxidation of iron particles, and the generated heat can be used directly or converted into electricity. The energy carrier is regenerated via reduction with hydrogen produced by water electrolysis or other CO_2-free energy sources. The reduced particles are stored for subsequent use, thereby closing the cycle.[8]

Conceptually, the idea of using metals as energy carriers is based on the release of energy during the oxidation process (i.e., combustion), followed by the regeneration of the metal through a reduction step, after which the reduced metal is stored for subsequent use. This metal–oxide

redox cycle can be organised in a closed-loop and continuous manner, as schematically illustrated in the Figure 1.1. In practical applications, hydrogen is most commonly used as the reducing agent; it may be supplied as a byproduct of another technological process or generated locally, for instance via water electrolysis. Oxidation can be performed using either ambient air or water vapour; in the latter case, hydrogen is produced as a co-product and can subsequently be used for reduction. Recent studies have demonstrated that such metal-based energy cycles can be realised in fluidised-bed and particle-based reactor concepts, offering high-efficiency heat and mass transfer as well as scalability to industrially relevant power levels.[9] Importantly, when hydrogen is produced from free carbon technology, the overall cycle does not involve net greenhouse gas emissions, making metal-based energy carriers a promising option for the storage and conversion of sustainable and carbon-neutral energy.[10,11] The iron powder obtained after the recycling process can subsequently be stored and transported to locations with high energy demand.

1.2 Iron as a promising energy carrier

For large-scale deployment of metals as energy carriers, three candidates are most commonly considered: silicon, aluminium, and iron. Silicon exhibits a high volumetric energy density of approximately 20.8 kWh L^{-1}; however, its practical use is limited by the fact that silicon particles cannot be fully reduced by hydrogen to elemental silicon, but only to silicon monoxide, which significantly reduces the overall efficiency of the energy cycle and complicates closed-loop operation[12].

Aluminium has the highest volumetric energy density among the three candidates, reaching about 23.5 kWh L^{-1}.[13] Nevertheless, aluminium powders are characterised by an extremely high deflagration index, which imposes severe safety requirements on their handling and use and requires extensive protective measures due to the risk of dust explosions.[14,15] In addition, it is well established that powdered aluminium can ignite at temperatures substantially below its melting point, effectively forcing the process to vapour-phase oxidation.[16] This behaviour promotes the formation of highly dispersed systems, including nanoparticles, which are difficult to collect and cause significant challenges for continuous operation under high mass-flow conditions.[17]

The third candidate, iron, exhibits a volumetric energy density of approximately 16.7 kWh L^{-1},[13] which is lower than that of silicon and aluminium but is accompanied by several decisive advantages. The deflagration index of iron is significantly lower than that of aluminium and even lower than that of coal, making iron powders comparatively safe and convenient to handle.[18,19] Iron powder can be readily stored and transported using established infrastructure. Moreover, due to its high density, moderate gravimetric heating value, and high combustion temperature,

which are comparable to those of conventional hydrocarbon fuels, iron can be utilised in standard combustion systems with only minor modifications.[8,20] Importantly, iron-based energy cycles are considered more efficient and environmentally benign than alternative green energy carriers such as liquid hydrogen (2.4 kWh L^{-1})[21,22] or ammonia (3.8 kWh L^{-1}),[23] particularly when evaluated in terms of safety, storage, transport, and integration at the system-level.

Another practical advantage of using iron powder is its physical properties, which are similar to those of pulverised coal, allowing its application in retrofitted power plants. Only minor modifications to existing plant designs are required, as iron exhibits a lower gravimetric heating value but a higher volumetric energy density compared to coal.[8,24,25] At the same time, such modernisation can simplify the overall process layout, as components such as flue gas desulfurization units and parts of the exhaust gas cleaning system become unnecessary.[26,27]

The development of metal fuel technologies may also have a substantial impact on other large-scale industrial sectors, as it promotes the more efficient use of material reserves and minimises waste generation.[28–31] This is particularly relevant for steel production, where eliminating the need for carbon dioxide capture and transport is capable of significantly reducing process costs.[32] Green hydrogen produced via water electrolysis can serve as a carbon-neutral alternative to the currently dominant blast furnace route in steel production. To date, the so-called direct reduction based on hydrogen in iron ore (H-DRI) has only been partially implemented on an industrial scale.[33–35] However, the technology moves on to advance rapidly because of its vital importance. Several first-of-a-kind plants based on direct reaction with green hydrogen and the associated steel production are currently at advanced stages of design or construction and are expected to become operational within the next few years. Given that the steel industry accounts for approximately 7% of global CO_2 emissions, the potential of the H-DRI process to reduce carbon emissions in this sector is substantial.[36]

1.3 Physical and chemical properties

1.3.1 Iron

Metallic iron exhibits remarkable structural, mechanical, and magnetic properties, making it an exceptionally absorbing subject of research in both science and technology. A vast body of literature is devoted to the pressure–temperature iron phase diagram, since an accurate equation of state forms the basis for theoretical simulation and technological calculations. Of particular interest are the temperature-induced changes in the structural and magnetic properties at ambient pressure.

At low temperatures, iron adopts a body-centred cubic (bcc) crystal structure, commonly known as the α phase. In this state, iron is a typical ferromagnetic material. Upon increasing the temperature to the Curie temperature of 1043 K, the magnetic order is lost, and iron is transformed into a paramagnetic material while retaining the body-centred cubic structure, which is conventionally denoted as β-Fe. With further increase in temperature, two additional phase transitions occur: the first at 1185 K to face-centred cubic (fcc) iron (γ-Fe) and the second at 1667 K back to the body-centred cubic structure (δ-Fe). Both γ- and δ-iron are paramagnetic phases. δ-Iron remains stable up to a melting temperature of 1811 K.[37]

The complex phase behaviour of metallic iron significantly complicates the theoretical description of its physicochemical properties. With increasing temperature, thermal atomic displacements induce increasingly large fluctuations in the magnitudes of local magnetic moments. As a result, it becomes necessary to explicitly account for finite-temperature spin–lattice coupling by considering thermal disorder in both subsystems—the spin and the lattice—simultaneously.[38]

Nevertheless, alternative approaches have been proposed that allow for an accurate description of lattice dynamics in iron crystals. For example, phonon dispersions can be calculated using the self-consistent ab initio lattice dynamical method (SCAILD), while the paramagnetic spin subsystem is approximated by an antiferromagnetic configuration[39]. Within this framework, anharmonic phonon–phonon interactions are found to play a crucial role in stabilising the γ and δ phases of iron.

An alternative strategy for modelling lattice dynamics has been proposed by Leonov and co-workers,[40] where phonons are treated as frozen while paramagnetism is described using dynamical mean-field theory (DMFT). Strong electronic correlations were shown to have a pronounced effect on phase stability, allowing *ab initio* prediction of the β–γ phase transition temperature in iron. Another approach involves treating the magnetic subsystem within the mean-field (MF) and random-phase approximation (RPA).[41] This method provides for an exceptionally accurate description of the α–β phase transition and its associated thermodynamic properties over a wide temperature range.

Experimentally, it is extremely challenging to distinguish the relative importance of individual contributions to specific physicochemical phenomena. In this context, Mauger and co-workers[42] measured the phonon density of states of iron up to the β–γ phase transition using nuclear resonant inelastic X-ray scattering. It was found that with increasing temperature, all phonon modes shift toward lower energies due to thermal expansion. In particular, low-energy transverse modes soften rapidly above 700 K, exhibiting strongly anharmonic behaviour that remains across the magnetic transition. An unusually large anharmonic contribution was reported, leading to an increase in vibrational entropy at high temperatures.[42] This anharmonic contribution follows the thermal evolution of magnetic entropy and may be associated with magnetic excitations. In

addition, only a small change in the vibrational entropy was observed at the structural β–γ phase transition.

Accurate theoretical modelling of lattice dynamics in iron is also of critical importance for the investigation of phase transitions in iron-based alloys.[43] A comprehensive description of all thermodynamic contributions in iron-containing systems provides more reliable predictions of the properties of novel and technologically relevant materials.

1.3.2 Wüstite

Wüstite (FeO) is a typical strongly correlated transition-metal oxide whose electronic and magnetic properties are of scientific and technological interest, including catalytic applications and geophysical relevance. Its electronic properties and phase stability are of great significance for understanding the processes that occur in the interior of the Earth under high-pressure and high-temperature conditions.[44,45] Under ambient conditions, FeO crystallises in the cubic rocksalt-type (B1) structure. At temperatures below 198 K, the crystal exhibits antiferromagnetic ordering, with the magnetic moments of iron atoms aligned along the [111] direction[46,47] (AFMII - type). As a consequence of this magnetic ordering, the crystal symmetry is slightly distorted, resulting in a small structural distortion along the direction of spin alignment. The temperature of 198 K corresponds to the Néel temperature of wüstite[48], marking the phase transition from the antiferromagnetic to the paramagnetic state.

First-principles studies have shown that density functional theory approaches within local density (LDA) and generalised gradient (GGA) approximations do not succeed to correctly describe FeO, predicting a metallic ground state instead of the experimentally observed antiferromagnetic insulator.[49] The inclusion of on-site electron–electron interactions within the DFT+U framework is therefore essential to open the band gap and reproduce experimentally measured electronic and magnetic properties. More advanced exchange–correlation functionals, such as the SCAN (meta-GGA), significantly improve the description of magnetic ordering but still require an additional Hubbard U term to correctly capture the phase stability and band gap of FeO. Overall, these studies highlight that an explicit treatment of strong electronic correlations remains crucial for a quantitatively accurate description of the structural, magnetic, and electronic behaviour of FeO.[50,51]

Beyond the ground-state electronic structure, the coupling between magnetic ordering, orbital occupancy, and lattice distortions plays a decisive role in transition-metal monoxides such as MnO, FeO, CoO, and NiO. First-principles studies demonstrate that below the Néel temperature, antiferromagnetic ordering induces symmetry-lowering distortions of the rocksalt structure, whose character depends sensitively on the occupation of the minority-spin t_{2g} states. Spin–orbit

coupling and transverse electron interactions are shown to govern magnetic anisotropy, with FeO and CoO being particularly affected due to their partially filled t_{2g} subshells.[52,53] More advanced electronic-structure approaches, including screened hybrid functionals and many-body GW calculations, provide an improved description of band gaps and densities of states, yielding results in good agreement with experimental data.[54] These studies underline that a quantitative description of FeO requires the simultaneous treatment of strong electronic correlations, magnetic anisotropy, and lattice distortions. Consequently, FeO and related monoxides serve as benchmark systems to assess the capabilities and limitations of modern first-principles methods in strongly correlated materials.

Wüstite is intrinsically non-stoichiometric and is commonly described as $Fe_{1-x}O$, where deviations from stoichiometry are primarily accommodated by cation vacancies and associated changes in the Fe valence state. These Fe vacancies are not merely a structural imperfection: they induce pronounced local modifications of the lattice, electronic structure, and magnetism, and thereby control macroscopic properties such as transport, diffusion, and phase stability. First-principles studies of $Fe_{1-x}O$ show that Fe vacancies promote complex charge and magnetic rearrangements on the Fe sublattice, leading to polaron-like charge distributions and short-range correlations that are conceptually related to the charge ordering phenomena in magnetite.[55] Vacancies also have a strong impact on lattice dynamics: when strong on-site Coulomb interactions at Fe are accounted for (DFT+U), vacancy-stabilised trivalent Fe states introduce defect-related unoccupied bands and substantially reduce the insulating gap, while vacancy-induced atomic displacements modify force constants beyond nearest neighbours and lead to measurable changes in phonon dispersions.[56] Importantly, quantitative agreement with inelastic neutron and nuclear resonant X-ray scattering data is achieved only when both electronic correlations and explicit vacancy defects are included, suggesting a strong coupling between electronic and vibrational degrees of freedom in FeO.

At larger length and time scales, atomistic simulations provide complementary insight into how defect thermodynamics and microstructure evolve under realistic environments. Molecular dynamics studies of wüstite films in contact with liquid metal coolants highlight that the chemical potentials of dissolved Fe and O in the liquid phase can significantly influence the free energies of defect formation in oxide, allowing a consistent thermodynamic link between equilibrium defect concentrations and chemical potential-based descriptions.[57] Recent machine-learning interatomic potentials further extend the accessible scales and indicate that cation vacancies in wüstite tend to aggregate into stable defect clusters, including structures consistent with Koch–Cohen-type clusters, and that interstitial Fe can form as part of the non-stoichiometry accommodation mechanisms.[58] Together, these results establish point defects and defect clustering as central phenomena in the physics and chemistry of FeO, and motivate simulation strategies that treat lattice, charge, magnetism, and defect populations on an equal footing when exploring redox-driven transformations in Fe–O systems.

1.3.3 Magnetite

Under ambient conditions, magnetite (Fe_3O_4) crystallises in the inverse spinel structure. Spinels are commonly described by the general formula AB_2O_4, where A and B denote cations occupying distinct crystallographic sublattices. In the case of magnetite, the cation distribution is conventionally written as $(Fe^{3+})_A[Fe^{2+}Fe^{3+}]_BO_4$, where parentheses and brackets indicate the tetrahedral (A) and octahedral (B) sites, respectively. In a normal spinel, the A cations occupy tetrahedral sites while the B cations occupy octahedral sites; however, in an inverse spinel the divalent cations reside on octahedral sites, whereas the trivalent cations are distributed between tetrahedral sites and the remaining octahedral sites. This cation arrangement is commonly rationalised by the comparatively larger crystal-field stabilisation energy of Fe^{2+} in octahedral coordination than in tetrahedral coordination.[59] The spinel structure is based on an fcc O^{2-} anion lattice, in which 1/8 of the tetrahedral and half of the octahedral interstices are occupied.

Magnetite displays several remarkable properties. At temperatures around 120 K, it shows the Verwey transition, which is manifested as an abrupt change in electrical conductivity upon heating, and it is often described as an insulator–metal transition.[60] Importantly, this electronic transition is accompanied by a structural phase transition: Fe_3O_4 transforms from a low-temperature monoclinic structure to the high-temperature cubic inverse spinel phase. In terms of its magnetic properties, magnetite can be characterised as a ferrimagnet and a half-metal, with a Néel temperature of approximately 850 K.[61]

First-principles investigations highlight that the predicted electronic structure of magnetite is highly sensitive to the treatment of electronic correlations and self-interaction errors.[62] Self-interaction corrected local spin-density studies indicate that the “Verwey charge-ordered” pattern is not necessarily the lowest-energy solution in either ideal cubic or approximated low-temperature distorted structures, suggesting that structural distortions may play a more decisive function in driving charge disproportionation than correlation-induced localisation alone. Consistent with this perspective, DFT-based analyses that relax symmetry constraints on the electronic density (while keeping the lattice geometry fixed) find that charge disproportionation can emerge already in the cubic phase, opening a small gap on the order of 0.2 eV.[63] This result supports an interpretation of the Verwey transition as a semiconductor-to-semiconductor transition and points toward small-polaron hopping as the dominant transport mechanism above T_V = 120 K.

A further complication is methodological: different exchange–correlation approximations can qualitatively alter the nature of levels close to the Fermi level.[64] Comparative calculations using semilocal GGA, DFT+U, and range-separated hybrid functionals (e.g., HSE-type) show that the inclusion of exact exchange can dramatically modify the degree of electron localisation, the character of the valence band edge, and the distribution of magnetic moments and atomic

charges. Such functional dependence implies that a consistent description of bulk magnetite at room temperature, as well as its surfaces and interfaces relevant for device concepts, may require methodological choices that are not directly transferable from the low-temperature phase. Finally, comparative DFT+U studies of magnetite and its inverse-spinel analogue greigite (Fe_3S_4) demonstrate how changes in bonding character (more covalent sulfide versus more ionic oxide) influence elastic and magnetic properties, providing additional insight into the structure–property relations in mixed-valence spinels.[65]

First-principles DFT studies demonstrate that the relative stability of magnetite surfaces depends sensitively on the oxygen chemical potential, such that different terminations and compositions (stoichiometric, oxygen-deficient, and oxygen-rich) may become thermodynamically preferred under realistic operating conditions. In equilibrium, the (001) and (111) facets are often identified as the most stable, implying a characteristic truncated-cubic morphology.[66] However, redox conditions can considerably affect the surface composition and local electronic structure. Under reducing conditions, oxygen-vacancy formation leads to reduced Fe species in the vicinity of the vacancy, with the (001) surface predicted to be slightly more prone to reduction than (111) due to stronger stabilisation upon structural relaxation, whereas molecular oxygen adsorption is found to be favoured on the (111) surface. Conversely, under oxidizing conditions, additional oxygen atoms can stabilize oxidized surface configurations (e.g., bridge-like oxygen species bound between surface Fe atoms), which may remain favorable under ambient environments even when bulk Fe_3O_4 stability competes with further oxidation toward Fe_2O_3; this has direct implications toward interpreting catalytic performance, since experimentally relevant surfaces can be more oxidized than the bulk composition would suggest.

A consistent theme across these studies is the importance of simultaneously capturing structural relaxation, electronic correlation, and defect chemistry. Detailed calculations for Fe_3O_4 (111) indicate very large relaxations of near-surface interlayer distances, and DFT+U generally strengthens metal–surface bonding relative to semilocal DFT, indicating the role of on-site Coulomb interactions for the Fe 3d bands.[67] The thermodynamic analysis, moreover, suggests that Fe-terminated (111) surfaces can be stable over a wide range of oxygen chemical potentials, while point defects and adatoms may be competitive in surface energy and even become preferred in oxygen-rich or oxygen-poor regimes. Importantly, distinct terminations, vacancies, and adatoms can produce qualitatively different electronic structures and spin-polarisation features near the Fermi level, which is critical for both adsorption reactivity (e.g., noble-metal anchoring such as Pd versus Au) and for interfacial spin transport in organic spintronic architectures.[68]

A key issue in understanding and exploiting magnetite in heterogeneous catalysis, biocompatible hybrid materials, and device frameworks is that many relevant phenomena occur in complex nanostructures and at solid–liquid or solid–organic interfaces, where system sizes and time scales

exceed the practical limits of conventional electronic-structure calculations. This has motivated the development of efficient atomistic models that retain the crucial physics of electrostatics and mixed valency while enabling simulations of thousands of atoms. In this context, an empirical force field for the magnetite (001) and (111) surfaces has been constructed using partial charges derived from ab initio Bader analyses, providing an accurate description of electrostatic interactions upon magnetite–water and magnetite–organic interfaces. Such models suggest that surface charge redistribution is a main mechanism underlying magnetite surface reconstruction and ligand binding, and they provide a practical route to studying realistic nanoparticles and interfacial chemistries with a favourable balance between accuracy and computational efficiency.[69]

Beyond surface chemistry, the mechanical stability of oxide scales and the adhesion at metal/oxide interfaces are critical for industrial components, where the interfacial bonding controls susceptibility to degradation mechanisms. For the technologically important Fe/Fe3O4 system, first-principles analyses of the interfacial charge density and charge redistribution indicate that adhesion is governed by the interaction and electronic rearrangement of surface iron species at the interface, linking bonding properties to measured adhesion trends.[70] At the same time, describing the finite-temperature dynamics of mixed valency in magnetite requires methodologies that go beyond static electronic-structure calculations. A hybrid Monte Carlo/Molecular Dynamics approach based on explicit oxidation-state swapping has been proposed to reproduce oxidation-state patterns that match those of density functional theory, while enabling simulations of bulk magnetite, surfaces, and nanoparticles at relevant length and time scales.[71] These simulations show lattice distortions that stabilise excess charges and identify a critical near-surface thickness at which oxidation-state order transitions to disorder, providing a mechanistic framework for understanding charge-state dynamics in inverse spinels. Finally, cation diffusion in ferrite spinels—often central to functionality in catalysis and energy-related applications—has been analysed using DFT and crystal-field arguments, showing that migration proceeds via a metastable tetrahedral intermediate and that diffusion barriers are systematically governed by the crystal-field splitting of the migrating cation as well as by the spinel lattice parameter.[72] Collectively, these results underscore that a comprehensive description of magnetite across applications requires treating electrostatics, redox/valence dynamics, interfaces, and ionic transport within a single unified atomistic modelling strategy.

1.3.4 Hematite

Hematite (α-Fe_2O_3) crystallises in the corundum-type structure, which is isostructural with Al_2O_3.[73] The oxygen sublattice forms a slightly distorted hexagonal close-packed stacking along the crystallographic c-axis, while iron cations occupy two thirds of the octahedral interstices.

Hematite is an antiferromagnet, with the magnetic moments ordered along the [0001] direction. Its Néel temperature is approximately 955 K.

The experimental work shows that the structural, vibrational, and electronic properties of hematite are strongly coupled and can change markedly under extreme conditions.[74] High-pressure measurements of the phonon density of states combined with first-principles calculations reveal pronounced anomalies in elastic and vibrational behaviour across a pressure-induced structural transformation to a Rh_2O_3(II)-type phase at roughly 40–50 GPa. In contrast, the subsequent Mott-type insulator–metal transition occurring at higher pressures produces only comparatively minor changes in the vibrational and thermodynamic response, indicating that lattice dynamics is primarily governed by structural rearrangement rather than by electronic transition alone. These observations highlight hematite as a representative transition-metal oxide in which pressure can decouple structural and electronic transformations and thus generate definite signatures in the phonon spectrum and elastic constants.[74]

At ambient pressure, achieving a quantitatively reliable description of hematite remains challenging for standard density functional theory because approximate exchange–correlation functionals suffer from self-interaction errors and an incomplete treatment of localised Fe 3d states. Semilocal DFT typically underestimates the band gap and can misrepresent the nature of the insulating state, whereas correlation-corrected approaches such as DFT+U and hybrid functionals recover an antiferromagnetic insulating ground state and substantially improve agreement with spectroscopy.[75] In particular, screened hybrid DFT has been shown to reproduce the experimental band gap and key magnetic and structural properties without relying on empirically tuned d-electron parameters, allowing systematic studies of dopant-induced symmetry breaking and changes in optical response relevant to photocatalysis[76]. Beyond these established approaches, DFT+U+V—an extension that includes inter-site interactions—further improves the description of structure, magnetism, electronic properties, and X-ray absorption signatures at a fraction of the computational cost of hybrid functionals, while indicating a nontrivial dependence on the choice of atomic-orbital projectors.[77]

Charge-carrier physics in hematite is also strongly related to local lattice distortions. Hybrid-DFT studies indicate that holes tend to self-trap as small polarons localised on individual Fe sites, with localisation driven by local Fe–O bond distortions that lead to thermally activated hopping and intrinsically sluggish hole transport. In contrast, excess electrons are predicted to be more delocalized over neighbouring Fe units and thus show greater mobility.[78] This polaronic transport picture gives a microscopic explanation for the limited charge-transport performance of hematite in photoelectrochemical water splitting and directly links electronic conductivity to local structural relaxations.[78]

Finally, both experiment and theory show that hematite's magnetic response is sensitive to microstructure and confinement. Neutron diffraction measurements on mesoporous hematite demonstrate that confinement can suppress the Morin transition observed in bulk material, maintaining weak ferromagnetism down to very low temperatures and altering the orientation of magnetic moments relative to the crystallographic axis.[79] Collectively, these studies underline that predictive modelling of α-Fe_2O_3 requires simultaneous consideration of strong correlations, lattice distortions, and microstructure-dependent magnetism, which is essential when hematite participates in redox transformations within the wider Fe–O system.

First-principles studies show that predicted surface energetics and electronic structure can be sensitive to the chosen exchange–correlation fuctional: while structural relaxations of the α-$Fe_2O_3(0001)$ surface are often similar between PBE(+U) and screened hybrid functionals, quantities such as work function, stability trends, and near-gap states may differ, highlighting the need for careful methodological benchmarking.[80] Under hydroxylating conditions, PBE+U calculations with dispersion corrections indicate that low OH coverages remain stable down to relatively low water chemical potentials, whereas reduced terminations containing Fe^{2+} become favourable only at sufficiently reducing oxygen chemical potentials where bulk α-Fe_2O_3 is no longer more stable than magnetite.[81] Ab initio thermodynamics further predicts that the stable termination of hydrated hematite surfaces depends strongly on temperature, oxygen partial pressure, and water activity, with changes in protonation and hydroxyl group populations leading to large variations in stability and substrate relaxations.[82]

At the surface, hybrid-functional studies of water oxidation suggest that subsurface oxygen vacancies can stabilise oxygen adsorption and reshape the reaction-energy landscape; however, they may also increase the overpotential for electro-oxidation, with oxygen-terminated hematite predicted to exhibit the lowest overpotential among the considered terminations.[83]

1.4 Scope of this work

The primary objective of this study is to develop a consistent methodology that enables both qualitative and quantitative descriptions of the peculiarities and phenomena associated with redox processes in the Fe–O system in both solid and liquid states. In **Chapter 3**, the thermodynamic properties of iron and its oxides are calculated from first principles. Thermal properties are determined within the quasi-harmonic approximation. The resulting data allow us to consider oxidation and reduction as chemical reactions. To this end, phase diagrams of the system are constructed under both oxidising and reducing conditions.

The next step, described in **Chapter 4**, is the calculation of the diffusion coefficients of the iron and oxygen species in the bulk phases of iron and its oxides. Together with the thermodynamic data described above, the results provide a quantitative characterisation of mass-transport rates in the Fe–O system under oxidising and reducing conditions.

The **Chapter 3** and the **Chapter 4** are based on:

- **Aleksandr Maliugin**, Dmitry I. Sharapa, and Felix Studt. Theoretical study on iron oxidation and reduction of iron oxide. In preparation, 2026.

The surface and bulk phenomena in iron, discussed in **Chapter 5**, clarify key aspects of oxygen and hydrogen adsorption and diffusion. Migration barriers for the relevant species are computed both at the surface and in the bulk. In addition, the feasibility of describing electrochemical reduction within first-principles methods is considered.

Furthermore, **Chapter 6** addresses adsorption and diffusion phenomena in Fe_2O_3. A mechanism for the formation of a water molecule on the hematite surface is proposed, and the activation energies governing the rate of the underlying elementary steps are determined.

The chapter based on:

- Lukas Braun, Jonas Spielmann, Dmitry E Doronkin, Carola Kuhn, **Aleksandr Maliugin**, Dmitry I Sharapa, Isabel Huck, Jianing Bao, Steffen Tischer, Felix Studt, et al. Following the structural changes of iron oxides during reduction under transient conditions. ChemSusChem, 17(24):e202401045, 2024.

Chapter 7 is devoted to a first-principles-based description of liquid Fe–O. A machine learning interatomic potential is trained with an accuracy comparable to DFT while enabling simulations via classical molecular dynamics. This approach makes it possible to investigate the system at substantially larger time and size scales. Thermodynamic and transport properties are calculated as functions of composition and temperature.

This chapter is based on:

- **Aleksandr Maliugin**, Dmitry I. Sharapa, and Felix Studt. Molecular dynamics study of the liquid fe-o system using a machine learning interatomic potential. In preparation, 2026.

Using the trained MLIP, a series of MD simulations of oxidation of liquid-iron nanoparticles and an iron slab are carried out, as reported in **Chapter 8**. The systematic trends of the oxidation process are identified, and a schematic mechanism is proposed.

This chapter is based on:

- **Aleksandr Maliugin**, Dmitry I. Sharapa, and Felix Studt. Liquid-state oxidation processes in the iron–oxygen system. In preparation, 2026.

Finally, the methodology developed for reactive liquid condensed metal systems is not limited to the Fe–O system and can be transferred to other chemistries. As an additional case study, **Chapter 9** introduces the SCALMS concept, which employs low-melting metal alloys doped with catalytically active atoms as reaction media for propane dehydrogenation. A separate MLIP was trained to enable large-scale MD simulations of this system, and the resulting trajectories were used to examine the atomistic reaction mechanism. This case study demonstrates the broader applicability of the proposed workflow and provides atomistic support for several mechanistic scenarios discussed in the literature.

This chapter is based on:

- Moritz Wolf, Thomas Gradl, Shaine Raseale, **Aleksandr Maliugin**, Narayanan Raman, Patrick Schühle, Nicola Taccardi, Michael Claeys, Dmitry I Sharapa, Felix Studt, et al. In-pt supported catalytically active liquid metal solutions for propane dehydrogenation–role of surface acidity of support. ChemCatChem, page e202402096, 2025.

2 Computational methods

2.1 Electronic Structure Therory

In quantum-mechanical treatments of crystals and molecules, it is common to separate the electronic and ionic degrees of freedom within the Born–Oppenheimer approximation. According to this approximation, nuclear dynamics have a negligible effect on the dynamics of the electron subsystem. This allows the true wave function to be separated into its electron and nuclear components, with the nuclear positions treated as parameters of the electron subsystem. This approximation is justified by the significant difference in the masses between electrons and nuclei. The electronic subsystem is then governed by the time-independent Schrödinger equation.

In practice, solving the resulting many-electron problem is unsolvable for most systems. The difficulty stems from the very high dimensionality of the Hilbert space and from the need for a self-consistent solution, since the electronic Hamiltonian includes electron–electron interactions. A key simplification is therefore to replace the full many-body wave function with the electron density, which is considerably more convenient for computations.

Density functional theory (DFT) is one of the most successful and widely used frameworks for predicting the properties of molecules and crystalline solids. Accordingly, DFT is the standard choice for the electronic-structure step in most quantum-mechanical calculations.

2.1.1 Hohenberg–Kohn Theorems

In 1964, Hohenberg and Kohn formulated and proved two theorems that underpin modern density functional theory.[84] These theorems establish an exact correspondence between electron density $n(\mathbf{r})$, external potential $V_{\mathrm{ext}}(\mathbf{r})$, and many-electron wave function Ψ_{N}. In quantum mechanics, the ground-state wave function is obtained by minimizing the energy functional. For an N-electron system, the form of the external potential uniquely specifies the Hamiltonian; therefore, Ψ_{N} and $V_{\mathrm{ext}}(\mathbf{r})$ determine all ground-state properties.

Theorem 1. Instead of treating the many-electron wave function Ψ_{N} as the basic variable, Hohenberg and Kohn proposed the electron density $n(\mathbf{r})$ as the fundamental variable of the energy functional. For a non-degenerate ground state, the external potential $V_{\mathrm{ext}}(\mathbf{r})$ is uniquely determined by $n(\mathbf{r})$ up to an additive constant. Consequently, $n(\mathbf{r})$ uniquely fixes the ground-state wave function Ψ_0 (and thus all ground-state observables), since Ψ_0 is determined by V_{ext}, which in turn is a functional of $n(\mathbf{r})$.

Theorem 2. For any N-representable electron density $n(\mathbf{r})$, one can define a universal functional $F[n]$ such that the total energy in an external potential $V_{\mathrm{ext}}(\mathbf{r})$ is

$$E_v[n] = F[n] + \int V_{\mathrm{ext}}(\mathbf{r})\, n(\mathbf{r})\, d\mathbf{r}.$$

The ground-state energy satisfies the variational principle

$$E_0 = \min_n E_V[n],$$

so that $E_v[n] \geq E_0$ for any admissible density $n(\mathbf{r})$, with equality at the exact ground-state density.

Within the Hohenberg–Kohn framework, the generalized total-energy functional can be written as:

$$E_{\mathrm{HK}}[n] = T[n] + E_{\mathrm{int}}[n] + \int d\mathbf{r}\, V_{\mathrm{ext}}(\mathbf{r})\, n(\mathbf{r}) + E_{II}, \tag{2.1}$$

where $F_{\mathrm{HK}}[n] = T[n] + E_{\mathrm{int}}[n]$ is universal functional of the kinetic energy and the potential energy of electron–electron interactions, respectively, and E_{II} is the nucleus–nucleus interaction energy.

Thus, to determine the ground-state energy and the electron-density distribution, it is sufficient to know the functional $F_{\mathrm{HK}}[n]$. By minimizing the total energy of the system (eq. 2.1), one can obtain the ground-state electron density.

2.1.2 Kohn–Sham Equations

To overcome the difficulties associated with explicitly treating particle–particle interactions, Kohn and Sham proposed to treat the ground-state electron density of an auxiliary system of non-interacting particles.[85] In this construction, all complicated many-body effects are incorporated

through the exchange–correlation functional E_{xc}, which makes the electronic problem solvable. Within this approximation, the electron density is obtained by minimizing the functional:

$$E_{\mathrm{KS}} = T_{\mathrm{S}}[n] + \int d\mathbf{r}\, V_{\mathrm{ext}}(\mathbf{r}) n(\mathbf{r}) + E_{\mathrm{H}}[n] + E_{II} + E_{\mathrm{xc}}[n], \tag{2.2}$$

where $T_{\mathrm{S}}[n]$ is the kinetic-energy functional. However, the explicit form of T_{S} for the interacting problem remains unknown. Therefore, auxiliary single-particle wave functions of the non-interacting system, ψ_i^{KS}, referred to the Kohn–Sham orbitals, are introduced, and the kinetic energy is defined via the quantum-mechanical expectation value:

$$T_{\mathrm{S}} = -\frac{1}{2} \sum_{i=1}^{N} \int \psi_i^{\mathrm{KS}*}(\mathbf{r}) \nabla^2 \psi_i^{\mathrm{KS}}(\mathbf{r})\, d\mathbf{r}. \tag{2.3}$$

The Hartree energy E_H is given by:

$$E_H[n] = \frac{1}{2} \int d\mathbf{r}\, d\mathbf{r}' \, \frac{n(\mathbf{r}) n(\mathbf{r}')}{|\mathbf{r} - \mathbf{r}'|}. \tag{2.4}$$

Applying the variational principle to the energy functional yields the Kohn–Sham equations:

$$\left[-\frac{1}{2}\nabla^2 - \sum_{j=1}^{I} \frac{Z_j}{|\mathbf{R}_j - \mathbf{r}|} + \int \frac{n(\mathbf{r}')}{|\mathbf{r} - \mathbf{r}'|} d\mathbf{r}' + V_{\mathrm{XC}}(\mathbf{r}) \right] \psi_i^{\mathrm{KS}}(\mathbf{r}) = \varepsilon_i \psi_i^{\mathrm{KS}}(\mathbf{r}), \tag{2.5}$$

where Z_j and $\mathbf{R}_j$ are the charge and position of the j-th ion, respectively. All three potential-energy operators are local, because their action reduces to multiplying the wave function, leaving only a dependence on a single coordinate $\mathbf{r}$. The electron density of the interacting system is assumed to be equal to that of the auxiliary non-interacting system and is expressed as the sum of the diagonal elements of the Kohn–Sham orbital density matrix after integration over the spin variables:

$$n(\mathbf{r}) = \sum_{i=1}^{N} |\psi_i^{\mathrm{KS}}|^2 = N \int ... \int |\Psi_{\mathrm{N}}|^2 ds_1\, d\mathbf{r}_2\, ds_2 ... d\mathbf{r}_N\, d\, s_N, \tag{2.6}$$

where Ψ_{N} is the true many-electron wave function.

The exchange–correlation potential V_{xc}, which accounts for the correction to the kinetic energy that compensates for the independent-electron approximation, as well as for the self-interaction correction, is defined as

$$V_{xc} = \frac{\delta E_{xc}[n]}{\delta n}. \tag{2.7}$$

All practical approximations within the Kohn–Sham formalism are associated with the choice of the exchange–correlation functional, which depends on the physical nature of the problem under study. Many functionals are based on the model of the homogeneous electron gas. The most widely used are the local density approximation (local density approximation, LDA; for spin-polarized systems, LSDA), where the energy depends only on $n(\mathbf{r})$, and the generalized gradient approximation (generalized gradient approximation, GGA), where the energy additionally depends on spatial derivatives of the electron density. At present, GGA functionals are among the most commonly employed. Later, these functionals were extended by introducing a dependence on the kinetic-energy density; such functionals are referred to as meta-GGA (MGGA). Importantly, using a precomputed $E_{xc}[n]$ over a broad range of $n(\mathbf{r})$ based on quantum many-body Monte Carlo calculations renders a DFT calculation first-principles.

2.1.3 Bloch Theorem

In crystalline solids, an electron moves in a three-dimensional periodic potential. According to Bloch's theorem,[86] an electronic wave function that is invariant under the symmetry operation of a lattice translation and is simultaneously an eigenfunction of the Hamiltonian can be written as the product of a plane wave and a function with the periodicity of the Bravais lattice:

$$\varphi_{\mathbf{k}}(\mathbf{r}) = \exp\left[i(\mathbf{k}\cdot\mathbf{r})\right] u_{\mathbf{k}}(\mathbf{r}), \tag{2.8}$$

where $\mathbf{k}$ is the Bloch wave vector that belongs to the first Brillouin zone. The periodic function $u_{\mathbf{k}}$ can be expanded on the basis of plane waves with reciprocal lattice vectors:

$$u_{\mathbf{k}}(\mathbf{r}) = \sum_{\mathbf{G}} c_{\mathbf{k}}(\mathbf{G}) \exp\left[i(\mathbf{G}\cdot\mathbf{r})\right], \tag{2.9}$$

where $\mathbf{G}$ is a reciprocal-lattice vector. Then we can use these functions as a basis for the single-particle wave function sought in the n-th band:

$$\psi_{n\mathbf{k}}(\mathbf{r}) = \sum_{\mathbf{G}} c_{n,\mathbf{k}+\mathbf{G}} \exp\left[i((\mathbf{k}+\mathbf{G})\cdot\mathbf{r})\right]. \tag{2.10}$$

2.1.4 Plane-Wave Basis Set

In plane-wave implementations of density functional theory, the electronic wave functions are expanded in a plane-wave basis set, which is formally infinite. In practice, the basis is truncated using an energy cutoff parameter E_{cut}, such that only plane waves satisfying

$$\frac{1}{2}|\mathbf{G}+\mathbf{k}|^2 \leq E_{\mathrm{cut}} \tag{2.11}$$

which represents the maximum kinetic energy of a basis plane wave, or, equivalently, the radius of a sphere in reciprocal space. All plane waves lying within this sphere, i.e., having kinetic energies below the cutoff, are included in the basis set. The value of this parameter is chosen based on the specific problem and must be validated by convergence tests. In particular, more localized orbitals typically require a larger plane-wave basis.

Figure 2.1 schematically illustrates the construction of the plane-wave basis set. In VASP,[87] the calculations are implemented using optimized algorithms based on the fast Fourier transform (FFT). A real-space simulation cell discretized by an N_{FFT} grid corresponds to a reciprocal-space lattice. As is well known, the first Brillouin zone, which contains all information required to describe the electronic properties of a crystal, corresponds to the Wigner–Seitz cell of the reciprocal lattice sampled by a $\mathbf{k}$-point mesh. All reciprocal-lattice vectors $\vec{G}$ that satisfy condition 2.11 are included in the plane-wave basis.

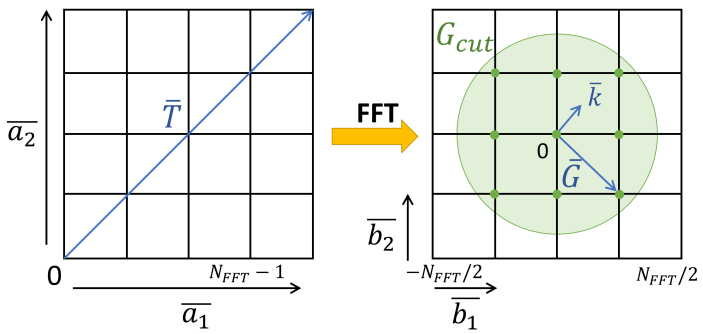

Figure 2.1: Schematic illustration of the construction of the plane-wave basis set; $\vec{a_1}$ and $\vec{a_1}$ are Bravais-lattice vectors, $\vec{T}$ is a translation vector, and $\vec{b_1}$ and $\vec{b_2}$ are reciprocal-lattice vectors.

To reduce the number of Kohn–Sham equations to be solved, one exploits the fact that wave functions corresponding to nearby $\mathbf{k}$ points are very similar. Therefore, within a given region of reciprocal space, the electronic states can be approximated using a finite set of representative $\mathbf{k}$ points with appropriate weights $w_{\mathbf{k}}$ that account for symmetry. This approach accelerates the calculations, while the associated error is controlled by choosing a sufficiently dense $\mathbf{k}$-point mesh. The technical parameter `KPOINTS`, which determines the density of the mesh, must also be tested for convergence.

With $\mathbf{k}$-point sampling, the electron density can be written as

$$n(\mathbf{r}) = \sum_{n\mathbf{k}} w_{\mathbf{k}}\, f_{n\mathbf{k}}\, |\psi_{n\mathbf{k}}(\mathbf{r})|^2\, d\mathbf{k}, \tag{2.12}$$

where $f_{n\mathbf{k}}$ are the occupation numbers given by the Fermi–Dirac distribution:

$$f = \frac{g_i}{\exp\left(\dfrac{\varepsilon_i - \mu}{k_B T}\right) + 1}, \tag{2.13}$$

where ε_i is the energy of the ith state, g_i is its degeneracy, and μ is the chemical potential.

2.1.5 Pseudopotential Method

Nevertheless, solving the Kohn–Sham equations remains a highly demanding task. The electronic wave functions exhibit a complex structure; in particular, the core states close to the nuclei are strongly oscillatory, which would require an extremely large number of plane waves for an accurate representation. As a result, all-electron calculations are feasible only for a very limited class of systems. Importantly, however, these core states depend only weakly on the relative arrangement of nuclei in the system. Therefore, it is sufficient to compute the core electron density once by solving the all-electron problem for an isolated atom in the spherically symmetric approximation.

The pseudopotential approach retains only the interaction of valence electrons with a smooth pseudopotential that reproduces the net effect of the core electrons on the valence states. The rapidly oscillating functions near the nuclei are replaced by smooth pseudo-wave functions. In this way, the required plane-wave basis can be drastically reduced, and the computational cost is significantly lowered.

In the projector augmented-wave (PAW) method, originally proposed by Blöchl,[88] space around each atom is partitioned into atom-centered augmentation regions and an interstitial region. In the interstitial region the electronic wave functions are smooth and can be efficiently expanded

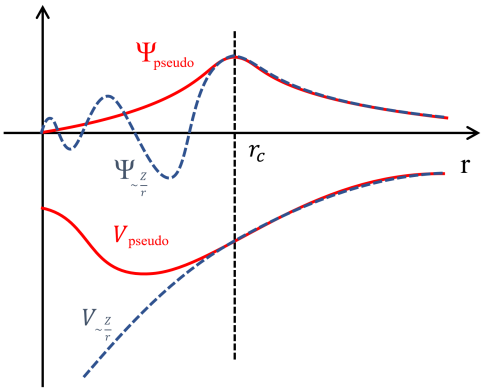

Figure 2.2: Illustration of the pseudopotential concept. The smooth pseudopotential is shown by the red solid line, while the Coulomb potential is shown by the blue dashed line.

in a plane-wave basis. Inside the augmentation spheres the all-electron wave functions exhibit strong oscillations due to the presence of the atomic cores.

Within the PAW formalism the true all-electron wave function $|\Psi\rangle$ is related to a smooth pseudo-wave function $|\tilde{\Psi}\rangle$ through a linear transformation. The rapidly oscillating all-electron wave functions in the augmentation regions are replaced by smooth pseudo-wave functions that vary slowly in space. Outside the augmentation spheres the pseudo and all-electron wave functions coincide.

The all-electron wave function can be reconstructed as

$$|\Psi\rangle = |\tilde{\Psi}\rangle + \sum_{at,i} \left(|\phi_{i,at}\rangle - |\tilde{\phi}_{i,at}\rangle \right) \langle \tilde{p}_{i,at} | \tilde{\Psi} \rangle, \tag{2.14}$$

where $|\phi_{i,at}\rangle$ and $|\tilde{\phi}_{i,at}\rangle$ are the all-electron and pseudo partial waves defined inside the augmentation region of atom at, respectively, and $\langle \tilde{p}_{i,at}|$ are projector functions that extract the expansion coefficients of the pseudo-wave function in the partial-wave basis.

A PAW dataset contains information about the partial waves for a given atomic species, which are then used as a basis within the augmentation region. The pseudo-basis functions are smooth partial waves $|\tilde{\phi}_{i,at}\rangle$ that coincide with the true partial waves outside the augmentation sphere but are smoother inside it.

Thus, this approach can substantially increase computational efficiency because the core electronic structure does not need to be recomputed for every calculation. Since the pseudo-wave function

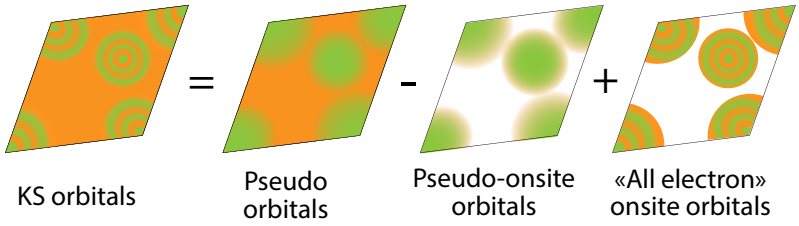

Figure 2.3: Construction of the all-electron wave function within the PAW framework according to Eq. 2.14.

$|\tilde{\Psi}\rangle$ is smoother than the all-electron one, it can be represented with a much smaller plane-wave basis and, consequently, a lower E_{cut}. The specific form of a pseudopotential depends on many technical choices, such as the augmentation radius, the construction scheme, the number of all-electron partial waves, and so forth. These parameters determine both the accuracy of the results and the computational performance.

2.1.6 Exchange–Correlation Functionals

The independent-electron approximation provides a convenient route to solving the many-electron problem, but it must be compensated by introducing the exchange–correlation (xc) energy. Accordingly, the kinetic energy of the interacting physical system is written as the sum of the kinetic-energy functional of the non-interacting electrons $T_{\mathrm{S}}[n]$ ("S" for single-particle) and the correlation contribution $T_{\mathrm{C}}[n]$ ("C" for correlation):

$$T[n] = T_S[n] + T_C[n]. \tag{2.15}$$

The exact form of $T_{\mathrm{S}}[n]$ is unknown. However, it can be expressed explicitly in terms of the single-particle orbitals as the sum of the kinetic energies of non-interacting particles:

$$T_{\mathrm{S}}[\,\{\psi_i\}] = \frac{1}{2}\sum_{i=1}^{N}\langle\psi_i|\nabla^2|\psi_i\rangle. \tag{2.16}$$

The potential part of the exchange–correlation energy is commonly decomposed into correlation and exchange contributions. The exchange energy can be written exactly in terms of the single-particle orbitals as the Fock expression:

$$E_x[\{\psi_i\}] = -\frac{1}{2}\sum_{i,j}\iint d\mathbf{r}\, d\mathbf{r}' \frac{\psi_i^*(\mathbf{r})\psi_j^*(\mathbf{r}')\psi_i(\mathbf{r}')\psi_j(\mathbf{r})}{|\mathbf{r}-\mathbf{r}'|}, \tag{2.17}$$

whereas no analogous explicit expression exists for the correlation part of the potential energy. Evidently, the total correlation energy consists of kinetic and potential contributions.

2.1.6.1 Exchange and Correlation

It is tempting to compute the exchange–correlation energy using the exact wave-function-based expression for the exchange (2.17) and to obtain the correlation—being computationally the most demanding—within DFT. However, the key difficulty is that the definitions of the E_{XC} in DFT and in the Hartree–Fock approximation (HFA) are not fully equivalent. The exchange energy in DFT can be written in the same form as in HFA, except that the Kohn–Sham orbitals are used instead of Hartree–Fock orbitals. This introduces a non-local potential into the problem.

Both exchange and correlation contain short-range and long-range components. Long-range correlation is, in essence, associated with static correlation, whereas short-range correlation corresponds to dynamical correlation. These contributions complement the exchange energy in a non-trivial way, partially compensating each other.[89] Historically, the DFT XC-functional was conceived as local, with the compensation of long-range effects built in implicitly. As a result, combining the two approaches could lead to ambiguity and physical inconsistency. In more recent developments, DFT, HFA, and RPA have been unified within the adiabatic-connection fluctuation–dissipation theorem (ACFDT).

It is often most convenient to discuss this issue in terms of exchange–correlation holes. Electrons avoid each other because this lowers the energy. This behavior arises from classical Coulomb repulsion (between negatively charged particles), the Pauli principle (exchange interactions for electrons with the same spin), and correlation (Coulomb interactions between electrons of parallel and antiparallel spins). The exchange–correlation hole is the region of space in which finding a second electron is less probable. The probability of finding one electron at $\mathbf{r}_1$ and another at $\mathbf{r}_2$ is determined by the diagonal elements of the second-order density matrix:

$$n(\mathbf{r}_1,\mathbf{r}_2) = N(N-1)\int ... \int d\mathbf{r}_3 ... \mathbf{r}_N \, |\Psi(\mathbf{r}_1,\mathbf{r}_2,\mathbf{r}_3,...,\mathbf{r}_N)|^2. \tag{2.18}$$

For non-interacting particles, this probability factorizes into a product of independent events. In reality, however, because electrons carry charge and spin, the presence of one electron modifies the probability of finding the other:

$$n(\mathbf{r}_1, \mathbf{r}_2) = n(\mathbf{r}_1)\, n(\mathbf{r}_2) + n(\mathbf{r}_1)\, h_{xc}(\mathbf{r}_1, \mathbf{r}_2), \tag{2.19}$$

where $h_{xc}(\mathbf{r}_1, \mathbf{r}_2)$ is the exchange–correlation hole, which quantifies the change in the probability of finding electron 2 at $\mathbf{r}_2$ given that electron 1 is located at $\mathbf{r}_1$. This concept is often interpreted as an interaction of each electron with an effective positive charge cloud surrounding it, which lowers the total energy. The function $h_{xc}(\mathbf{r}_1, \mathbf{r}_2)$ must satisfy several constraints:

$$h_{xc} = h_x + h_c \tag{2.20}$$

$$\int h_x(\mathbf{r}_1, \mathbf{r}_2) d\mathbf{r}_2 = \int \frac{n_2(\mathbf{r}_1, \mathbf{r}_2)}{n(\mathbf{r}_1)} d\mathbf{r}_1 d\mathbf{r}_2 - \int n(\mathbf{r}_2) d\mathbf{r}_2 = \frac{N(N-1)}{N} - N = -1 \tag{2.21}$$

$$h_x(\mathbf{r}_1, \mathbf{r}_2) \leqslant 0 \tag{2.22}$$

$$\int h_c(\mathbf{r}_1, \mathbf{r}_2)\, d\mathbf{r}_2 = 0, \tag{2.23}$$

where h_x and h_c denote exchange and correlation holes, respectively. The exchange hole describes a static reduction in probability corresponding to one electron. The correlation hole reduces the probability of finding electron 2 near electron 1, while increasing the probability of finding it far away.

In HFA, the exchange energy is a non-local functional, i.e., the exchange hole is delocalized over the entire system. For example, in a diatomic molecule the exchange hole is delocalized over both nuclei. When electron correlation is treated explicitly, it largely acts to remove this delocalized character of the exchange hole. By contrast, the exchange functional in DFT is typically local; therefore, the compensation of the delocalized Hartree–Fock exchange hole by correlation must be embedded in the XC-functional itself. This is one of the key differences between wave-function-based and density-based definitions of exchange and correlation.

In addition, the Hartree term depends only on the sum of the diagonal elements of the first-order density matrix. Consequently, the charge density associated with a given electron interacts with the electron itself, implying a non-zero Coulomb repulsion even for one-electron systems. This is the self-interaction error. In HFA, this problem is removed automatically because the exchange integral exactly cancels the self-interaction contribution of the Coulomb term. In a many-electron system, the exchange energy therefore contains both the self-interaction correction and the contribution associated with the "true" exchange hole, which is comparable in magnitude to correlation [90]. A similar idea is employed in DFT; however, complete self-interaction cancellation is not guaranteed, since it has been shown that no strictly local functional can eliminate self-interaction exactly. [91]

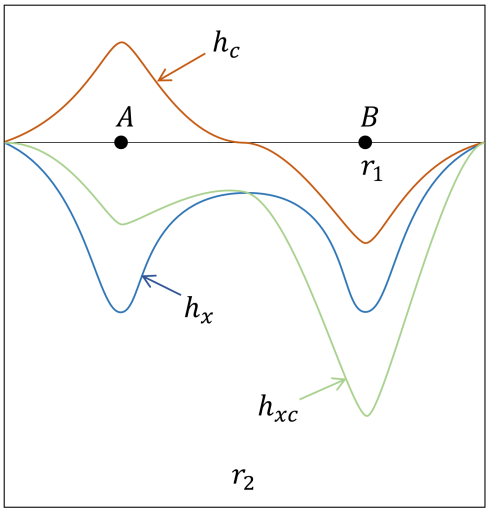

Figure 2.4: Schematic representation of the exchange–correlation hole

To illustrate this concept, consider the hydrogen molecule in Fig. 2.4. The position of electron 1 is treated as a parameter. The spatial wave functions of the two electrons are identical, while their spin states are different. In this case, h_x primarily compensates self-interaction: for one of the electrons, the exchange hole corresponds to one half of the squared bonding molecular-orbital wave function. Consequently, h_x is delocalized and reduces the electron density by "half an electron" in the vicinity of each nucleus. Note that the exchange hole is invariant with respect to the position of electron 1. Importantly, as the internuclear distance increases, the shape of h_x does not change, which in this limit introduces additional screening between electron 2 and its nearest nucleus (A).

The correlation hole is predominantly negative near electron 1 due to electrostatic repulsion. Far from electron 1, h_c becomes positive, satisfying condition (2.23). In the present example, there are no contributions from parallel spins, and h_c arises solely from interactions between antiparallel-spin electrons. If one electron is located near nucleus A, the probability of finding the other near nucleus B increases, and vice versa. This effect becomes more pronounced as the two atoms are separated. Thus, the Coulomb (correlation) hole is also delocalized: it has a negative part around nucleus B, where electron 1 is located, and a positive part around the other nucleus. Upon dissociation, the correlation hole compensates "half an electron" at nucleus A and transfers it to the other nucleus. This behavior differs from that of h_x, which does not depend on where electron 1 is located.

2.1.6.2 Uniform Electron Gas

Most exchange–correlation functionals are constructed using the theory of the uniform electron gas. In this model, electrons move in a uniform background of positive charge that ensures overall charge neutrality. The system is considered in the thermodynamic limit, where both the number of particles and the volume tend to infinity at fixed electron density.

In practice, this model is far from realistic, because atoms and molecules typically exhibit large density gradients. Nevertheless, the exchange and correlation energies are known with high accuracy only for the uniform electron gas.

Within the Hartree–Fock approximation, a plane wave is an eigenfunction of the exchange operator with eigenvalue

$$\varepsilon_x(k) = -\frac{k_F}{\pi} f(x), \qquad x = k/k_F \tag{2.24}$$

$$f(x) = 1 + \frac{1-x^2}{2x} \ln\left|\frac{1+x}{1-x}\right|. \tag{2.25}$$

The exchange energy per electron in an unpolarized system is obtained by averaging $f(x)$ over the Fermi sphere, which yields $-3/2$:

$$\epsilon_x = -\frac{3}{4\pi} k_F = -\frac{3}{4}\left(\frac{3}{\pi}\right)^{1/3} n^{1/3}. \tag{2.26}$$

The correlation hole and the correlation energy cannot be obtained analytically. To evaluate the correlation energy ε_c of the uniform electron gas, diagrammatic many-body techniques are typically employed. These methods sum infinite series of contributions associated with many-body diagrams and interpolate between the high- and low-density limits. Many parameterizations of ε_c with varying accuracy have been proposed. The most successful ones reproduce quantum Monte Carlo calculations, where the many-body interaction problem is treated explicitly.

2.1.6.3 Local Density Approximation

The local density approximation (LDA) is historically the first and simplest class of exchange–correlation functionals. Its central assumption is that, within an infinitesimal volume element, the electron density can be regarded as constant, and the exchange–correlation energy density is

equal to that of a uniform electron gas with the same density. The exchange–correlation energy is then written as

$$E_{xc}^{LDA}[n(\mathbf{r})] = \int d\mathbf{r}\, n(\mathbf{r})\, \varepsilon_{xc}(n(\mathbf{r})). \tag{2.27}$$

This assumption is rather crude, because the electron density in real materials is generally far from homogeneous, and these inhomogeneities should be taken into account to obtain accurate energies. Nevertheless, LDA performs remarkably well for many systems. The LDA exchange and correlation holes satisfy the exact constraints 2.21, 2.22, and 2.23. The LDA exchange energy is given by

$$E_{x}^{LDA} = -\frac{3}{4}\left(\frac{3}{\pi}\right)^{1/3} \int d\mathbf{r}\, n(\mathbf{r})^{4/3}. \tag{2.28}$$

As noted above, there is no analogous explicit analytical expression for the correlation energy. However, Ceperley and Alder[92] reported accurate quantum Monte Carlo results for the uniform electron gas. Based on these data, several authors proposed parameterized expressions for ε_c using interpolation schemes. Among the most widely used parameterizations are those by Vosko, Wilk, and Nusair[93] and by Perdew and Wang[94]. One of the earlier parameterizations, proposed by Hedin and Lundqvist[95], reads

$$\varepsilon_{c}^{HL}(r_s) = -\frac{C}{2}\left[(1+x^3)\ln\left(1+\frac{1}{x}\right) + \frac{x}{2} - x^2 - \frac{1}{3}\right], \tag{2.29}$$

where $A = 21$, $C = 0.045$, and $x = r_s/A$. The corresponding correlation potential is given by

$$V_{c}^{HL}(r_s) = -\frac{Ce^2}{2}\ln\left(1+\frac{1}{x}\right). \tag{2.30}$$

Figure 2.5 provides a schematic interpretation of the approximation. In the vicinity of a point $\mathbf{r}$, the electron density is assumed to be constant and is mapped to the exchange–correlation energy of a uniform electron gas with the same density. Integrating these contributions over space yields the exchange–correlation energy corresponding to the given inhomogeneous density.

LDA is most accurate for systems with slowly varying electron densities. It typically overbinds, leading to lattice constants that are slightly underestimated. This behavior is usually attributed to a partial cancellation between exchange and correlation errors.

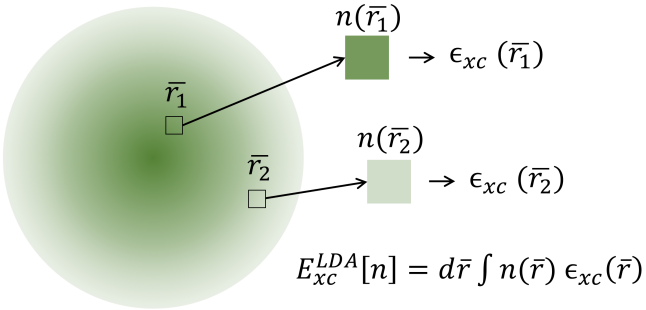

Figure 2.5: Schematic illustration of the local density approximation.

2.1.6.4 Generalized Gradient Approximation

The electron density in most real systems is strongly inhomogeneous. Introducing gradient corrections to the LDA exchange–correlation functional led to the generalized gradient approximation (GGA), a class of semilocal exchange–correlation functionals. These functionals are mathematically more complex and, to some extent, less physically transparent, because their forms were constructed to satisfy known exact constraints such as (2.21), (2.22), and (2.23):

$$E_{xc}^{GGA}[n] = \int d\mathbf{r}\, n(\mathbf{r})\, \varepsilon_x^{hom}(n)\, F_{xc}(n^{\uparrow}, n^{\downarrow}, |\nabla n^{\uparrow}|, |\nabla n^{\downarrow}|). \tag{2.31}$$

For exchange, the spin-scaling relation holds:

$$E_x[n_{\uparrow}, n_{\downarrow}] = \frac{1}{2}\left(E_x[2n_{\uparrow}] + E_x[2n_{\downarrow}]\right), \tag{2.32}$$

so that it is sufficient to consider the spin-unpolarized case $F_x(n, \nabla n)$. In practice, it is customary to introduce the reduced density gradient

$$s = \frac{|\nabla n|}{2k_F n} = \frac{|\nabla n|}{2(3\pi^2)^{1/3} n^{4/3}} = \frac{|\nabla r_s|}{2(9\pi/4)^{1/3}}. \tag{2.33}$$

In the Perdew–Burke–Ernzerhof (PBE) parameterization[96], the exchange enhancement factor is defined as

$$F_x(s) = 1 + \kappa - \frac{\kappa}{1 + \mu s^2/\kappa}, \tag{2.34}$$

where $\mu = 0.21951$ and $\kappa = 0.804$. These values are chosen to satisfy several exact constraints, including the Lieb–Oxford lower bound[97]

$$E_{xc}[n_\uparrow, n_\downarrow] \geq -C_{LO} \int d\mathbf{r}\, n^{4/3}(\mathbf{r}), \tag{2.35}$$

where $C_{LO} \approx 1.679$.

In the regime of small gradients, which is relevant for many physical systems, different forms of F_x yield similar results. More importantly, because $F_x \geq 1$, the magnitude of the exchange energy in GGA is smaller than in LDA. Typically, density variations are more rapid in atoms than in molecules and solids, leading to a larger reduction of exchange in atoms. As a result, GGA predicts smaller binding energies than LDA and often improves agreement with experiment, which is one of its main advantages.

In the large-gradient regime, however, different choices of F_x—constructed to satisfy only a subset of physical constraints—can yield substantially different results, implying that the functional must be chosen with care for the properties of interest.

The correlation contribution is described by more complicated expressions, but its magnitude is usually smaller than that of exchange. In GGA, the correlation functional takes the form

$$E_c^{GGA}[n_\uparrow, n_\downarrow] = \int d\mathbf{r}\, n(\mathbf{r}) \left[\varepsilon_c^{hom}(r_s, \zeta) + H(r_s, \zeta, t)\right], \tag{2.36}$$

where $\zeta = (n_\uparrow - n_\downarrow)/n$ is the relative spin polarization, $t = |\nabla n|/(2\phi k_s n)$ is a dimensionless density gradient, $\phi(\zeta) = [(1+\zeta)^{2/3} + (1-\zeta)^{2/3}]/2$, and $k_s = \sqrt{4k_F/\pi a_0}$.

Unfortunately, no single GGA exchange–correlation functional can describe both atomistic and molecular properties (total energies, atomization energies, etc.) and the properties of solids with uniformly high accuracy. These applications require somewhat different forms of $F_{xc}(r_s, s)$. The original PBE functional was designed primarily for molecular and atomistic systems. A modified functional tailored to solids was proposed by Perdew *et al.*[98]. The PBEsol functional yields significantly improved lattice constants as well as more accurate surface and other solid-state properties.

2.1.7 Hubbard correction

As is well known, standard DFT is unable to properly describe Mott insulators. In such systems, the potential energy associated with electron–electron interactions (due to Coulomb repulsion)

dominates over the kinetic energy, driving the electrons to localize in states that resemble atomic orbitals.[99] Describing this physics generally requires multi-determinant approaches, in which the weights of configurations of different character (e.g., ionic versus covalent) can be redistributed. In contrast, widely used exchange–correlation functionals tend to over-delocalize valence electrons and thereby spuriously stabilize a metallic state. This deficiency is related both to the intrinsic difficulty of representing strongly correlated electronic states within common approximations and to the incomplete cancellation of self-interaction arising from the classical Hartree term.

One of the simplest models introduced to address these limitations is the Hubbard model[100–105]. In the language of second quantization, the Hubbard Hamiltonian can be written as:

$$H_{\mathrm{Hubbard}} = t \sum_{\langle i,j\rangle,\sigma} (c^{\dagger}_{i,\sigma} c_{j,\sigma} + h.c.) + U \sum_{i} n_{i,\uparrow}, n_{i,\downarrow} \tag{2.37}$$

where $\langle i, j\rangle$ denotes atomic sites, $c^{\dagger}_{i,\sigma}$, $c_{i,\sigma}$ and $n_{i,\sigma}$ are creation, annihilation and particle number operators for electrons of spin σ on site i.

The insulating behavior emerges when the intersite hopping amplitude t, which favors delocalization, is suppressed by the short-range Coulomb interaction U (typically $t \ll U$). The delocalized, hopping-dominated regime is generally well described by DFT as a largely single-particle framework, whereas the strongly correlated regime requires more advanced methods beyond standard DFT approximations.

Within LDA+U the total energy of a system can be written as follows:

$$E_{\mathrm{LDA+U}}[\rho(r)] = E_{\mathrm{LDA}}[\rho(r)] + E_{\mathrm{Hub}}[\{n^{I\sigma}_{mm'}\}] - E_{\mathrm{dc}}[\{n^{I\sigma}\}], \tag{2.38}$$

where E_{Hub} contains electron-electron interaction as modeled in Hubbard Hamiltonian. Because the energy functional already contains a contribution corresponding to interactions of this type, an additional term E_{dc} must be subtracted to avoid double counting. This correction is usually derived within a mean-field treatment of the correlated electrons. Since DFT lacks an exact diagrammatic formulation, more than one reasonable form of such a double-counting term may exist. It should also be emphasized that the correction is applied specifically to selected localized states of the system. Therefore, the formulation explicitly involves a localized basis of atomic-like states. $n^{I\sigma}_{mm'}$ – occupation numbers that are often defined as projections of occupied Kohn-Sham orbitals on the states of a localized basis set.

The LDA+U approach was first introduced in[106–108] and consisted of an energy functional that, when specialized to on-site interactions, can be written as follows:

$$E = E_{\mathrm{LDA}} + \sum_I \left[\frac{U^I}{2} \sum_{m,\sigma \neq m',\sigma'} n_m^{I\sigma} n_{m'}^{I\sigma'} - \frac{U^I}{2} n^I (n^I - 1) \right]. \tag{2.39}$$

where $n_m^{I\sigma} = n_{mm}^{I\sigma}$ and $n^I = \sum_{m,\sigma} n_m^{I\sigma}$. The second and the third terms of the right-hand side of this equation reprsent, respectively, the Hubbard and the double-counting terms of 2.38.

Although DFT+U often shifts localized d/f states and can substantially improve the electronic structure relative to LDA/GGA DFT, it does not open a band gap automatically. A gap appears only if degeneracies (or near-degeneracies) of the localized states at the Fermi level are lifted, so that these states can separate into fully occupied and fully unoccupied manifolds. Such lifting typically requires symmetry breaking (e.g., magnetic order, crystal-field/Jahn–Teller distortions, or spin–orbit coupling) that enables orbital or spin polarization.

A simpler expression for the Hubbard correction was adopted and further simplified in this work[109]. While remaining rotationally invariant, the resulting formulation can be written as

$$\begin{aligned} E_U[\{n_{mm'}^{I\sigma}\}] &= E_{\mathrm{Hub}}[\{n_{mm'}^{I}\}] - E_{\mathrm{dc}}[\{n^I\}] \\ &= \sum_I \frac{U^I}{2} \left[\left(n^I\right)^2 - \sum_\sigma \mathrm{Tr}\left[\left(\mathbf{n}^{I\sigma}\right)^2 \right] \right] - \sum_I \frac{U^I}{2} n^I (n^I - 1) \\ &= \sum_{I,\sigma} \frac{U^I}{2} \mathrm{Tr}\left[\mathbf{n}^{I\sigma} \left(1 - \mathbf{n}^{I\sigma} \right) \right]. \end{aligned} \tag{2.40}$$

However, this is still insufficient to describe noncollinear magnetism and to capture correlation effects in multiband metals. Since the simplified approach is spin-diagonal, it is customary to assign the Coulomb interaction an effective value that incorporates the exchange correction, U_{eff}=U – J.

2.2 Statistical Mechanics

A common starting point for virtually all statistical-mechanics methods used to model classical many-particle systems is the ensemble average of an observable A:

$$\langle A \rangle = \frac{\int \mathrm{d}\mathbf{r}^N \int \mathrm{d}\mathbf{p}^N \, A(\mathbf{r}^N, \mathbf{p}^N) \exp\left[-\beta \left(\sum_{i=1}^N \frac{\mathbf{p}_i^2}{2m_i} + U(\mathbf{r}^N) \right) \right]}{\int \mathrm{d}\mathbf{r}^N \int \mathrm{d}\mathbf{p}^N \, \exp\left[-\beta \left(\sum_{j=1}^N \frac{\mathbf{p}_j^2}{2m_j} + U(\mathbf{r}^N) \right) \right]}, \tag{2.41}$$

where N is the number of particles in the system, $\mathbf{p}$ denotes momenta, $\mathbf{r}$ denotes coordinates, $\beta = 1/(k_B T)$, U is the potential-energy function, and m is the particle mass. Because the kinetic-energy term is a quadratic function of the momenta, the integration over momenta can, in most cases, be carried out analytically. The remaining challenge is the evaluation of ensemble averages of observables that depend only on the coordinates, i.e., quantities of the form $A(\mathbf{r}^N)$. Therefore, the primary focus is placed on the configurational integral. In practice, such integrals are evaluated either by time averaging along a trajectory (the molecular-dynamics approach) or by ensemble averaging through stochastic sampling (the Monte Carlo approach).

2.2.1 Quantum Molecular Dynamics

Among the most advanced first-principles approaches for computing materials properties is quantum molecular dynamics (QMD), which has substantially broadened the scope of atomistic studies of solids, liquids, and gases. The method allows us to follow the real-time evolution of an atomic system in a supercell, which remains extremely challenging to access experimentally. As a result, a wide range of material properties can be obtained without resorting to empirical potentials as in classical molecular dynamics. In particular, QMD enables one to account for anharmonic effects in calculations of thermal properties of crystals and liquids, and to elucidate mechanisms of complex catalytic reactions.[110]

In QMD simulations, atoms with a prescribed density are placed in a supercell of volume Ω. Periodic boundary conditions are imposed, such that any particle leaving the cell re-enters through the opposite face. This ensures a constant number of atoms in the simulation.

At each ionic step of the QMD simulation, the electronic structure is computed within density functional theory under the Born–Oppenheimer approximation, i.e., the electrons are assumed to adjust instantaneously to the current ionic configuration due to the large mass disparity. The ions are treated classically, and the forces exerted on the ions by the electrons are evaluated using the Hellmann–Feynman theorem:

$$\mathbf{F}_I = -\frac{\partial E}{\partial \mathbf{R}_I} = -\int d\mathbf{r}\, n(\mathbf{r}) \frac{\partial V_{ext}(\mathbf{r})}{\partial \mathbf{R}_I} - \frac{\partial E_{II}}{\partial \mathbf{R}_I}. \tag{2.42}$$

To control the temperature, a thermostat at temperature T_I may be employed; it, in turn, influences the ionic dynamics. The kinetic energy then fluctuates around its mean value:

$$E_I^{\mathrm{kin}} = \frac{3}{2}(N_{\mathrm{atoms}} - 1) k_B\, T_I. \tag{2.43}$$

This set of equations cannot be solved analytically, and therefore numerical methods based on discretized equations of motion are used, for example, the Verlet algorithm. At each time step t, the current ionic positions determine the positions at the next step $t + \Delta t$ together with the forces exerted by the electrons at the current time:

$$\mathbf{R}_I(t + \Delta t) = 2\mathbf{R}_I(t) - \mathbf{R}_I(t - \Delta t) + \frac{(\Delta t)^2}{M_I}\mathbf{F}_I[\{\mathbf{R}_J(t)\}]. \tag{2.44}$$

A key feature of this algorithm is that, in classical simulations, numerical errors do not accumulate systematically. Although the equations of motion are approximate for any finite Δt, this does not lead to a drift in the total energy, and the simulation remains stable over relatively long time spans.

In QMD, the electronic problem is solved for each instantaneous nuclear configuration to obtain the total energy (and forces), which are then used to propagate the ionic positions and velocities; the resulting trajectories $\mathbf{R}_{\mathrm{at}}(t)$ and velocities are recorded. In computing the nucleus–nucleus interaction energy (the Ewald energy), the presence of periodic replicas of the simulation supercell is taken into account due to the infinite extent of the modeled structure. After a certain number of steps, the total energy reaches an equilibrium plateau and subsequently fluctuates as a result of coupling to the thermostat. At each ionic step, the kinetic contribution of the ions to the pressure is also recorded; it fluctuates around a mean value:

$$p_I^{kin}(t) = \frac{N_{at} - 1}{\Omega} kT_I. \tag{2.45}$$

Because the ionic dynamics is governed not only by the Hellmann–Feynman forces but also by the thermostat settings, the resulting time evolution should not be interpreted as a strictly physical trajectory. Nevertheless, once equilibrium is reached, the sampled ionic configurations are generally assumed to be representative of physically realizable states under the given conditions. Accordingly, the thermodynamic quantities averaged over the equilibrium portion of the trajectory are treated as equilibrium values for these conditions.

2.2.2 Monte Carlo method

In this chapter, we consider the Monte Carlo method, which enables efficient sampling of phase space and allows ensemble averages to be evaluated. In practice, the dimensionality of phase space grows as m^{DN}, where m is the number of equidistant grid points along a single axis, D is the spatial dimension, and N is the number of particles. Moreover, for the vast majority

of these points the Boltzmann factor is essentially zero, implying that they do not contribute to the integral. Consequently, uniform sampling of phase space is inefficient, and one should instead exploit the fact that the system is distributed according to a probability density for finding a configuration in the vicinity of a point $\mathbf{r}^N$. This density is given by the Boltzmann weight divided by the partition function. A practical difficulty arises because the partition function is generally unknown. Therefore, Monte Carlo sampling is formulated in terms of relative, rather than absolute, probabilities.[111]

Consider the Metropolis scheme for constructing the transition probability $\pi(o \to n)$ from an old configuration o to a new configuration n. At equilibrium, the average number of accepted transitions from state o to state n is exactly compensated by the number of reverse transitions. This is the detailed-balance (detailed-equilibrium) condition:

$$P(o)\,\pi(o \to n) = P(n)\,\pi(n \to o), \tag{2.46}$$

where $P(\cdot)$ denotes the equilibrium probability of a configuration.

A single Monte Carlo step consists of two stages. First, a trial move from o to n is proposed; the probability of generating this trial move is denoted by $\alpha(o \to n)$. Second, the trial move is either accepted or rejected with an acceptance probability $\mathrm{acc}(o \to n)$. Accordingly, the overall transition probability can be written as

$$\pi(o \to n) = \alpha(o \to n) \cdot \mathrm{acc}(o \to n). \tag{2.47}$$

Assuming that the proposal probability is symmetric, i.e., $\alpha(o \to n) = \alpha(n \to o)$, the detailed-balance condition can be rewritten as

$$\frac{\mathrm{acc}(o \to n)}{\mathrm{acc}(n \to o)} = \frac{P(n)}{P(o)}. \tag{2.48}$$

Within the Metropolis–Hastings framework, these acceptance probabilities are chosen as follows:

$$\mathrm{acc}(o \to n) = \begin{cases} P(n)/P(o), & P(n) < P(o), \\ 1, & P(n) \geq P(o). \end{cases} \tag{2.49}$$

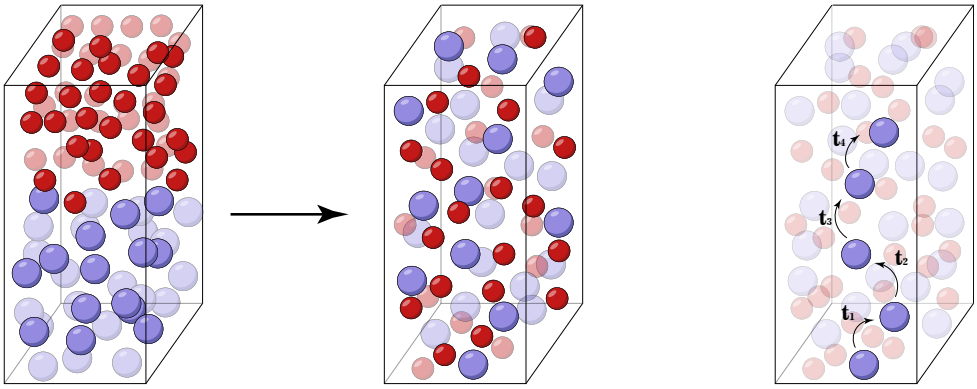

Metropolis-Hastings algorithm **Kinetic Monte Carlo**

Figure 2.6: The difference between the two Monte Carlo methods. The illustration highlights the different goals of these two approaches: one for studying thermodynamic properties, the other for kinetic properties.

The Metropolis algorithm defines a transition matrix

$$\pi(o \to n) = \alpha(o \to n)\,\mathrm{acc}(o \to n),$$

so that the resulting sequence of configurations $\{o_k\}$ forms a Markov chain: the distribution of the next state depends only on the current one. For a symmetric proposal probability α, choosing

$$\mathrm{acc}(o \to n) = \min\left[1, \frac{N(n)}{N(o)}\right]$$

ensures detailed balance,

$$N(o)\,\pi(o \to n) = N(n)\,\pi(n \to o),$$

and therefore the distribution $N \propto e^{-\beta U}$ is stationary for the chain.

In kinetic Monte Carlo (KMC), transitions also constitute a Markov process; however, instead of dimensionless probabilities π, one assigns physical event rates $k_{o\to n}$, which makes it possible to relate the evolution to real time. An event is then selected with probability proportional to $k_{o\to n}$, and the time increment Δt is sampled from an exponential distribution with parameter $\sum_n k_{o\to n}$. As a result, the generated trajectory describes kinetic evolution (rather than merely equilibrium sampling).

2.2.3 Quasi-Harmonic Approximation

One of the most widely used approaches for describing lattice dynamics is the quasi-harmonic approximation (QHA).[112] Its discussion is typically introduced by first considering the harmonic approximation (HA). Within the HA, the equations of motion for small displacements can be written in linear form. Let $\mathbf{u}(jl;t)$ denote the displacement of atom j in unit cell l from its equilibrium position. The harmonic equations of motion read as follows:

$$M_j \ddot{u}_\alpha(jl;t) = -\sum_{j'l'\beta} \Phi_{\alpha\beta}(jl;j'l')\, u_\beta(j'l';t), \tag{2.50}$$

where M_j is the mass of the atom j and $\alpha, \beta \in \{x, y, z\}$ are Cartesian components.

In this framework, the potential energy in the vicinity of the equilibrium configuration is expanded in a Taylor series, and the lattice dynamics is fully determined by the second-order (harmonic) force constants:

$$\Phi_{\alpha\beta}(jl;j'l') = \frac{\partial^2 U}{\partial r_\alpha(jl)\partial r_\beta(j'l')} = -\frac{\partial F_\beta(j'l')}{\partial r_\alpha(jl)}, \tag{2.51}$$

which quantify the force acting on atom j' in unit cell l' when atom j in unit cell l is displaced by an amount r_α.

Two main approaches are commonly used to compute second-order force constants: the finite-displacement method[113] and density-functional perturbation theory (DFPT).[114,115] In the finite-displacement approach, derivatives are evaluated by finite differences. This requires generating a set of symmetrically inequivalent structures with displaced atoms, exploiting crystal symmetry to reduce the number of calculations. Two variants are typically employed: one can evaluate forces (or energies) for both the equilibrium and displaced configurations to form the finite-difference derivatives, or one can determine the force constants by solving a system of linear equations using a modified Parlinski–Li–Kawazoe procedure, which reduces the required number of configurations by one. In either case, the results depend on the chosen displacement amplitude, which is usually taken as a single fixed value throughout the calculation (hyperparameter). In DFPT, by contrast, the Sternheimer equation is solved to obtain the linear response of the electronic system to an external perturbation (not necessarily an atomic displacement). This is often numerically more robust, because in many cases small variations can be computed more accurately than total-energy differences themselves.

Introducing a plane-wave ansatz for atomic displacements leads to an eigenvalue problem defined by the dynamical matrix:

$$u_\alpha(lj;t) = \frac{1}{\sqrt{M_j}}\, e_\alpha(j;\mathbf{q}\nu)\, \exp\big[i(\mathbf{q}\cdot\mathbf{R}_l - \omega_{\mathbf{q}\nu}t)\big], \tag{2.52}$$

$$\sum_{j'\beta} D_{\alpha\beta}(jj';\mathbf{q})\, e_\beta(j';\mathbf{q}\nu) = \omega^2_{\mathbf{q}\nu}\, e_\alpha(j;\mathbf{q}\nu), \tag{2.53}$$

where ν labels the phonon branch and $e_{j\alpha}(\mathbf{q}\nu)$ is the polarization vector. The dynamical matrix is given by the mass-weighted Fourier transform of the force constants,

$$D_{\alpha\beta}(jj';\mathbf{q}) = \frac{1}{\sqrt{M_j M_{j'}}} \sum_{l'} \Phi_{\alpha\beta}(j0;j'l')\, \exp\big[i\mathbf{q}\cdot(\mathbf{r}(j'l') - \mathbf{r}(j0))\big], \tag{2.54}$$

with $\mathbf{r}(j'l')$ denoting the atom j' in the cell l'. The eigenvalues of $D(\mathbf{q})$ yield the phonon frequencies $\omega_{\mathbf{q}\nu}$, while the corresponding eigenvectors define the phonon modes. In particular, negative eigenvalues imply $\omega^2_{\mathbf{q}\nu} < 0$ and thus imaginary frequencies, indicating a dynamical instability of the reference structure.

Within the harmonic approximation, lattice vibrations can be expressed in terms of normal modes. Let $\mathbf{u}_{lj}(t)$ be the displacement of atom j in unit cell l from equilibrium. Using the eigenvectors $e_{j\alpha}(\mathbf{q}\nu)$ of the dynamical matrix, the displacement field can be expanded as

$$u_\alpha(lj;t) = \frac{1}{\sqrt{N_c M_j}} \sum_{\mathbf{q}\nu} Q_{\mathbf{q}\nu}(t)\, e_\alpha(j;\mathbf{q}\nu)\, \exp\big[i\mathbf{q}\cdot\mathbf{r}(jl)\big], \tag{2.55}$$

where N_c is the number of unit cells in the supercell, and $Q_{\mathbf{q}\nu}$ are normal coordinates.

In these variables, the harmonic lattice Hamiltonian becomes a sum of independent oscillators,

$$H^{\mathrm{HA}}_{\mathrm{vib}} = \sum_{\mathbf{q}\nu} \left[\frac{P^2_{\mathbf{q}\nu}}{2} + \frac{1}{2}\,\omega^2_{\mathbf{q}\nu}\, Q^2_{\mathbf{q}\nu} \right], \tag{2.56}$$

where $\omega_{\mathbf{q}\nu}$ are phonon frequencies obtained from the dynamical matrix, and $P_{\mathbf{q}\nu}$ are the conjugate momenta.

Quantization of each normal mode yields a bosonic spectrum (phonons),

$$H^{\mathrm{HA}}_{\mathrm{vib}} = \sum_{\mathbf{q}\nu} \hbar\omega_{\mathbf{q}\nu} \left(\hat{a}^\dagger_{\mathbf{q}\nu}\hat{a}_{\mathbf{q}\nu} + \frac{1}{2} \right), \tag{2.57}$$

with $\hat{a}^{\dagger}_{\mathbf{q}\nu}$ and $\hat{a}_{\mathbf{q}\nu}$ the creation and annihilation operators. The mean phonon occupation number is given by the Bose–Einstein distribution,

$$\langle n_{\mathbf{q}\nu} \rangle = \frac{1}{\exp(\beta\hbar\omega_{\mathbf{q}\nu}) - 1}, \qquad \beta = \frac{1}{k_B T}. \tag{2.58}$$

The vibrational partition function factorizes over modes,

$$Z_{\mathrm{vib}} = \prod_{\mathbf{q}\nu} \frac{\exp(-\beta\hbar\omega_{\mathbf{q}\nu}/2)}{1 - \exp(-\beta\hbar\omega_{\mathbf{q}\nu})}, \tag{2.59}$$

and the vibrational (phonon) contribution to the Helmholtz free energy is

$$F_{\mathrm{vib}}(T) = -k_B T \ln Z_{\mathrm{vib}} = \sum_{\mathbf{q}\nu} \left[\frac{1}{2}\hbar\omega_{\mathbf{q}\nu} + k_B T \ln\!\left(1 - e^{-\beta\hbar\omega_{\mathbf{q}\nu}}\right) \right]. \tag{2.60}$$

An equivalent compact form is

$$F_{\mathrm{vib}}(T) = k_B T \sum_{\mathbf{q}\nu} \ln\left[2\sinh\left(\frac{\beta\hbar\omega_{\mathbf{q}\nu}}{2} \right) \right]. \tag{2.61}$$

In the quasi-harmonic approximation, the phonon frequencies depend on volume, $\omega_{\mathbf{q}\nu} = \omega_{\mathbf{q}\nu}(V)$, thereby incorporating the leading effect of thermal expansion. The total Helmholtz free energy is written as

$$F(T, V) = E_{\mathrm{lat}}(V) + F_{\mathrm{vib}}(T, V), \tag{2.62}$$

where $E_{\mathrm{lat}}(V)$ is the $T = 0$ electronic ground-state energy for a given volume. At fixed pressure, the Gibbs free energy is obtained via

$$G(T, P) = \min_{V} \left[F(T, V) + PV \right]. \tag{2.63}$$

2.2.4 Moment Tensor Potential

The Moment Tensor Potential[116–119] is a polynomial class of interatomic interaction potentials that allows for efficient and rapid calculation of the energy of an atomic configuration. The potential energy of a system is defined as the sum of the local atomic environments of each atom $\mathfrak{n}_i$:

$$E^{\mathrm{mtp}}(\mathrm{cfg}) = \sum_{i=1}^{n} V(\mathfrak{n}_i), \tag{2.64}$$

where the function $V(\mathfrak{n}_i)$ is expanded in the basis functions $B_\alpha(\mathfrak{n}_i)$ with learnable parameters ξ_α:

$$V(\mathfrak{n}_i) = \sum_{\alpha} \xi_\alpha B_\alpha(\mathfrak{n}_i). \tag{2.65}$$

The basis functions are defined using moment tensor descriptors:

$$M_{\mu,\nu}(\mathfrak{n}_i) = \sum_{j} f_\mu(|\mathbf{r}_{ij}|, z_i, z_j) \underbrace{\mathbf{r}_{i,j} \otimes \ldots \otimes \mathbf{r}_{i,j}}_{\nu \text{ times}} \tag{2.66}$$

These descriptors consist of the angular and radial part. The radial part is defined as follow:

$$f_\mu(|\mathbf{r}_{ij}|, z_i, z_j) = \sum_{\beta=1}^{N_Q} c^{(\beta)}_{\mu,z_i,z_j} Q^{(\beta)}(|\mathbf{r}_{ij}|), \tag{2.67}$$

where $Q^{(\beta)}$ is given by:

$$Q^{(\beta)}(|\mathbf{r}_{i,j}|) = \begin{cases} \varphi^{(\beta)}(|\mathbf{r}_{i,j}|)(R_{cut} - |\mathbf{r}_{i,j}|), & |\mathbf{r}_{ij}| < 0, \\ 0, & |\mathbf{r}_{ij}| \geq 0. \end{cases} \tag{2.68}$$

The size of the base set is determined by the so-called potential level, which in turn depends on μ and ν:

$$\mathrm{lev} M_{\mu,\nu} = 2 + 4\mu + \nu. \tag{2.69}$$

Finally, to specify a particular MTP functional form, we set the maximum level $\mathrm{lev}_{\max}$ and retain all basis functions with levels that do not exceed this value:

$$\mathrm{lev} B_\alpha \leq \mathrm{lev}_{\max} \tag{2.70}$$

For instance, if we choose $\mathrm{lev}_{\max}$ = 8 then there are nine basis functions B_α:

$$\begin{aligned}
B_1 &= M_{0,0} & \mathrm{lev}B_1 &= 2 \\
B_2 &= M_{1,0} & \mathrm{lev}B_2 &= 6 \\
B_3 &= M_{0,0}^2 & \mathrm{lev}B_3 &= 4 \\
B_4 &= M_{0,1} \cdot M_{0,1} & \mathrm{lev}B_4 &= 6 \\
B_5 &= M_{0,2} : M_{0,2} & \mathrm{lev}B_5 &= 8 \\
B_6 &= M_{0,0} M_{1,0} & \mathrm{lev}B_6 &= 8 \\
B_7 &= M_{0,0}^3 & \mathrm{lev}B_7 &= 6 \\
B_8 &= M_{0,0}(M_{0,1} \cdot M_{0,1}) & \mathrm{lev}B_8 &= 8 \\
B_9 &= M_{0,0}^4 & \mathrm{lev}B_9 &= 8
\end{aligned} \tag{2.71}$$

2.2.5 Linear responce theory

Although molecular dynamics is typically used to probe systems at equilibrium, transport properties can also be obtained from equilibrium trajectories via linear-response theory. The central idea goes back to Onsager (1931), who hypothesized that spontaneous fluctuations of a system in equilibrium regress in time according to the same laws that govern the relaxation of macroscopic deviations from equilibrium[120].

Consider a system prepared under a very weak and constant external perturbation. At time $t = 0$, the perturbation is suddenly switched off. We then monitor the time evolution of an observable, i.e., the value of a dynamical variable:

$$\langle \Delta A(t) \rangle = \frac{\int d\Gamma \exp\left[-\beta(\mathcal{H}_0 - \lambda B)\right] A(t)}{\int d\Gamma \exp\left[-\beta(\mathcal{H}_0 - \lambda B)\right]} \tag{2.72}$$

Let us expand $\exp\left[-\beta(-\lambda B)\right]$ over λ at $\lambda \to 0$:

$$\langle \Delta A(t) \rangle = \frac{\int d\Gamma \exp\left[-\beta(\mathcal{H}_\prime)\right] A(t) \left(1 + \beta\lambda B + \mathcal{O}(\lambda^2)\right)}{\int d\Gamma \exp\left[-\beta(\mathcal{H}_\prime\right] \left(1 + \beta\lambda B + \mathcal{O}(\lambda^2)\right)} \tag{2.73}$$

Simplifying, we obtain that:

$$\langle \Delta A(t) \rangle = \frac{Z_0 \left(\langle A(t) \rangle_0 + \beta\lambda \langle A(t) B \rangle_0\right)}{Z_0 \left(1 + \beta\lambda \langle B \rangle_0\right)} \tag{2.74}$$

Since $\langle A(t)\rangle_0 = 0$, we retain only terms up to first order in ϵ and use the expansion $(1+\epsilon)^{-1} \approx 1-\epsilon$:

$$\langle \Delta A(t)\rangle = \beta\lambda\langle A(t)B(0)\rangle_0 \,(1 - \beta\lambda\langle B\rangle_0) \tag{2.75}$$

omit the term with λ^2:

$$\langle \Delta A(t)\rangle = \beta\lambda\langle A(t)\, B(0)\rangle \tag{2.76}$$

Consider a time-dependent external field $f(t)$ that couples to a mechanical property B:

$$\begin{aligned} \mathcal{H}(t) &= \mathcal{H}_0 - f(t)B \\ \langle \Delta A(t)\rangle &= \int_{-\infty}^{+\infty} dt'\, \chi_{AB}(t,t')\, f(t') \\ \langle \Delta A(t)\rangle &= \int_{-\infty}^{t} dt'\, \chi_{AB}(t-t')\, f(t') \end{aligned} \tag{2.77}$$

Let us return to the case of constant field in $t < 0$:

$$\begin{aligned} \langle \Delta A(t)\rangle &= \lambda \int_{-\infty}^{0} dt'\, \chi_{AB}(t,t') \\ \langle \Delta A(t)\rangle &= \lambda \int_{t}^{+\infty} d\tau\, \chi_{AB}(\tau) \end{aligned} \tag{2.78}$$

Finally, we obtain

$$\int_{t}^{+\infty} d\tau\, \chi_{AB}(\tau) = \beta\langle A(t)\, B(0)\rangle \tag{2.79}$$

or

$$\chi_{AB}(t) = \begin{cases} -\beta\langle \dot{A}(t)\, B(0)\rangle & t > 0 \\ 0 & t \leq 0 \end{cases} \tag{2.80}$$

As a concrete example, consider the mobility of particles in an external field.

$$\mathcal{H} = \mathcal{H}_0 - F_x x \tag{2.81}$$

A phenomenological expression for the steady-state particle velocity can be written as

$$\langle \nu_x(t)\rangle = \mu F_x. \tag{2.82}$$

If this relation is reformulated in terms of correlation functions, one obtains a microscopic expression for the mobility:

$$\begin{aligned} \langle \nu_x(t)\rangle &= F_x \int_{-\infty}^{t} dt'\, \chi_{\nu_x x}(t-t') \\ &= F_x \int_{0}^{+\infty} d\tau\, \chi_{\nu_x x}(\tau) \\ &= -\beta F_x \int_{0}^{+\infty} d\tau\, \langle x(0)\dot{\nu}_x(\tau)\rangle \\ &= \beta F_x \int_{0}^{+\infty} d\tau\, \langle \nu_x(0)\nu_x(\tau)\rangle \end{aligned} \tag{2.83}$$

Combining equations 2.82 and 2.83, we obtain:

$$\mu_x = \beta \int_{0}^{+\infty} d\tau\, \langle \nu_x(0)\nu_x(\tau)\rangle. \tag{2.84}$$

2.2.6 Two-Phase Thermodynamics

As noted above, the major challenge in statistical physics is the evaluation of the configurational integral. The problem becomes substantially simpler when the quantity of interest can be measured directly from a molecular-dynamics or Monte Carlo simulation. However, not all thermodynamic functions can be obtained straightforwardly from such modeling. In this work, we employed a method for computing the entropy of a liquid based on the velocity autocorrelation function (VACF), which can be extracted from a molecular-dynamics trajectory.[121–124] It can be written as:

$$C(t) = \langle \mathbf{v}(t) \cdot \mathbf{v}(0) \rangle \tag{2.85}$$

where $\mathbf{v}(t)$ and $\mathbf{v}(0)$ are the velocity vectors at times t and 0, respectively. Upon Fourier transformation, this function yields the vibrational density of states (VDOS):

$$F(\nu) = \int_{-\infty}^{+\infty} C(t)\ \exp^{-2\pi i \nu t}\, dt \tag{2.86}$$

Several choices of normalization are possible for both functions. For the present approach, it is essential to use the following normalization:

$$\int_{0}^{+\infty} 12F(\nu)\, d\nu = 3 \tag{2.87}$$

which effectively corresponds to the number of degrees of freedom, i.e., the number of possible translational motions in the system.

The key idea of the method is that the total VDOS can be decomposed into solid-like and gas-like contributions:

$$F(\nu) = (1 - f_g)\, F_s(\nu)\ +\ f_g F_g(\nu) \tag{2.88}$$

where f_g denotes the fraction of the gas-like component. Accordingly, the total entropy can be expressed as the sum of gas-like and solid-like contributions:

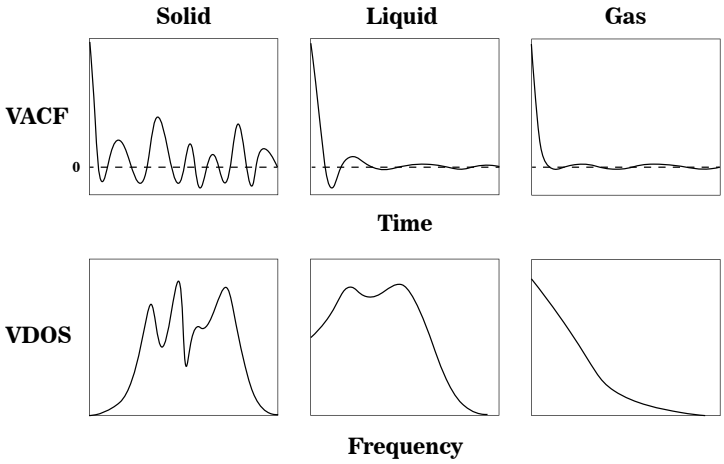

Figure 2.7: Schematic illustrations of the velocity autocorrelation function (VACF) and the corresponding vibrational density of states (VDOS) for the three states of matter: solid, liquid, and gas.

$$S_l = S_s + S_g \tag{2.89}$$

Figure 2.7 schematically illustrates the velocity autocorrelation function and the corresponding vibrational density of states for the three states of matter: solid, liquid, and gas.

To decompose the VDOS into gas-like and solid-like contributions, a hard-sphere model was introduced. In this notation, γ denotes the hard-sphere packing fraction of the gas-like component, and f_g^{HS} is the hard-sphere fluidity factor (i.e., the gas-like fraction). To determine these unknown parameters, one can introduce the generalized diffusivity:

$$\Delta = \frac{8}{3} F(0) \sqrt{\frac{\pi k T}{m}} \left(\frac{N}{\Omega}\right)^{1/3} \left(\frac{6}{\pi}\right)^{2/3} \tag{2.90}$$

Using Δ, the following equation for γ can be obtained[125]:

$$\frac{2(1-\gamma)^3}{2-\gamma} - \gamma^{2/5} \Delta^{3/5} = 0 \tag{2.91}$$

The gas-like fraction is then given by

$$f_g^{HS} = \gamma^{2/5} \Delta^{3/5} \tag{2.92}$$

The resulting frequency spectrum for the gas-like component in the hard sphere model has the Lorentzian form:

$$f_g^{\mathrm{HS}} F_g^{\mathrm{HS}}(\nu) = \frac{F(0)}{1 + \left(2\pi\nu F(0)/f_g^{\mathrm{HS}}\right)^2} \tag{2.93}$$

The gas-like contribution to the entropy can be written as

$$S_g = f_g^{\mathrm{HS}} N k_B \int_0^{+\infty} 12 F_g^{\mathrm{HS}}(\nu) W_g^{\mathrm{HS}}\, d\nu \tag{2.94}$$

with a weighting function that is also defined within the hard-sphere approximation:

$$W_g^{\mathrm{HS}} = \frac{1}{3}\left\{ \frac{S^{\mathrm{IG}}}{k} + \ln\left[\frac{1+\gamma+\gamma^2-\gamma^3}{(1-\gamma)^3}\right] + \frac{\gamma(3\gamma-4)}{(1-\gamma)^2} \right\} \tag{2.95}$$

Here, the ideal-gas component is expressed as

$$\frac{S^{IG}}{k} = \frac{5}{2} + \ln\left[\left(\frac{2\pi m k_B T}{h^2}\right)^{3/2} \frac{\Omega}{f_g^{HS} N}\right] \tag{2.96}$$

By normalizing the spectral component, this expression can be simplified to

$$S_g = 3 N k_B f_g^{HS} W_g^{HS}. \tag{2.97}$$

An analogous relation is used for the solid-like contribution:

$$S_s = N k_B \int_0^{+\infty} 12\left[F(\nu) - f_g F_g(\nu)\right]\, W_s\, d\nu \tag{2.98}$$

In this case, the weighting function is taken from the harmonic approximation.

$$W_s(\nu) = \frac{h\nu/k_B T}{\exp h\nu/k_B T - 1} - \ln\left[1 - \exp\left(-h\nu/k_B T\right)\right]. \tag{2.99}$$

3 Thermodynamic properties of iron and iron oxides

3.1 Introduction

A quantitative description of metal oxidation and reduction is not possible without thermodynamic data, which establish whether a given process is feasible in principle. At the same time, the full set of thermodynamic parameters defines the equation of state of the material. In this chapter, thermodynamic properties are computed using modern methods of condensed-matter physics. This is critical because the degree of agreement with experimental thermodynamic data largely determines the credibility of results obtained from first-principles simulations.

This chapter is based on:

- **Aleksandr Maliugin**, Dmitry I. Sharapa, and Felix Studt. Theoretical study on iron oxidation and reduction of iron oxide. In preparation, 2026.

3.2 Methodology

3.2.1 DFT calculations

All density functional theory (DFT) calculations were carried out with the Vienna *Ab initio* Simulation Package (VASP).[87,126,127] Core–valence electron interactions were described using the projector augmented-wave (PAW) method.[128] The exchange–correlation energy was treated within the generalized gradient approximation employing the Perdew–Burke–Ernzerhof functional[96]. Electronic wave functions were expanded in a plane-wave basis with a kinetic-energy cutoff of 450 eV. Self-consistent electronic minimization was converged to 10^{-6} eV, and structural relaxations were continued until residual forces were below 10^{-3} eV/Å.

On-site interactions of Fe d electrons were included via the DFT+U formalism,[106] using the Dudarev implementation[109] with $U_{\text{eff}} = 4$ eV. Brillouin-zone integrations employed the k-point meshes listed in Table 3.1. Diffusion transition states were determined with the nudged elastic band (NEB) method[129]. In addition, ground-state energies were recalculated using the HSE06 hybrid functional[130] to improve the accuracy of the thermodynamic quantities. Geometry optimization at the hybrid-functional level was performed until the total energy change fell below 10^{-3} eV.

Table 3.1: First-principles calculation parameters for iron and its oxides.

	Number of atoms	Space Group	Lattice parameters, Å	k-points grid	q-points grid
α-Fe	2	229	a = 8.741	11× 11 × 11	32× 32 × 32
α-Fe	54	229	a = 11.329	3 × 3 × 3	-
FeO	64	225	a = 8.783	2 × 2 × 2	22× 22 × 22
Fe_3O_4	56	227	a = 8.438	2 × 2 × 2	22× 22 × 22
Fe_2O_3	120	167	a = 10.103, c = 13.839	2 × 2 × 1	11× 11 × 11

3.2.2 Thermodynamic properties

Thermodynamic quantities were evaluated within the quasi-harmonic approximation[112]. For selected supercells, the Hessian (dynamical) matrices were computed using density functional perturbation theory (DFPT) as implemented in VASP.[131] Phonon dispersions, thermodynamic potentials, and the isothermal thermal expansion were obtained with the phonopy package.[132,133] The corresponding $\mathbf{q}$-point meshes used for the lattice-dynamical calculations are summarized in Table 3.1.

Within QHA, the phonon contribution to the Helmholtz free energy is given by

$$F_{\text{ph}}(T,V) = \frac{1}{2}\sum_{\mathbf{q}i}\hbar\omega_{\mathbf{q}i}(V) + k_B T \sum_{\mathbf{q}i}\ln\left[1-\exp\left(-\frac{\hbar\omega_{\mathbf{q}i}(V)}{k_B T}\right)\right], \tag{3.1}$$

where k_B is the Boltzmann constant and $\omega_{\mathbf{q}i}$ denotes the phonon frequency of mode i at wave vector $\mathbf{q}$. The phonon spectrum is assumed to be independent of the electronic temperature. The Gibbs free energy is obtained according to 2.63. Figure 3.1 illustrates a search of ΔG.

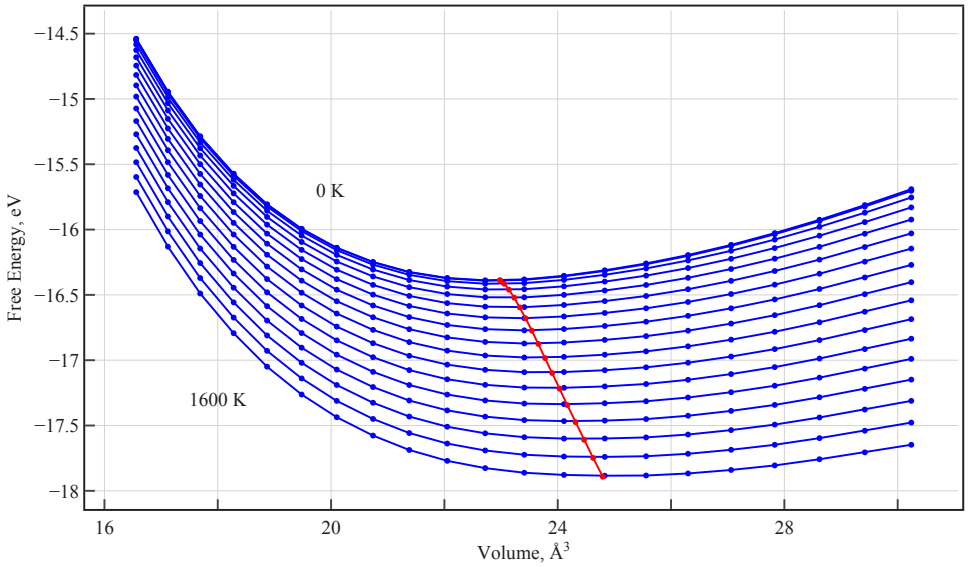

Figure 3.1: Calculation of the Gibbs free energy of bcc iron within the quasi-harmonic approximation (QHA). The blue lines represent the Helmholtz free energy over the temperature range from 0 to 1600 K in steps of 100 K, while the red line represents the Gibbs free energy obtained from the relation $p = -\left(\frac{dF}{dV}\right)_T$ where p is the pressure under consideration, F is the Helmholtz free energy, and V is the volume.

The magnetic contribution to heat capacity was included using the empirical Inden model.[134] In this formulation,

$$k_\beta = \frac{\ln(|\mu_m| + 1)}{\frac{518}{1125} + \frac{11692}{15975}\left(\frac{1}{p} - 1\right)}, \tag{3.2}$$

$$k_\alpha = \frac{474}{497}\left(\frac{1}{p} - 1\right) k_\beta, \tag{3.3}$$

$$C_{\text{mag}} = \begin{cases} k_\alpha R \ln\dfrac{1+\tau^3}{1-\tau^3}, & \tau < 1, \\ k_\alpha R \ln\dfrac{\tau^5+1}{\tau^5-1}, & \tau > 1, \end{cases} \tag{3.4}$$

where R is the gas constant, $|\mu_m|$ is the magnitude of the magnetic moment, $\tau = T/T_C$, and T_C is the Curie temperature. The structural factor p is defined as the ratio of the magnetic enthalpy in the paramagnetic state to the total magnetic enthalpy. For α-iron $p = 0.4$ is set, while for all other structures $p = 0.28$ is used.[135]

3.3 Results

Accurate evaluation of oxidation and reduction kinetics requires reliable data on phase equilibrium in the Fe–O system. To this end, the thermodynamic properties of iron and its oxides from first principles are computed. The results are compared with the experimental reference data reported under standard conditions (298 K, 1 atm).[136]

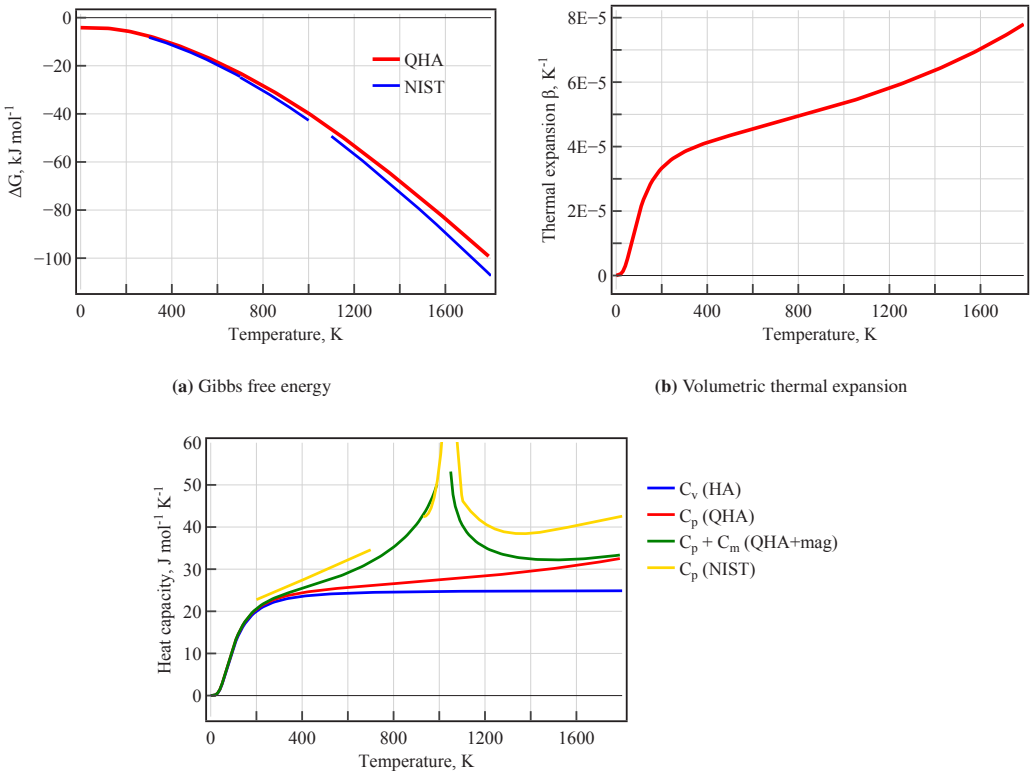

(a) Gibbs free energy

(b) Volumetric thermal expansion

(c) Heat capacity

Figure 3.2: Thermodynamic properties of bcc iron: heat capacity calculated within with harmonic approximation (HA), quasi-harmonic approximation (QHA), and QHA including magnetic heat capacity computed with Eq. 3.4. The Gibbs free energy and heat capacity are compared to the experimental data (NIST).[136]

Figure 3.2 summarizes the calculated thermodynamic properties of body-centred cubic (bcc) iron. For comparison, the heat capacity is decomposed into three contributions: the harmonic approximation, the quasi-harmonic approximation, and the magnetic term. It is evident that using only C_V obtained within the harmonic approximation is insufficient for a quantitatively correct description. Although this approximation captures the basic physical picture underlying

the Debye model, it predicts a temperature-independent heat capacity once the Debye temperature is reached.

Including thermal expansion within the quasi-harmonic approximation substantially improves the agreement. The corresponding temperature dependence of the volumetric thermal expansion coefficient is shown in Fig. 3.2c. However, the adopted lattice-dynamical treatment alone cannot adequately reproduce the ferromagnetic–paramagnetic transition at the Curie temperature. For this reason, an empirical model was introduced for the magnetic contribution. The model is parametrized by the Curie temperature, taken from experimental data, and by the atomic magnetic moment in the ferromagnetic (or antiferromagnetic) configuration, obtained from first-principles calculations and assumed to be constant over the entire temperature range. When all contributions are combined, the resulting Gibbs free energy is in good agreement with experimental data.

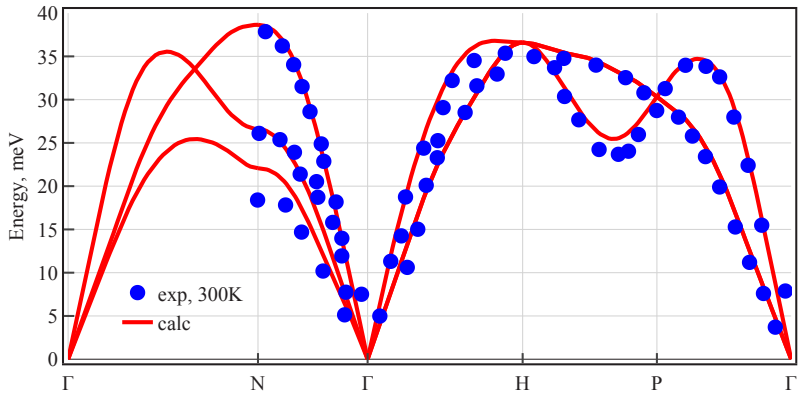

Figure 3.3: Calculated phonon band structure of bcc iron (red lines) compared to experimental data at 300 K (blue dots) [38]. For comparison, the computed data are presented for a volume corresponding to 300 K.

In order to ensure the correctness of the system's description, the phonon density of states was also calculated (Fig. 3.3). The obtained results are in good agreement with the experimental data. [38]

With increasing temperature, solids can also exhibit first-order phase transitions. Iron, for instance, undergoes a bcc→fcc transformation at 1185 K, re-enters a high-temperature bcc phase at 1667 K, and melts at 1811 K. [37] In the present workflow, the analysis is restricted to phases that are stable at $T = 0$ K; consequently, these finite-temperature phase transitions were not explicitly included.

Thermodynamic properties of iron oxides were evaluated in an analogous manner (Fig. 3.4, 3.5, 3.6). Overall, the calculated Gibbs energies reproduce the experimental trends with good accuracy. The remaining deviations are most likely related to the intrinsic difficulty of describing

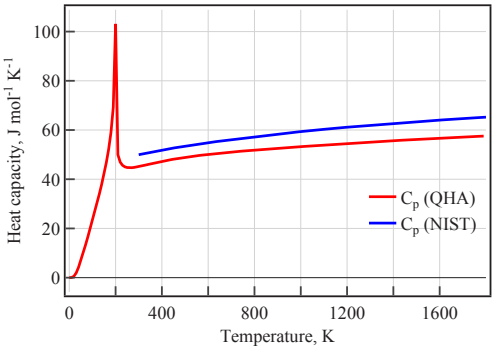

(a) Heat capacity

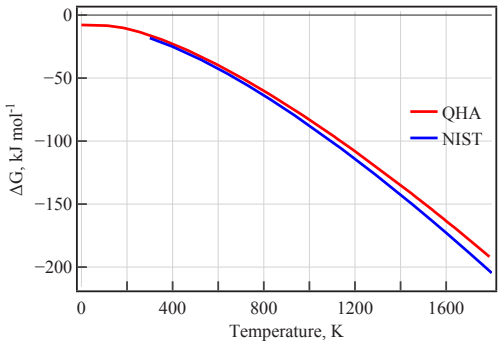

(b) Gibbs free energy

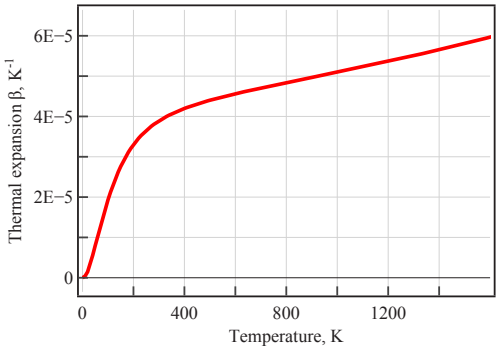

(c) Volumetric thermal expansion

Figure 3.4: Thermodynamic properties of FeO. The red lines denote calculated data. The blue lines correspond to experimental NIST data. [136]

magnetic thermodynamics within current first-principles frameworks. As discussed in Ref. [137], spin-polarized DFT typically captures ground-state magnetic properties well, yet it tends to substantially overestimate the Curie temperatures of ferromagnetic materials.

At the same time, it is evident that the deviation from the experimental data increases as the temperature approaches the melting point of each crystal. For most of the considered compounds, the calculated curves depart from the experimental reference with increasing temperature. Hematite (Fe_2O_3) is a notable exception; the underlying reason is related to its thermodynamic stability and will be discussed later.

Finally, an analysis of temperature-dependent formation enthalpies revealed a systematic underestimation, which effectively translates into an overestimation of the stability of oxide at the PBE+U level. To overcome this problem, optimized structures with PBE + U were further refined using

the hybrid functional HSE06 with a Hartree-Fock exchange of 18%. This additional refinement substantially improved agreement with the experimental formation energies and allowed us to construct a phase diagram that is qualitatively consistent with experimental observations.

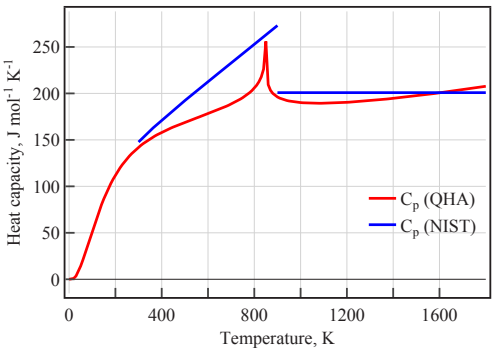

(a) Heat capacity

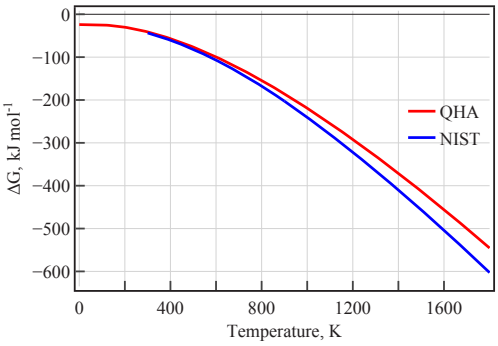

(b) Gibbs free energy

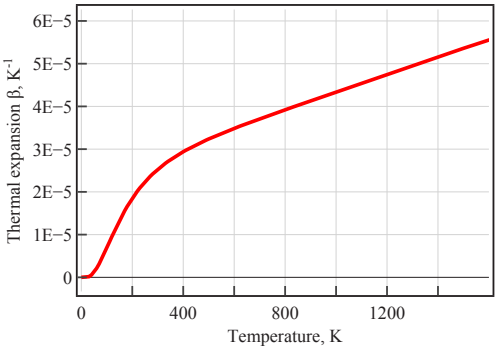

(c) Volumetric thermal expansion

Figure 3.5: Thermodynamic properties of Fe_3O_4. The red lines denote calculated data. The blue lines correspond to experimental NIST data.[136]

Using the assembled thermodynamic dataset, Gibbs free energy of formation diagrams are constructed and mapped the phase stability fields for oxidizing (Fig. 3.7a) and reducing (Fig. 3.7b) conditions. Both diagrams contain a temperature interval in which FeO is predicted to be unstable. In the present calculations, the upper limit of this interval is ∼425 K, i.e., roughly half of the experimentally reported value (858 K). Despite this quantitative mismatch, the computed diagrams reproduce the main qualitative features of the experimentally observed phase behaviour, supporting the overall robustness of the modelling approach. Notably, even if one relies on experimentally tabulated thermodynamic data for ideal crystals, the corresponding reaction reversibility temperature is still significantly underestimated (yielding about 500 K).

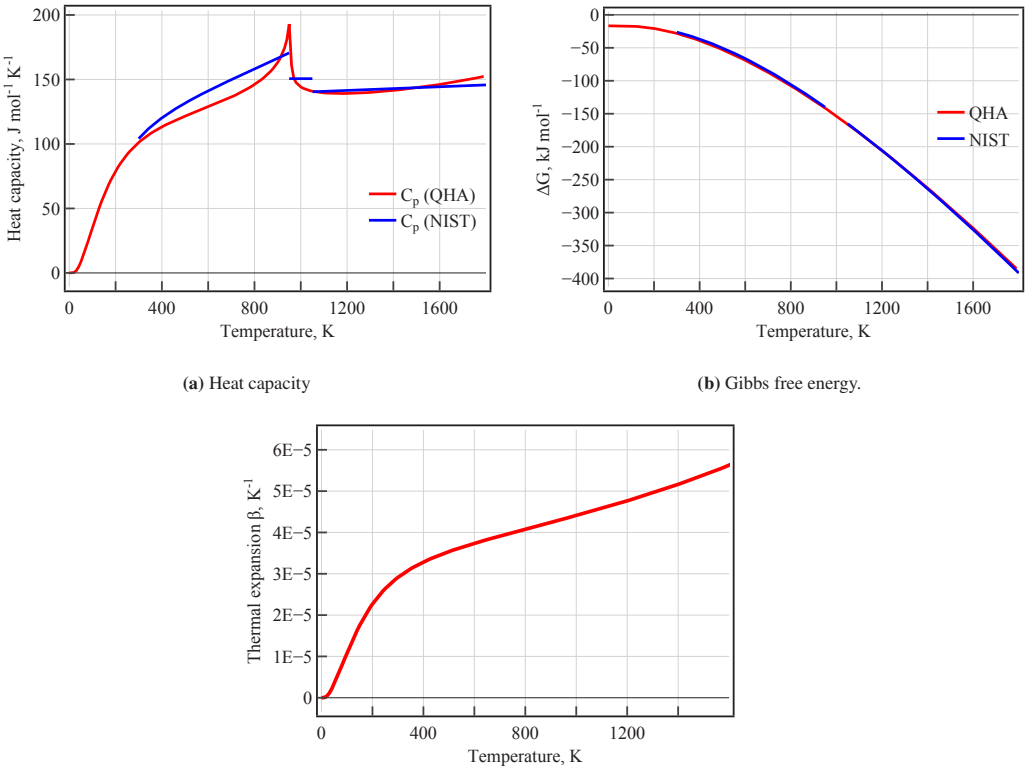

(a) Heat capacity

(b) Gibbs free energy.

(c) Volumetric thermal expansion

Figure 3.6: Thermodynamic properties of Fe_2O_3. The red lines denote calculated data. The blue lines correspond to experimental NIST data. [136]

In typical oxidation experiments, iron reacts in air, where the oxygen partial pressure can be treated as approximately constant. The diagram shows that under such conditions metallic iron is thermodynamically driven to oxidize over the entire temperature window considered. Below 425 K, the predicted instability of FeO leads to an oxide-layer sequence of Fe–Fe_3O_4–Fe_2O_3–O_2. Above this temperature, FeO becomes stable and oxidation follows the layered scheme Fe–FeO–Fe_3O_4–Fe_2O_3–O_2, while preserving the overall ordering of phases.

For reducing atmospheres, the stability domains of the condensed phases coincide with those obtained under oxidizing conditions. The reduction diagram further indicates that complete reduction of Fe_2O_3 to metallic iron requires a sufficiently large ratio $\tilde{p}(H_2)/\tilde{p}(H_2O)$, where $\tilde{p}(H_2)$ and $\tilde{p}(H_2O)$ are the partial pressures of hydrogen and water, respectively. The critical ratio decreases with increasing temperature, implying that reduction becomes thermodynamically more favourable at elevated temperatures.

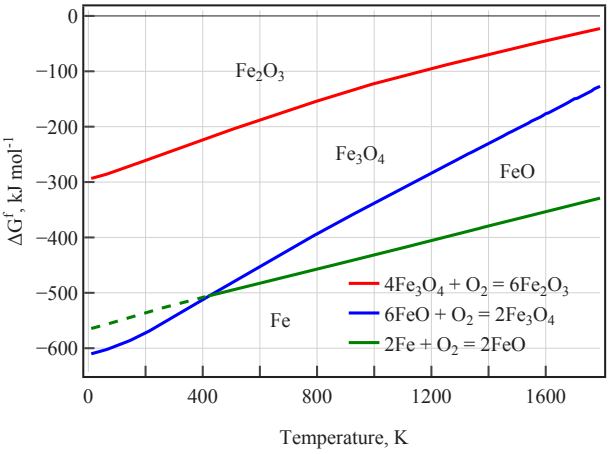

(a) Oxidizing conditions. The oxygen pressure is 1 atm.

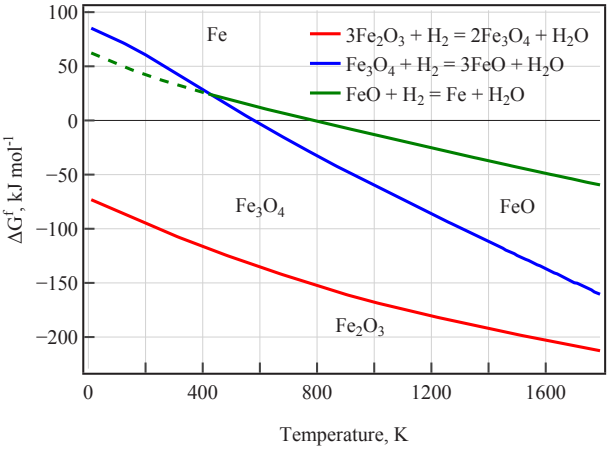

(b) Reducing conditions. The partial pressures of hydrogen and oxygen are equal.

Figure 3.7: Gibbs free energy of formation of iron and iron oxides at oxidizing 3.7a and reducing 3.7b conditions. The graph shows the stability regions of the crystals studied. The dotted line indicates the region where the disproportionation reaction $4\mathrm{FeO} = \mathrm{Fe_3O_4} + \mathrm{Fe}$ proceeds, meaning that any FeO formed decomposes into $\mathrm{Fe_3O_4}$ and Fe.

Several points should be clarified regarding the construction and interpretation of the phase diagram. First, the standard chemical potential μ_i^0 of each component (Fe or O) is referenced to its value at 298 K and 1 atm. Second, the analysis is restricted to iron oxide phases whose thermodynamic stability has been established experimentally and which are relevant for practical redox cycling. Accordingly, the phase sequence Fe–FeO–$\mathrm{Fe_3O_4}$–$\mathrm{Fe_2O_3}$–$\mathrm{O_2}$ is adopted and do not consider additional intermediate compositions.

Third, the imposed bounds for the oxygen chemical potential in iron and the iron chemical potential in oxygen are chosen for visualization only and do not carry independent physical meaning. They are introduced solely to display the stability fields and their intersections in a compact manner. For kinetic modelling of oxide-growth rate constants, only the chemical potentials at equilibrium phase boundaries are required, because these boundary values define the limiting chemical potentials that separate adjacent stability domains. As an example, the iron chemical potential at the FeO/Fe_3O_4 boundary can be written as

$$\Delta\mu_{\mathrm{Fe}} = 4\,\Delta\mu_{\mathrm{FeO}} - \Delta\mu_{\mathrm{Fe_3O_4}}, \tag{3.5}$$

where $\Delta\mu_{\mathrm{FeO}}$ and $\Delta\mu_{\mathrm{Fe_3O_4}}$ denote the chemical potentials of FeO and Fe_3O_4, respectively.

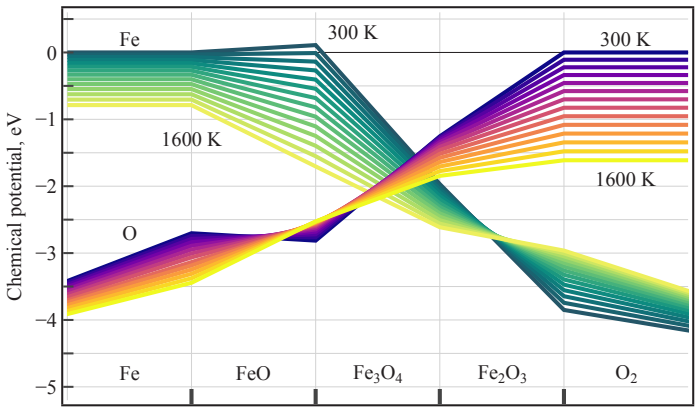

Figure 3.8: Phase diagram of the Fe-O system representing the oxidation process. The branch of lines shaded with a gradient from green to yellow corresponds to the chemical potential of iron at the respective temperatures, ranging from the lowest (300 K, green) to the highest (1600 K, yellow). The other branch represents the chemical potential of oxygen over the same temperature range (300 K – purple, 1600 K – yellow). The graph shows the ranges over which chemical potentials vary for specific phases, taking into account the interfaces between adjacent phases. The X-axis represents some spatial variable, such as the radius of a spherical particle.

Figure 3.8 presents the Fe–O phase diagram for $T = 300$–1600 K at $p = 1$ atm. Along the adopted phase sequence, the iron chemical potential is maximal in metallic Fe and decreases monotonically across the successive oxide phases, approaching a limiting value on the oxygen-rich side. An analogous monotonic behaviour is obtained for the oxygen chemical potential when moving toward the iron-rich side.

For oxidation, the ordering of iron and oxide layers is well established. In contrast, the reduction case motivates assessing which layer sequences are thermodynamically consistent with the phase-diagram constraints.

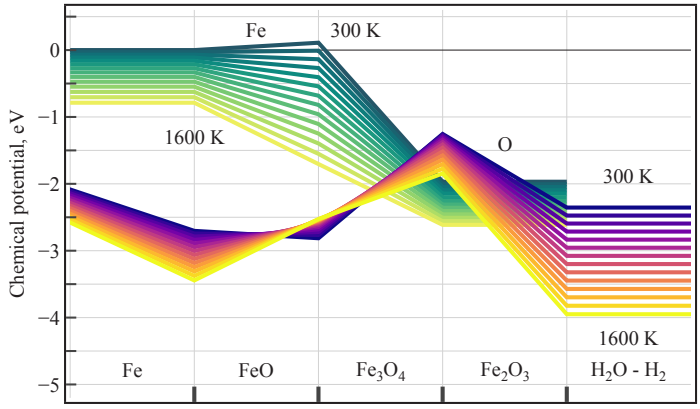

(a) Surface reduction of iron oxide

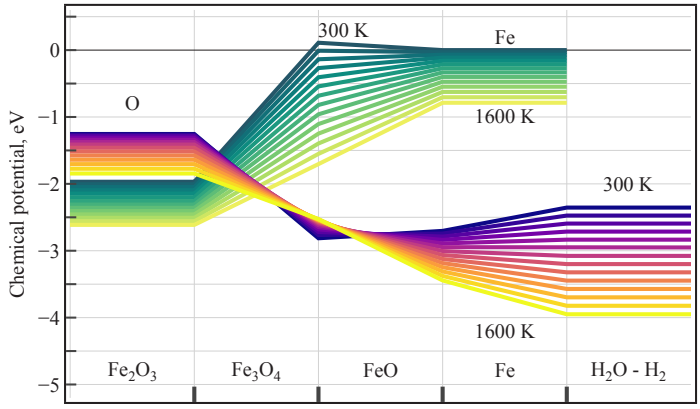

(b) Bulk reduction of iron oxide

Figure 3.9: Phase diagram of the Fe-O system representing the oxidation process. The branch of lines shaded with a gradient from green to yellow corresponds to the chemical potential of iron at the respective temperatures, ranging from the lowest (300 K, green) to the highest (1600 K, yellow). The other branch represents the chemical potential of oxygen over the same temperature range (300 K – purple, 1600 K – yellow). The graph shows the ranges over which chemical potentials vary for specific phases, taking into account the interfaces between adjacent phases. As an example, the data are shown for a partial-pressure ratio of water to hydrogen of 10^{-4}. The X-axis represents some spatial variable, such as the radius of a spherical particle.

If one assumes that reduction proceeds within the bulk, the reducing atmosphere would be in direct contact with hematite (Fe_2O_3) (Fig 3.9a). Under these conditions, the diagram suggests that magnetite (Fe_3O_4) would not be stable, and the transformation would follow the simplified

route $Fe_2O_3 \rightarrow FeO \rightarrow Fe$. This prediction, however, contradicts experimental observations, where intermediate oxide phases are typically detected.

A different picture emerges if metallic iron nucleates at the surface and a layered arrangement develops according to Fe_2O_3–Fe_3O_4–FeO–Fe–H_2O+H_2 (Fig 3.9b). In this case, the chemical-potential profile does not introduce additional extrema, and the reduction proceeds sequentially through the intermediate oxides. Finally, once iron forms at the surface of a hematite particle, it produces a dense metallic shell. Because iron is denser than hematite, complete conversion cannot fill the shell volume entirely with iron, implying that reduction is necessarily accompanied by pore formation and local mechanical damage, such as cracking.

The Appendix 11.1 presents diagrams with stability regions for oxidizing and reducing conditions depending on the temperature and partial pressures of the gas phase components.

3.4 Conclusions

In this chapter, the thermodynamic properties of iron and its oxides were calculated from first principles. The results are in good agreement with experimental data, which suggests that the predicted properties are sufficiently reliable for macroscopic modelling aimed at optimising technology design.

Based on the computed dataset, phase-equilibrium diagrams were constructed, providing a clear picture of the thermodynamic driving forces and phase stability across the relevant conditions. The results reproduce the stability region of FeO to an acceptable degree and predict a similar high-temperature behaviour for Fe_2O_3. In particular, some experimental studies indicate that hematite does not melt but instead decomposes, releasing O_2 and forming Fe_3O_4. This interpretation is also supported by the excellent agreement between the calculated and experimental thermodynamic functions for hematite.

In addition, phase-equilibrium diagrams were constructed in a form that explicitly represents the chemical-potential gradients across layered sequences of iron and its oxides, together with the ambient gas phase, which collectively constitute the reactive system. These diagrams clearly reveal phase transitions at specific temperatures. By analysing two possible diagrams under reducing conditions, it can be concluded that metallic iron is most likely to form at the surface of an oxide particle. This is supported by the monotonic behaviour of the chemical potential across the thickness of the solid layers. The resulting iron layer is expected, first, to hinder further reduction because oxygen bound in water must be removed from the system and, second, to be unable to form a fully dense phase in this geometry, as illustrated in Fig. 3.10. Consequently,

Figure 3.10: Schematic representation of the surface reduction process. The pink hexagons represent iron oxides, and the purple pentagons represent iron. It can be seen that the reduced iron is forced to form domains, as the overall particle size must decrease. For this reason, a fully formed particle with a sufficiently rapid reduction rate will always be porous.

the reduced iron product should be porous. Incomplete reduction may also lead to residual oxide inclusions.

These assumptions are supported by experimental observations.[25] It has been reported that both the oxidation product (iron-oxide particles) and the reduction product (iron particles) can exhibit widely varying porosities, depending on the mechanical properties of the precursor micrometre-sized particles from which they are formed, as well as on the reaction conditions and reactor design.

4 Diffusion phenomena in iron and iron oxides

4.1 Introduction

The study of metal oxidation and reduction is inherently a multistep problem, reflecting the wide range of phenomena that occur at the atomistic scale. These include molecular adsorption at the surface, dissociation reactions, penetration of species into the subsurface region, diffusion within the bulk phase, interfacial processes at phase boundaries, and related effects. Any of these elementary phenomena may become rate-limiting for the overall transformation. Because mass transport to the reactive zone (interface) is important in solid-state chemical reactions, this chapter focuses on the diffusion of iron and oxygen species within the bulk phase.

This chapter is based on:

- **Aleksandr Maliugin**, Dmitry I. Sharapa, and Felix Studt. Theoretical study on iron oxidation and reduction of iron oxide. In preparation, 2026.

4.2 Methodology

All density functional theory (DFT) calculations were performed using the Vienna *Ab initio* Simulation Package (VASP).[87,126,127] Core–valence electron interactions were treated within the projector augmented-wave (PAW) formalism[128]. Exchange–correlation effects were described using the Perdew–Burke–Ernzerhof (PBE) functional within the generalized gradient approximation (GGA)[96]. The electronic wave functions were expanded in a plane-wave basis with a kinetic-energy cutoff of 450 eV. Electronic self-consistency was achieved with an energy tolerance of 10^{-6} eV, and structural relaxations were continued until the residual forces fell below 10^{-3} eV/Å. Strong on-site interactions of Fe d states were incorporated via the DFT+U approach[106] in the Dudarev formulation,[109] using an effective parameter $U_{\mathrm{eff}} = 4$ eV. Transition states were located using the nudged elastic band (NEB) method.

Evaluating the self-diffusion coefficient requires an explicit analysis of the atomic migration pathways available in the crystal lattice. Because the temperatures of interest are sufficiently high for point-defect transport to dominate, the present study is rectricted to vacancy-mediated diffusion via neutral (Schottky-type) vacancies. The Gibbs free energy of vacancy formation was computed as

$$G^{f}_{\mathrm{vac},i}(T) = G_{\mathrm{def}}(T) - G_{\mathrm{bulk}}(T) - \mu_i(T), \tag{4.1}$$

where $G_{\mathrm{def}}(T)$ is the Gibbs free energy of the supercell containing a vacancy on a site of species i, $G_{\mathrm{bulk}}(T)$ is the Gibbs free energy of the corresponding defect-free bulk supercell, and $\mu_i(T)$ is the chemical potential of the removed species.

For each oxide, the equilibrium concentration of vacancies of type i was then estimated as a function of temperature using

$$C_{\mathrm{vac},i} = x_{\mathrm{vac}} \exp\left(-\frac{G^{f}_{\mathrm{vac},i}(T)}{k_B T}\right), \tag{4.2}$$

where x_{vac} is the fraction of vacancy sites in the simulation cell. It can be noted that, in several oxides, the vacancy fraction can become sufficiently large that the vacancy formation free energy is no longer constant but depends on composition. Capturing this effect would require sampling a broad set of vacancy configurations within the supercell, which is beyond the scope of the present work.

4.3 Results

4.3.1 Calculation of vacancy concentration

Accurate diffusion coefficients require thermodynamic information on vacancy populations, since vacancies define the dominant migration pathways for atoms in crystalline oxides. Figure 4.1a summarizes the calculated vacancy concentrations for the relevant sublattices in iron oxides. As widely reported, FeO exhibits an unusually high defect content and is frequently non-stoichiometric. The calculations reproduce this hallmark behavior: the predicted vacancy concentration of iron remains extremely large over most of the explored temperature and chemical-potential range. As discussed above, such a defect-rich regime would, in principle, require an explicit treatment of the composition dependence of defect formation energies. Because this was

not included here, the present results are effectively constrained by the fixed stoichiometry of the computational supercell.

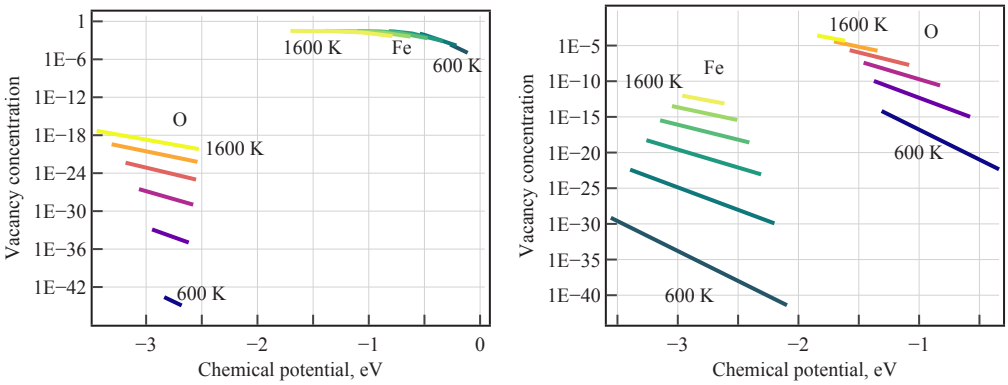

(a) FeO

(b) Fe_2O_3

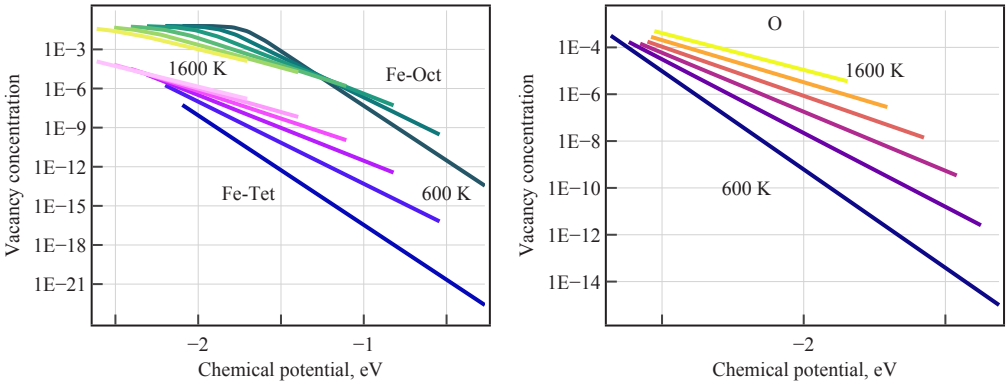

(c) Iron in Fe_3O_4

(d) Oxygen in Fe_3O_4

Figure 4.1: Vacancy concentration of oxygen and iron as a function of chemical potential. The branches of lines shaded with a gradient from green to yellow and from purple to yellow correspond to the vacancy concentration at the respective temperatures, ranging from the lowest (600 K, green or purple) to the highest (1600 K, yellow). $\mathrm{Fe-Tet}$ denotes iron atom at the tetrahedral site and $\mathrm{Fe-Oct}$ represents iron atom located at the octahedral sites. The chemical potentials correspond to the oxidizing conditions illustrated in Fig. 3.8. The partial pressure of oxygen is 1 atm.

In Fe_3O_4, iron occupies two distinct crystallographic environments, namely octahedral (Fe_{oct}) and tetrahedral (Fe_{tet}) sites. In the inverse-spinel structure, tetrahedral Fe is significantly more strongly stabilized than octahedral Fe, and this trend is confirmed by our calculations. Figure 4.1c therefore shows a substantially higher vacancy population on the octahedral Fe sublattice than on the tetrahedral one. It follows that migration is expected to be dominated by Fe_{oct} species, whereas

Fe_{tet} sites remain essentially fully occupied to minimize the total energy. Oxygen vacancies in Fe_3O_4 are predicted to be slightly less abundant than Fe_{oct} vacancies, although the gap between the two is considerably smaller than in FeO.

In hematite (Fe_2O_3), the situation is reversed: oxygen vacancies are markedly more prevalent than iron vacancies. Overall, the vacancy distribution across the oxides displays an inversion trend: the concentration of iron vacancies decreases along the sequence $FeO \rightarrow Fe_3O_4 \rightarrow Fe_2O_3$, while the concentration of oxygen vacancies increases. This is a notable result because the most oxygen-rich phase also exhibits the highest oxygen-vacancy population. In the context of oxidation, it implies that hematite in contact with an oxygen atmosphere will not become perfectly saturated; instead, it maintains a thermodynamically imposed vacancy concentration and can accommodate continued oxygen transport into deeper regions of the material.

4.3.2 KMC simulations of diffusion coefficients

Diffusion in solids is a rare-event process. Crystal-lattice sites can be regarded as deep potential wells; therefore, during the time evolution of a crystalline system, atoms spend most of their time localized near these minima, performing thermal vibrations. At the same time, a crystal may contain additional metastable positions that can also act as potential sites; these correspond to local minima of the potential-energy landscape. For an atom to migrate from one site to another, it must overcome an intervening potential-energy barrier. This barrier is often sufficiently large to control the probability of the corresponding event. As a consequence, direct observation of atomic hops in molecular-dynamics simulations would require an impractically large number of time steps, which is precisely why diffusion is referred to as a rare event. Such processes are therefore commonly simulated using kinetic Monte Carlo methods.

In this work, vacancy-mediated diffusion via a Schottky-type mechanism is considered. This choice is motivated by the relatively high temperature range of interest, because the equilibrium vacancy population increases with temperature and vacancies therefore become the dominant carriers of mass transport. An alternative pathway is interstitial (Frenkel-type) diffusion, in which atoms migrate through interstitial sites. It is commonly assumed that at lower temperatures the probability of occupying an interstitial position can be comparatively higher for certain species and materials.

At the same time, increasing temperature also leads to thermal expansion, which enlarges the available interstitial volume and may, in principle, facilitate interstitial accommodation. Nevertheless, the migration barrier along an interstitial pathway is largely governed by the local bonding topology and typically does not change dramatically with temperature. Within the scope of the

present study, The focus is on Schottky-type vacancy diffusion as the most relevant mechanism under high-temperature conditions.

The diffusion coefficient is evaluated using the Einstein relation, which provides a general framework for activated random-walk processes.

$$\mathrm{MSD} = \left\langle \, |r(t) - r(0)|^2 \right\rangle = \frac{1}{N} \sum_{i=1}^{N} |r_i(t) - r_i(0)|^2 = 6Dt. \tag{4.3}$$

Consider atomic motion on a cubic crystal lattice. Each individual hop has a fixed jump length; however, the net displacement is not equal to the simple sum of the elementary displacements. For instance, with a finite probability an atom may return to its initial position during the simulation, in which case the resulting displacement relative to the starting point becomes zero. Therefore, the diffusion coefficient must be defined in terms of the mean-squared displacement averaged over all possible trajectories, thereby capturing the statistics of the random walk. In some cases, it is sufficient to introduce a correlation factor that corrects for such back-and-forth correlations:

$$f = 1 + \lim_{n\to\infty} \frac{2}{n} \sum_{i=1}^{n-1} \sum_{j=1}^{n-i} \langle \cos\theta_{i,i+j} \rangle. \tag{4.4}$$

Moreover, the symmetry and structural complexity of a crystal can generate multiple distinct migration pathways, each characterized by its own activation barrier. For this reason, kinetic Monte Carlo (KMC) is adopted as a more general approach: displacements, and thus diffusion coefficients, are obtained directly from the simulated stochastic trajectories without the need to preselect a single dominant path.

In the KMC framework, each event is characterized directly by its rate. In this work, event rates were evaluated using the Vineyard approximation[138]:

$$k_{\mathrm{kMC}} = \frac{\prod_{i=1}^{3N-3} \nu_i^{\mathrm{IS}}}{\prod_{i=1}^{3N-4} \nu_i^{\mathrm{TS}}} \, \exp\left(-\frac{E_a}{k_B T}\right), \tag{4.5}$$

where E_a is the activation energy, ν_i^{IS} are the vibrational frequencies of the migrating atom in the initial state, and ν_i^{TS} are those in the transition state. The prefactor is also referred to as the attempt frequency:

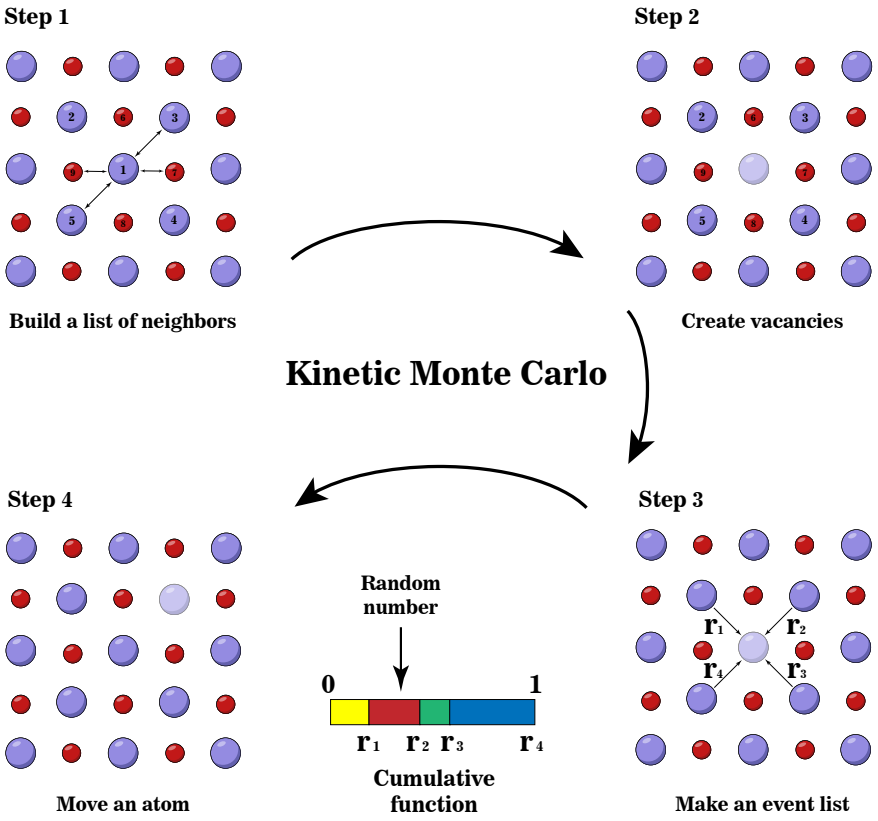

Figure 4.2: Algorithm of KMC code. In the first step, the initial geometry is generated and a nearest-neighbor list is constructed for each atom, thereby defining the set of possible migration pathways. In the second step, vacancies are distributed throughout the structure. Next, at the third step, a cumulative rate function is assembled and the event to be executed at the current step is selected stochastically. In the fourth step, the geometry is updated, after which steps 3 and 4 are repeated for a number of iterations equal to the prescribed number of KMC steps.

$$\nu_{att} = \frac{\prod_{i=1}^{3N-3} \nu_i^{\mathrm{IS}}}{\prod_{i=1}^{3N-4} \nu_i^{\mathrm{TS}}}. \tag{4.6}$$

which requires the corresponding attempt frequency. The attempt frequencies were obtained from constrained vibrational analysis within DFPT, considering only the migrating atom. Activation energies were computed using the nudged elastic band (NEB) method.

In this work, a kinetic Monte Carlo (KMC) algorithm was implemented in the C programming language. The overall workflow is schematically summarized in Fig. 4.2. The simulation is initialized by specifying the temperature, vacancy concentration, total number of KMC steps,

and the cutoff radius used to construct neighbor lists. Next, the atomic geometry is read from an input file, and a neighbor list is generated for each atom by including all sites within the cutoff distance. Distances to all neighbors are computed and used to assign an activation barrier and an attempt frequency to each possible jump. These kinetic parameters are provided as a separate pre-tabulated text file. For a prescribed vacancy concentration, vacancies are then placed randomly on the lattice sites of the crystal structure.

After initialization, the KMC simulation is launched. At each step, all possible atomic jumps from the current configuration are enumerated to form an event list. Each event is associated with a rate constant, and a cumulative probability distribution is constructed from the set of rates. A random number uniformly distributed in the interval $[0, 1]$ is then drawn, and the corresponding event is selected using the cumulative distribution. The atom involved in the selected event is displaced accordingly, and its squared displacement with respect to the initial geometry is updated. The procedure is then repeated for the next KMC step.

This procedure is repeated until the prescribed number of KMC steps is reached. The simulation output is then used to compute the diffusion coefficient along with its associated mean-square deviation (statistical uncertainty).

4.3.3 Diffusion coefficient

KMC simulations of transport in solid iron oxides require an explicit characterization of the underlying crystal structures in order to enumerate feasible atomic hopping pathways and to parameterize each hop by an activation barrier E_a and an attempt frequency ν_{att}. In this work, candidate jumps were restricted to a maximum hopping distance of 4 Å, since pathways involving longer displacements were found to possess prohibitively large barriers and thus contribute negligibly to diffusion. To keep the vibrational analysis tractable, the attempt frequency was estimated by considering only the migrating atom at the initial and transition states. The resulting migration barriers, attempt frequencies, and qualitative pathway assignments for all studied oxides are compiled in Table 4.1.

In FeO, iron and oxygen occupy crystallographically equivalent lattice sites (Wyckoff position 4a). Consequently, both species share the same geometric migration topology, with the saddle-point configuration associated with the 24d site, and a hop length of 3.10 Å. Despite this structural equivalence, the corresponding activation barriers differ markedly: 0.98 eV for iron versus 2.23 eV for oxygen. This substantial contrast supports the notion that, in wüstite, mass transport relevant to oxidation is dominated by iron migration.

Table 4.1: Input data for the KMC simulations calculated within PBE+U approach.

Oxide	Migrational pathway	Distance, Å	Attempt frequency, ν^{att}, $10^{12} s^{-1}$	Activation barrier E_a, eV
FeO	Fe - Fe	3.10	4.42	0.98
	O - O	3.10	5.74	2.23
Fe_3O_4	Fe_{oct} - Fe_{oct}	2.98	4.06	0.73
	Fe_{oct} - Fe_{tet}	3.48	5.53	2.07
	Fe_{tet} - Fe_{oct}	3.48	6.28	0.95
	Fe_{tet} - Fe_{tet}	3.65	11.80	0.75
	O - O	2.98	9.34	1.32
	O - O	3.12	13.61	1.46
	O - O	2.89	8.72	1.89
Fe_2O_3	Fe - Fe	2.93	2.81	1.89
	Fe - Fe	3.00	3.42	2.07
	Fe - Fe	3.40	3.12	2.23
	Fe - Fe	3.74	3.90	2.80
	O - O	2.69	8.54	0.67
	O - O	3.06	9.42	1.92
	O - O	2.92	8.59	1.51
	O - O	2.80	9.86	1.24

Figure 4.3 compares experimental iron diffusion coefficients with values obtained from the KMC simulations. The results capture the expected linear scaling of the diffusion coefficient with vacancy concentration in iron oxides. Moreover, for a given oxide, the simulated temperature dependence is in reasonable agreement with the experimental trends.

In the inverse-spinel lattice, iron occupies two crystallographically distinct sublattices, namely octahedrally coordinated and tetrahedrally coordinated sites. A specific complication of Fe migration in Fe_3O_4 is the occurrence of intermediate metastable positions that form additional local minima on the potential-energy surface. As illustrated schematically in Appendix 11.2, a successful migration event proceeds via a two-step sequence: an atom first hops from its regular lattice site to an intermediate site and only then reaches the final site. If, instead, the atom returns to the initial position, the net displacement associated with that sequence is zero and it does not contribute to the mean-squared displacement and, hence, to the diffusion coefficient. To treat this mechanism in a tractable manner, quasi-stationary approximation is employed in which the effective rate of long-range migration is taken as one half of the total rate of transitions from the regular site to the intermediate site.

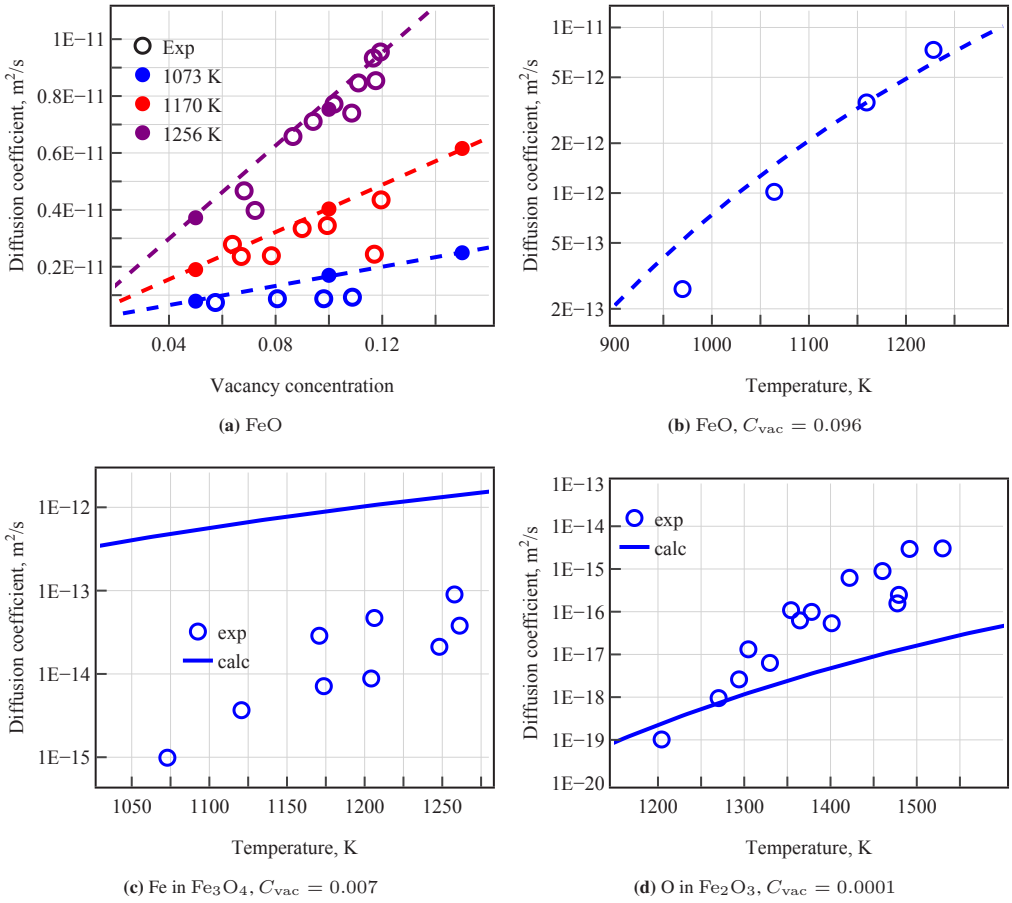

(a) FeO

(b) FeO, $C_{\mathrm{vac}} = 0.096$

(c) Fe in Fe_3O_4, $C_{\mathrm{vac}} = 0.007$

(d) O in Fe_2O_3, $C_{\mathrm{vac}} = 0.0001$

Figure 4.3: Comparison of the calculated iron diffusion coefficients with experimental data (open circles).[139] The figure shows the calculated iron diffusion coefficients as a function of vacancy concentration in FeO at constant temperatures and as a function of temperature for FeO, Fe_3O_4, and Fe_2O_3 at constant vacancy concentrations.

Comparison of the computed iron diffusion coefficients with experimental measurements indicates that the present model systematically overestimates iron mobility in Fe_3O_4 (Fig. 4.4b. A likely source of this deviation is an inaccurate description of the relevant migration barriers at the PBE+U level.

Although oxygen atoms in Fe_3O_4 occupy symmetry-equivalent lattice sites, the geometry of the Fe sublattice gives rise to three distinct oxygen-hopping pathways that differ only by their jump lengths. Each pathway is associated with its own activation barrier and attempt frequency.

Table 4.2: Results of the KMC simulations. The calculated values of diffusion coefficients were fitted using the Arrhenius equation, and the corresponding parameters are listed in the table.

Oxide	Species	A, 10^{-7} m^2 s^{-1}	E_a^{eff}, eV
FeO	Fe	6.56	0.98
	O	9.79	2.18
Fe_3O_4	Fe	1.03	0.68
	O	8.12	1.35
Fe_2O_3	Fe	4.48	2.21
	O	9.62	1.24

Overall, the resulting oxygen diffusion coefficient is moderately lower than the corresponding iron diffusion coefficient.

In hematite (Fe_2O_3), both iron and oxygen reside on crystallographically distinct sublattices; however, lattice symmetry generates four inequivalent migration pathways for iron and four for oxygen. As in magnetite, each pathway is characterized by a specific set of kinetic parameters. The systematic trend observed across the Fe–O solids persists: the iron migration rate decreases along the sequence $FeO \rightarrow Fe_3O_4 \rightarrow Fe_2O_3$, whereas oxygen migration becomes progressively faster.

Finally, the KMC results were fitted to an Arrhenius form, and the corresponding parameters are reported in Table 4.2. In most cases, the effective activation energy extracted from the fit is close to the smallest barrier among the set of inequivalent migration pathways identified in the structure.

4.3.4 Oxidation rate constants

According to Wagner's theory of oxidation[140], the rational rate constant of scale formation can be expressed as follows:

$$k_r = |z_{\text{O}}|\, c_{\text{O}} \int_{a'_{\text{O}}}^{a''_{\text{O}}} \left(\frac{z_{\text{Fe}}}{|z_{\text{O}}|}\, D_{\text{Fe}} + D_{\text{O}} \right) d\, \ln a_O = |z_{\text{Fe}}|\, c_{\text{Fe}} \int_{a''_{\text{Fe}}}^{a'_{\text{Fe}}} \left(D_{\text{Fe}} + \frac{|z_{\text{O}}|}{z_{\text{Fe}}}\, D_{\text{O}} \right) d\, \ln a_{\text{Fe}} \tag{4.7}$$

where D_{Fe} and D_{O} represent the diffusion coefficients of iron and oxygen, z_i denotes their chemical valences, c_i is the concentration of species i and a_i'' and a_i' correspond to the upper and lower limits of the thermodynamic activity of the component at the phase boundaries.

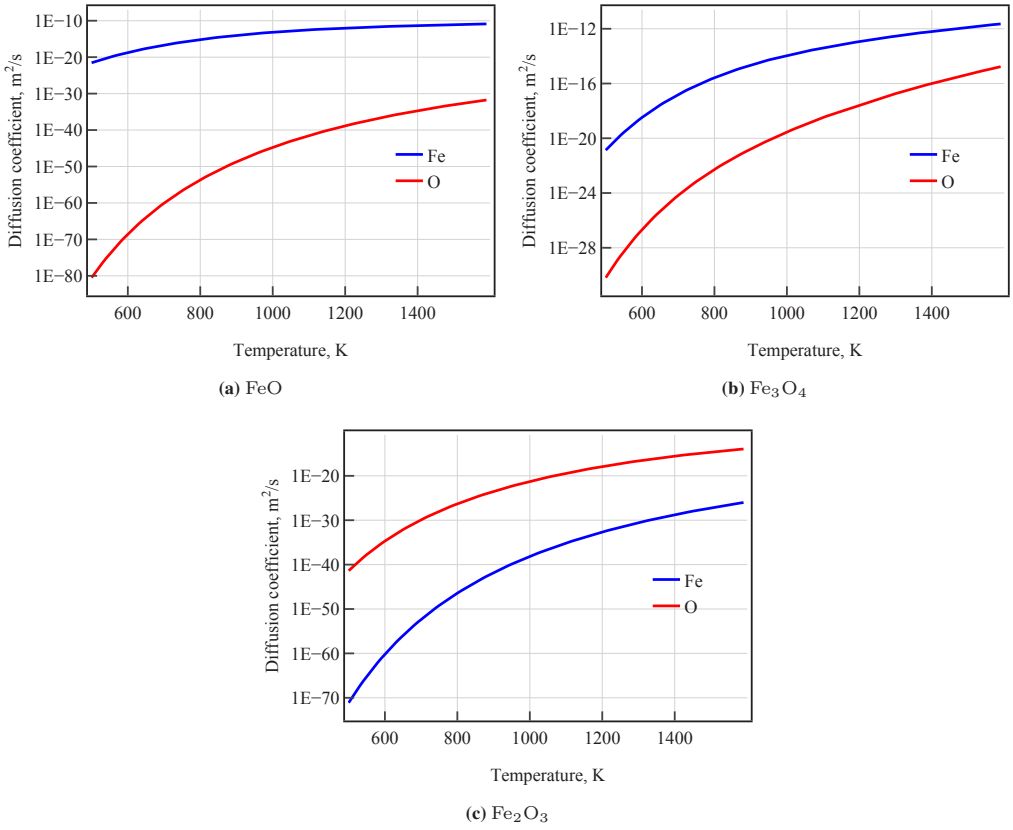

Figure 4.4: Temperature dependence of the diffusion coefficients. The calculations account for the vacancy concentration evaluated at the mean chemical potential of the corresponding species in the oxide.

From the computed thermodynamic and kinetic inputs, the rate constants for oxide growth are evaluated. For benchmarking, a reference set of rate constants is also constructed following the same workflow but using experimental thermodynamic and transport data. The comparison is presented in Fig. 4.5. A key outcome is that the first-principles-based model correctly singles out the slowest-forming oxide. At the same time, the reference constants were obtained using iron self-diffusion data only and rely on additional simplifying assumptions. This comparison suggests that oxygen transport may be somewhat underestimated in the theoretical description, with the most likely source of error being the predicted vacancy concentrations. Overall, coupling Wagner's oxidation theory with first-principles calculations offers a robust framework for rationalizing metal-oxide growth and for estimating oxidation and reduction rates.

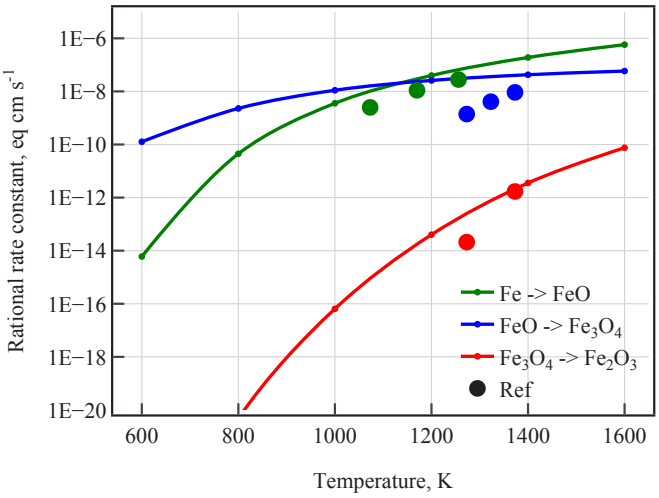

Figure 4.5: Rational rate constants for iron-oxide formation as a function of temperature computed with Wagner's theory. The results are compared with the reference data. [139]

4.4 Conclusions

In this chapter, diffusion coefficients of iron and oxygen species in iron and its oxides were determined. The calculations combine (i) thermodynamic predictions of equilibrium vacancy concentrations as functions of temperature and chemical potential and (ii) a systematic analysis of migration pathways within each oxide phase. The final diffusion coefficients were obtained using a kinetic Monte Carlo (KMC) scheme; the corresponding simulation code was developed as part of this work.

The resulting dataset provides a basis for proposing atomistic mechanisms of oxidation and reduction. Figure 4.6 summarises the oxidation mechanism. On the Fe_2O_3 surface, oxygen molecules adsorb and dissociate. Because hematite contains a comparatively large concentration of oxygen vacancies and oxygen exhibits high mobility in this phase, oxygen can diffuse into the bulk toward the Fe_3O_4/Fe_2O_3 interface. In contrast, both FeO and Fe_3O_4 are characterised by a substantially higher concentration of iron vacancies than oxygen vacancies, and iron is found to migrate much faster in these oxides. Consequently, iron atoms migrate from the Fe/FeO interface toward the FeO/Fe_3O_4 boundary and further toward the Fe_3O_4/Fe_2O_3 interface, thereby supplying iron for the growth of Fe_2O_3.

The reduction mechanism is illustrated in the figure 4.7. As discussed above, iron is the more mobile species in FeO and Fe_3O_4. Therefore, during reduction, iron diffuses from the outer metallic Fe phase inward toward Fe_2O_3, reducing Fe_2O_3 to Fe_3O_4 and Fe_3O_4 to FeO. Simultaneously,

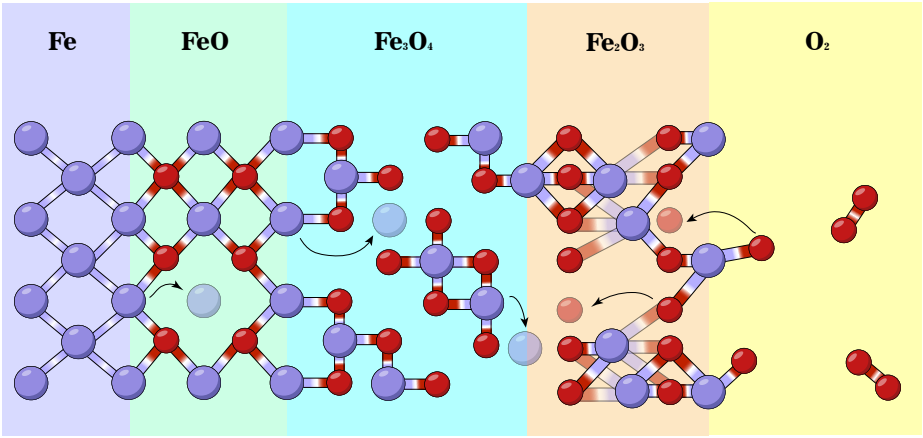

Figure 4.6: Mechanism of oxidation reaction. Oxygen adsorbs on the Fe_2O_3 surface, after which the molecule dissociates, and atomic oxygen migrates into the bulk via oxygen vacancies. In contrast, in bcc iron, the chemical potential of iron is higher, which drives a flux of iron atoms. These atoms migrate through the FeO and Fe_3O_4 layers via iron vacancies toward the Fe_3O_4/Fe_2O_3 interface, where oxidation proceeds.

oxygen migrates toward the Fe/gas interface, where it is removed from the solid by forming water. As oxygen is depleted near the Fe/FeO boundary, the metallic iron phase is correspondingly replenished in that region.

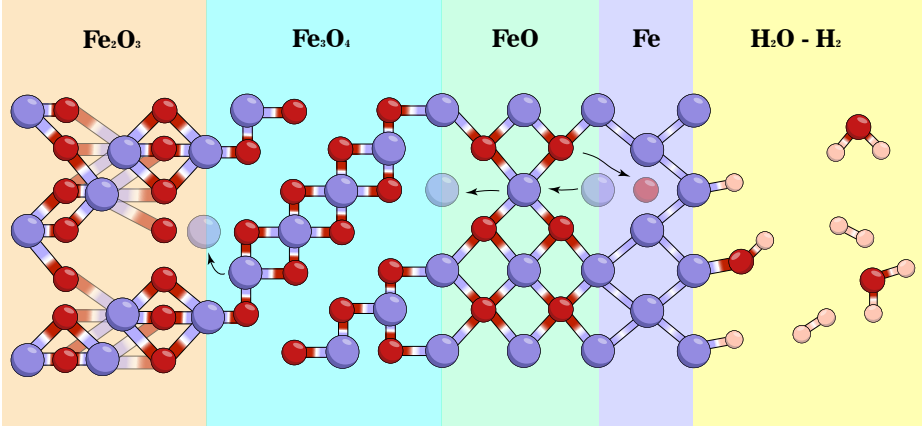

Figure 4.7: Mechanism of surface reduction reaction. Molecular hydrogen adsorbs on the bcc iron surface and subsequently dissociates. The high chemical potential of iron in the bcc phase induces a flux toward Fe_2O_3, causing iron atoms to migrate inward toward the Fe_3O_4/Fe_2O_3 boundary and thereby reduce Fe_2O_3 to Fe_3O_4. At the same time, iron migration within FeO releases oxygen, which diffuses from the oxide toward the gas phase, again driven by chemical-potential gradients. At the Fe/gas interface, water molecules form and then desorb into the gas phase.

5 Diffusion and adsorption of hydrogen and oxygen on iron

5.1 Introduction

One plausible pathway for oxidation and reduction involves the penetration of gaseous reactants through iron and their transport into the interior of the material. This route intrinsically couples interfacial phenomena at the iron surface with processes occurring in the subsurface and bulk regions. In this chapter, therefore the adsorption and diffusion of atomic oxygen and hydrogen are investigated, with the aim of clarifying how surface uptake, transport into the solid, and local chemical reactions collectively govern the overall redox kinetics.

5.2 Methodology

Spin-polarized *ab initio* calculations were carried out with the Vienna *Ab initio* Simulation Package.[127] Within VASP, density functional theory is formulated using a plane-wave basis in combination with either pseudopotentials or the projector augmented-wave method.[88,128] The exchange–correlation energy was treated within the generalized-gradient approximation using the PBE functional.[96] Dispersion interactions were accounted for by the Grimme D3 scheme.[141] Pseudopotentials with the following valence configurations were employed: Fe ($3d^7 4s^1$), O ($2s^2 2p^4$), and H ($1s^1$).

A plane-wave kinetic-energy cutoff of 500 eV was used throughout. Reciprocal-space integration relied on Monkhorst–Pack k-point meshes of $11 \times 11 \times 11$ for bulk iron and $6 \times 4 \times 1$ for the $2 \times 2 \times 1$ supercell slab of the Fe(110) surface. Slabs were separated by a 15 Å vacuum layer to minimize spurious interactions between periodic replicas. With these numerical parameters, hydrogen adsorption energies on iron were converged to within 0.05 eV, which is sufficient for the aims of the present study. The electronic self-consistency threshold was set to 10^{-6} eV, and structural relaxations were terminated when residual forces fell below 10^{-2} eV/Å. Transition states were determined using the Improved Dimer Method.[142]

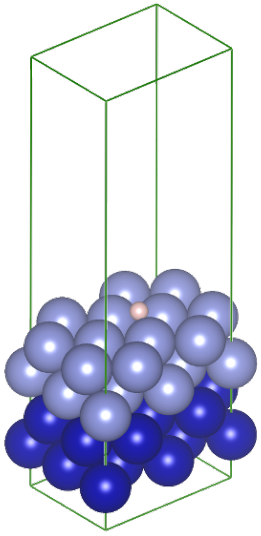

Figure 5.1: The slab of the 110 iron surface with an adsorbed hydrogen atom. Atoms frozen from relaxation are colored blue.

5.3 Results

5.3.1 Adsorption onto (110) iron surface

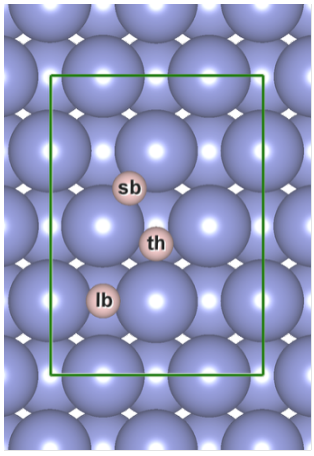

Figure 5.2: Adsorption sites on (110) surface of bcc iron: th – three-fold hollow, sb – short bridge, lb - long bridge.

In the redox chemistry of iron, surface adsorption plays a central role: oxidation is initiated by the uptake of oxygen, whereas reduction proceeds via hydrogen adsorption and subsequent surface reactions. In this work, the focus is on the Fe(110) surface (Fig.5.2), which is commonly identified as the most stable facet, i.e., the one with the lowest surface energy (0.153 eV/Å^2). The slab model comprises four atomic layers of iron, with the two bottom layers kept fixed to mimic the bulk constraint, while the remaining layers and all adsorbates were fully relaxed.

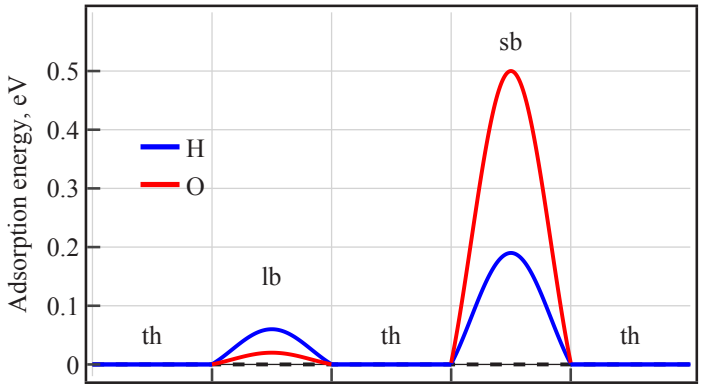

Figure 5.3: The adsorption energy profiles for hydrogen and oxygen on (110) surface of bcc iron: th (three fold hollow) – lb (long bridge) – th – sh (short bridge) – th.

The adsorption and surface migration of atomic H and O on the three most stable adsorption motifs reported for Fe(110) were investigated: the three-fold hollow site (th), the long-bridge (lb) and the short-bridge (sb). The computed adsorption energies indicate that, among these candidates, the th site is the only thermodynamically stable minimum for both species, with adsorption energies of -3.05 eV for hydrogen and -3.45 eV for oxygen. The corresponding reaction diagram further shows that lateral diffusion on the surface is facile: migration proceeds readily via the lb configuration, whereas pathways involving the sb site are comparatively hindered, as reflected by higher activation barriers (Fig.5.2). These trends imply that, under the conditions considered, surface transport is unlikely to be rate-limiting except in local environments where the diffusion path is constrained to traverse sb-type geometries.

5.3.2 Diffusion in iron

Once an atom is adsorbed, it can subsequently migrate into the crystal and diffuse through the lattice. This behaviour reflects the finite solubility of both hydrogen and oxygen in iron. From the perspective of oxidation and reduction kinetics, the key question is how rapidly these species

migrate in the solid because their diffusion coefficients directly affect the overall reaction rates and the spatial distribution of the reduced/oxidized regions.

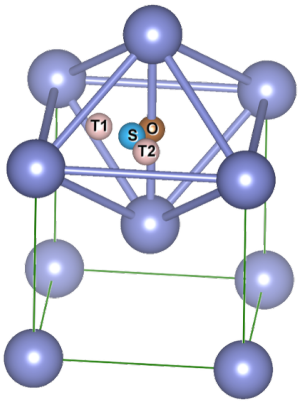

Figure 5.4: The diffusion sites of hydrogen and oxygen in bcc iron: O – octahedral, T1 and T2 – tetrahedral, S – saddle point.

It is known that the potential energy surface that govern bulk diffusion are not expected to be uniform for different types of atoms. In practice, the mass, effective size, and bonding characteristics of an interstitial atom—ultimately controlled by its electronic structure—lead to distinct stable sites and transition states (critical points) in the potential-energy surface. In the present case, hydrogen exhibits a global minimum in the tetrahedral interstitial site (Fig.5.4). Its diffusion proceeds through a saddle point with an activation barrier of 0.09 eV(Fig.5.5).

In contrast, oxygen shows a different site preference. The lowest-energy configuration corresponds to the octahedral interstitial site, accompanied by a local distortion of the surrounding Fe environment. Oxygen migration is governed by the tetrahedral site, which serves as the transition state along the dominant diffusion pathway. Thus, the tetrahedral site is a stable minimum for hydrogen but a transition-state configuration for oxygen. This geometric relation also implies a higher multiplicity of stable hydrogen positions: for each stable octahedral site available to oxygen, there are four symmetry-related tetrahedral sites that can host hydrogen as stable interstitial sites.

5.3.3 Generalized coordination number

Another curious way for iron oxide reduction is electrochemical reduction in ionic liquids, where metallic iron is reconstructed from solution. To describe this process using first-principles

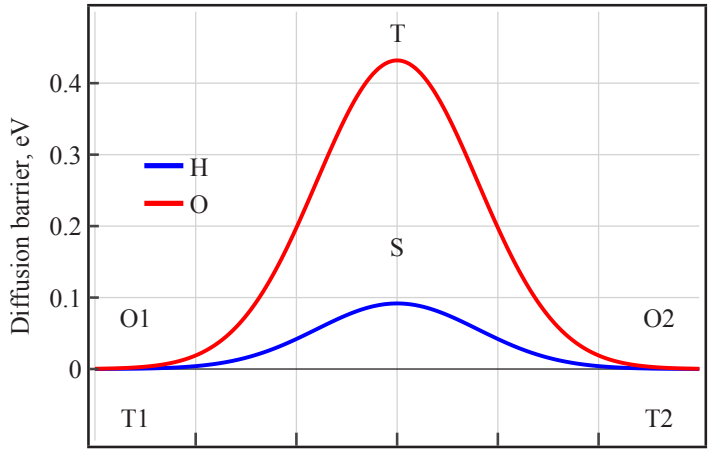

Figure 5.5: The diffusion energy profile for hydrogen (blue): tetrahedral site (T1) – saddle point (S) – tetrahedral site (T2); and oxygen (red): octahedral site (O1) – tetrahedral site (T) – octahedral site (O2).

approaches, it is necessary to quantify how the atom-wise energy of an iron depends on its local environment.

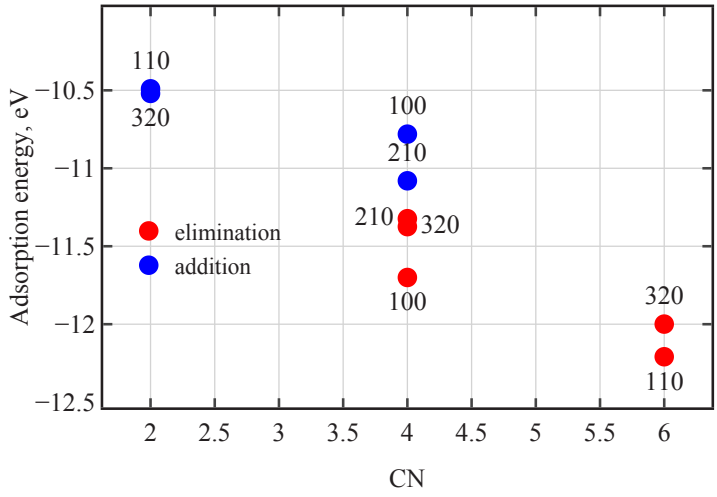

Figure 5.6: Dependence of the adsorption energy of an iron atom on the coordination number. For each data point, the crystallographic plane from which an atom was eliminated (red) or to which an atom was added (blue) is indicated. The reference state was defined as a hexaquairon(II) ion ($Fe^{2+}(H_2O)$), together with the intact slab and water molecules.

In this work, bcc-iron slabs were constructed that exposed several crystallographic planes. For each surface, a single Fe atom was either removed or added, and the resulting change in the total

energy was evaluated. The reference state was defined as a hexaquairon(II) ion ($Fe^{2+}(H_2O)$), together with the intact slab and water molecules. Then the dependence of the atom-resolved energy change on the coordination number (CN) and on the generalized coordination number (GCN), defined according to the following[143], was analysed:

$$\mathrm{CN} = \sum_{i=1}^{N} \mathrm{CN_{max,i}} \,/\, \mathrm{CN_{max}}$$

$$\mathrm{GCN} = \sum_{i=1}^{N} \mathrm{CN_{i}} \,/\, \mathrm{CN_{max}}$$

respectively, where i is a neighbour and N is a total number of atoms.

We find that the energy trends expressed as a function of CN cannot be reliably interpolated. In particular, the data exhibit substantial scatter for CN$= 4$ (Fig.5.6). By contrast, the energy plotted against GCN follows a clear monotonic relationship. This result indicates that GCN provides a substantially more faithful descriptor of the atomic environment in a monometallic system(Fig.5.7).

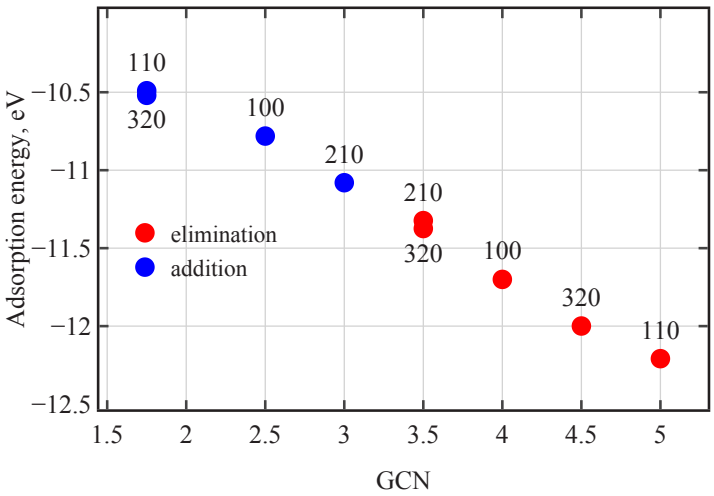

Figure 5.7: Dependence of the adsorption energy of an iron atom on the generalized coordination number. For each data point, the crystallographic plane from which an atom was eliminated (red) or to which an atom was added (blue) is indicated. The reference state was defined as a hexaquairon(II) ion ($Fe^{2+}(H_2O)$), together with the intact slab and water molecules.

5.4 Conclusions

In this chapter, the adsorption of atomic oxygen and hydrogen on the bcc Fe(110) surface was investigated. The calculated adsorption energies indicate that adsorption is thermodynamically favourable, and the corresponding migration barriers suggest that surface diffusion is expected to be fast.

The diffusion in bulk bcc iron was also analysed. The stable interstitial sites (local minima of the potential-energy surface) for both hydrogen and oxygen were identified, and the computed barriers imply very high migration rates within the iron lattice. These findings suggest that iron is sufficiently permeable to both hydrogen and oxygen atoms; therefore, an iron layer is not expected to constitute a kinetic bottleneck for the redox processes considered here.

In addition, a first-principle description of electrochemical reduction of iron oxide from a solvent environment was explored. It was found that the atom-resolved energetic trends for iron are captured much more reliably by the generalized coordination number than by the conventional coordination number.

6 Reduction of hematite using hydrogen

6.1 Introduction

The reduction of Fe_2O_3 is a key step in the energy cycle of iron-based energy carrier technologies. The overall efficiency of this step largely determines the industrial feasibility of implementing the concept at scale. Incomplete reduction increases the mass of the energy carrier and, consequently, lowers its effective energy density. In addition, particle size changes during cycling can introduce substantial operational challenges. Since the process is often conducted in a gas-flow reactor, particle shrinkage may, at minimum, alter the prevailing mass-transfer regime, and in the worst case, lead to entrainment and loss of the solid energy carrier from the system. Achieving deep and complete reduction of hematite—the oxidation product of iron—is therefore essential to ensure true process cyclicity. For this reason, a mechanistic understanding of hematite reduction is required to identify and mitigate the origins of inefficiencies during practical operation.

In this chapter, we employ modern first-principles and atomistic simulation methods to predict thermodynamic and kinetic properties relevant to the reduction of Fe_2O_3. These methods enable a consistent description of the underlying reduction pathways and provide quantitative insight into the factors that govern the extent and rate of reduction under operating conditions.

The chapter based on:

- Lukas Braun, Jonas Spielmann, Dmitry E Doronkin, Carola Kuhn, **Aleksandr Maliugin**, Dmitry I Sharapa, Isabel Huck, Jianing Bao, Steffen Tischer, Felix Studt, et al. Following the structural changes of iron oxides during reduction under transient conditions. ChemSusChem, 17(24):e202401045, 2024.

6.2 Methodology

Spin-polarized first-principles calculations were performed using the Vienna *Ab initio* Simulation Package.[127] VASP is a density functional theory framework based on a plane-wave basis and employs either pseudopotentials or the projector augmented-wave formalism.[88,128] Exchange–correlation effects were described within the generalized-gradient approximation using the PBE functional.[96] Long-range dispersion interactions were included via the Grimme D3 correction[141]. To improve the treatment of strong on-site correlations, we applied the DFT+U approach in the Dudarev formulation.[109] An effective Hubbard parameter of $U = 4$ eV was adopted following prior theoretical studies[75,144], yielding a satisfactory description of the key physical and chemical properties of hematite. The following valence electronic configurations were used for the pseudopotentials: Fe ($3d^7 4s^1$), O ($2s^2 2p^4$), and H ($1s^1$).

The plane-wave kinetic-energy cutoff was set to 450 eV. Brillouin-zone sampling employed Monkhorst–Pack meshes of $3\times3\times2$ for the $2\times2\times1$ bulk supercell of hematite (128 atoms) and $3\times3\times1$ for the slab of the same lateral size. Surface calculations were carried out using slabs separated by a 15 Å vacuum region to suppress interactions between periodic images. We considered the (0001) surface with an Fe-terminated (R-Fe) termination, previously reported as the most stable configuration.[80] Magnetic moments were oriented along the [0001] direction, consistent with antiferromagnetic ordering.[79] With these settings, the hydrogen adsorption energies on hematite were converged to within 0.05 eV, which is adequate for the objectives of this work. Electronic self-consistency was achieved with an energy tolerance of 10^{-6} eV, and ionic relaxation was converged to forces below 10^{-2} eV/Å. Gibbs free energies of adsorbates and reaction intermediates were evaluated within the harmonic approximation, and transition states were located using the Improved Dimer Method.[142]

6.3 Results

6.3.1 Formation of water on the surface of hematite

The reduction of hematite begins with the adsorption of hydrogen molecules on its surface, which provides the initial conditions for subsequent hydrogenation and oxygen-removal steps. In this work, we focus on the hematite (0001) surface with the R-O-Fe termination. This specific termination exposes both oxygen and iron atoms at the interface, making them sterically accessible and thus capable of acting as adsorption and reaction sites. Using density functional theory, we therefore seek to resolve the microscopic mechanism by which adsorbed hydrogen is converted into

surface hydroxyl species and ultimately into water, and to determine the sequence of elementary steps and intermediates governing this transformation.

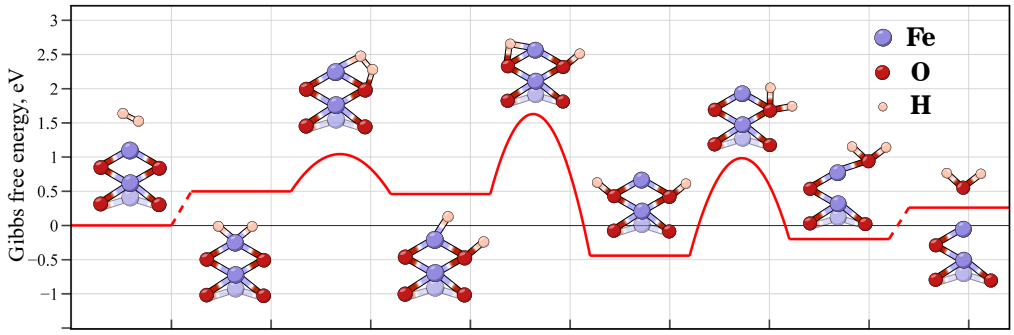

Figure 6.1: Gibbs free energy diagram of the reduction of the (0001) Fe_2O_3 surface at 673 K and hydrogen pressure of 1 atm with Fe–O–Fe termination. The reference system consists of a clean slab and a hydrogen molecule in the gas phase. Iron atoms are shown in purple, oxygen atoms in red, and hydrogen atoms in pale pink. The final state corresponds to a slab with one oxygen atom removed and a water molecule in the gas phase. Intermediate configurations and transition states are also schematically depicted in the figure.

In this work, we propose the reaction mechanism summarised schematically in the figure6.1 together with the corresponding Gibbs free-energy reaction diagram. The process starts with the physisorption of an H_2 molecule on the hematite surface. The adsorption site is an Fe atom; upon adsorption, its coordination environment becomes closer to the bulk-like one. The distance between the adsorption centre and the nearest hydrogen atom is approximately 2.17 Å.

Subsequently, the H–H bond undergoes heterolytic dissociation with an activation barrier of 0.54 eV, yielding two atomic hydrogen species: one bound to the Fe site and the other bonded to a surface O atom. The next elementary step is the migration of the H atom from Fe to a neighbouring oxygen site that is not yet hydrogenated. Already at this stage, the reaction becomes hindered by repulsive H–H interactions, as reflected by the relatively high activation barrier of 1.14 eV. Notably, the resulting configuration corresponds to the global minimum on the free-energy diagram, with $\Delta G = -0.44$ eV.

Water formation then requires overcoming the final remaining barrier, namely the approach of two hydrogen atoms toward the same oxygen atom. At $T = 673$ K, this barrier is approximately 1.18 eV. After crossing it, a water molecule is formed in which the oxygen atom originates from the hematite lattice. The resulting complex spontaneously lifts out of the surface oxygen plane. Subsequently, a barrierless desorption step becomes possible, in which the water molecule detaches, and an oxygen vacancy is created at the former lattice site. This vacancy formation increases the total energy of the system.

The reference state for the reaction diagram is the clean slab plus molecular hydrogen in the gas phase. In addition, an alternative pathway may occur in which H_2 adsorbs directly at an oxygen site and forms water in a single sequence of steps. In that case, the same diagram can be considered, but with the initial state shifted to the corresponding adsorbed configuration; within this reference, the process becomes effectively barrierless. Finally, we emphasise that the mechanism discussed here was evaluated at low surface coverage, corresponding to $1/6$ ML of hydroxyl species.

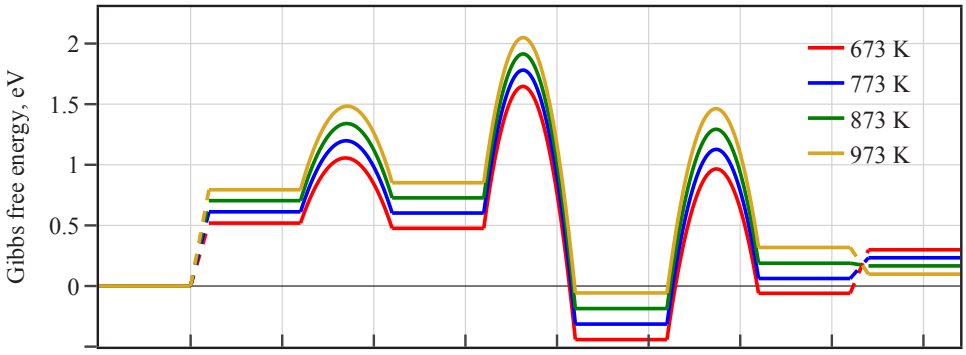

Figure 6.2: Gibbs free energy diagram of the reduction of the (0001) Fe_2O_3 surface for the set of temperatures ranging from 673 K to 973 K. The reference system consists of a clean slab and a hydrogen molecule in the gas phase.

This mechanism was evaluated at $T = 673$ K, 773 K, 873 K, and 973 K. The corresponding free-energy profiles are shown in Fig. 6.2. The diagram indicates that, with increasing temperature, all apparent barriers rise and the overall process becomes thermodynamically less favourable. This trend is primarily driven by the increasing entropic contribution of molecular hydrogen in the reference state, which shifts the free energies of the adsorbed intermediates upward as $-TS$ grows in magnitude.

An important exception is the final state, where an oxygen vacancy is present in the lattice and water has already entered the gas phase. In this case, the entropy of gaseous water provides a stabilising contribution that renders the final step thermodynamically favourable. As a result, the overall reaction approaches thermoneutrality at approximately $T = 1090$ K.

If one considers only the alternative pathway in which hydrogen adsorbs directly at a surface oxygen site (i.e., starting from the corresponding initial adsorbed configuration), the most favourable temperature window shifts to intermediate temperatures, with $T = 673$–773 K providing the strongest thermodynamic driving force.

6.3.2 Diffusion of hydrogen and water in hematite

In addition to the surface-mediated pathway discussed above, hematite reduction may, in principle, proceed via a bulk mechanism occurring within the interior of the solid. To assess whether such a pathway is thermodynamically feasible, we considered the formation of a water molecule inside a pore-like region of the crystal. Here, the term "pore" refers to a relatively large interstitial void inherent to the periodic crystal structure; i.e., this void is periodic and is not associated with extended defects such as cracks, grain boundaries, or dislocations.

Figure 6.3 summarises the free-energy landscape of candidate intermediate states that could, in principle, be involved in subsurface reduction. Introducing molecular hydrogen into the interstitial void strongly increases the system's free energy, indicating that H_2 residing in the pore is thermodynamically unfavourable. Although dissociation of H_2 and subsequent recombination steps among atomic hydrogen species partially lower the free energy relative to the molecularly adsorbed state, the overall pathway remains unfavourable over the considered conditions.

The lowest-energy defect-containing configuration along the bulk pathway corresponds to oxygen-vacancy formation inside the crystal, with $\Delta G \approx 0.55$ eV at $T = 673$ K. However, this value is still significantly higher than the corresponding surface vacancy formation free energy (0.30 eV), implying that reduction at the surface is thermodynamically preferred. Finally, the presence of a water molecule within the pore leads to a pronounced increase in free energy, further disfavoring bulk water formation under these conditions.

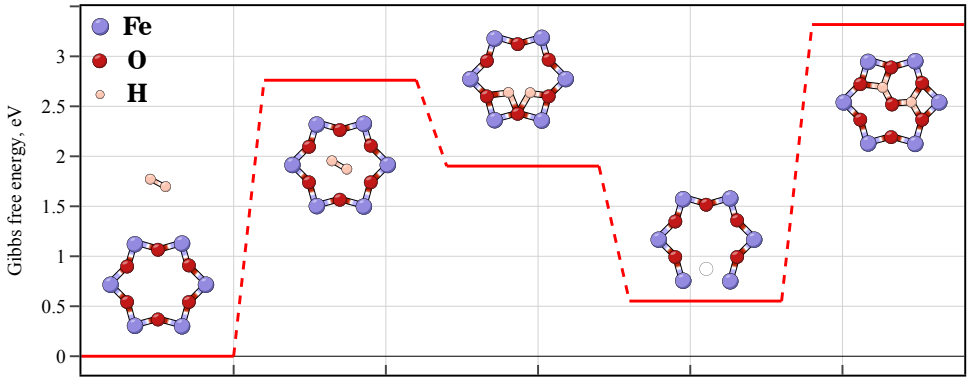

Figure 6.3: Gibbs free energy diagram for the hydrogen and water absorption in a hematite pore. Each state on the diagram (plateau) is accompanied by a schematic representation that qualitatively reflects the key features of the corresponding atomic configuration. Iron atoms are shown in purple, oxygen atoms in red, and hydrogen atoms in pale pink. The reference system consists of a bulk and a hydrogen molecule in the gas phase.

Increasing temperature further acts as a destabilising factor for the bulk pathway 6.4. As T rises, the free-energy penalty associated with confining hydrogen- and water-related species in the interstitial void becomes more pronounced, and the relative stability of bulk intermediates decreases. Consequently, elevated temperatures shift the bulk reduction route even further away from thermodynamic viability compared with the surface-mediated mechanism.

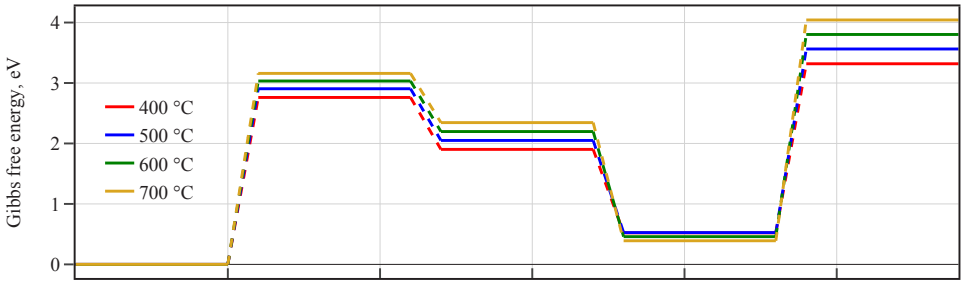

Figure 6.4: Gibbs free energy diagram for the hydrogen and water absorption in a hematite pore at the temperature range from 673 K to 973 K.

6.4 Conclusions

In this chapter, we examined hematite reduction via two limiting scenarios: a surface-mediated pathway and a bulk (subsurface) pathway. In both cases, the analysis focused on the elementary steps leading to water formation and on whether the formed water can be eliminated from the solid without prohibitive energetic penalties.

For the surface pathway, the calculated free-energy landscape indicates that the sequence of steps leading from molecular hydrogen adsorption to water formation is kinetically accessible, as suggested by activation barriers in a range compatible with experimentally relevant timescales. The overall outcome of this route is the creation of an oxygen vacancy at the surface, consistent with reduction proceeding through lattice-oxygen removal.

In contrast, water formation in the bulk is predicted to be strongly thermodynamically disfavoured. Moreover, once a water molecule forms inside an interstitial void, steric confinement prevents its migration out of the pore. Instead, the water molecule is expected to remain trapped and, if an oxygen vacancy is created nearby, to preferentially occupy (or passivate) that site (Fig. 6.4), rather than being released into the gas phase.

Taken together, these results suggest that hematite reduction is most likely to proceed predominantly at the surface, where both the formation and removal of water are feasible. If bulk reduction

occurs at all, it would require an additional mechanism for water removal that is absent in an ideal periodic crystal. One plausible scenario is that the local energy release associated with water formation and vacancy creation promotes structural damage (e.g., microcracking or the development of extended defects), thereby forming pathways for water to escape. Consequently, while both mechanisms may be feasible in principle, they are expected to prevail under markedly different external conditions and microstructural states.

7 Thermodynamic and transport properties of the liquid Fe-O system

7.1 Introduction

High-temperature oxidation of iron microparticles can proceed through regimes in which the reacting material is no longer adequately described as a purely solid core with a growing oxide scale. Recent combustion and post-mortem microscopy studies point to the formation of molten droplets during thermal runaway and to liquid–liquid segregation in the Fe–O system, manifested by core–shell morphologies and droplet-like inclusions that are naturally rationalised by a miscibility gap between oxygen-poor and oxygen-rich liquids. In such conditions, macroscopic parameters—burning rate, particle temperature history, mass gain, and the final microstructure—become sensitive to thermodynamic driving forces in the melt (chemical potentials, activities, phase stability) and to transport in the liquid state (self- and interdiffusion, viscosity, thermal conductivity). However, these properties remain poorly constrained at the relevant temperatures and oxygen chemical potentials, because direct in situ characterisation of molten Fe–O is experimentally challenging, transient, and strongly coupled to heat and mass transfer in the surrounding gas.

This chapter tackles this knowledge gap by constructing a physics-based, atomistically resolved description of liquid Fe–O using machine-learning interatomic potentials (MLIPs) trained on density-functional theory (DFT) reference data. The central objective is twofold. First, the aim is to provide a quantitatively reliable set of thermodynamic and transport properties for the liquid iron–oxygen system across compositions spanning metal-rich to oxide-rich melts, including conditions where liquid–liquid separation may occur. Second, the goal is to translate these atomistic predictions into forms that are directly applicable to experimental studies: parameterisations and trends that can be incorporated into continuum combustion/oxidation models, and diagnostics that connect measurable outcomes (e.g., particle morphology after quenching, rate laws, and temperature plateaus) to underlying liquid-state mechanisms.

Methodologically, the MLIP framework enables molecular-dynamics sampling on system sizes and time scales inaccessible to direct DFT simulations while retaining DFT-level fidelity for interatomic interactions. This makes it possible to compute composition- and temperature-dependent

equations of state, chemical potentials, and free-energy-related quantities, alongside transport coefficients obtained from equilibrium time-correlation functions or nonequilibrium protocols. Via systematic measuring uncertainties and validating against available high-temperature thermochemical and kinetic data, the resulting property set is intended to serve as a bridge between microscopic liquid-state physics and macroscopic combustion experiments. Ultimately, the chapter delivers a computational toolkit for interpreting and designing experiments on iron particle oxidation under regimes where molten Fe–O governs both reaction pathways and final microstructures.

This chapter is based on:

- **Aleksandr Maliugin**, Dmitry I. Sharapa, and Felix Studt. Molecular dynamics study of the liquid fe-o system using a machine learning interatomic potential. In preparation, 2026.

7.2 Methodology

All DFT electronic-structure calculations were performed using the VASP software package. A plane-wave basis set with a kinetic-energy cutoff of 450 eV was employed throughout. Exchange–correlation effects were described using the PBE functional. Brillouin-zone sampling was performed using Baldereschi-point averaging.[145] The electronic self-consistency criterion was set to 10^{-6} eV. For surface calculations, a 15 Å vacuum layer was introduced to avoid interactions between periodic images.

7.3 Results

7.3.1 Simulation within DFT-MD

7.3.1.1 Spin-polarized calculations

As a first step, it is necessary to assess whether spin-polarized molecular-dynamics simulations in the collinear approximation are feasible and computationally justified. To this end, a series of simulations for bcc iron at $T = 300$ K was performed using cells of different sizes and different Brillouin-zone sampling schemes. The time step was set to 2 fs, and the total trajectory length was 3000 steps. For the calculation with 250 atoms and an 8-k-point mesh, only 1800 steps were performed due to the substantially higher computational cost. The pressure was monitored in

Table 7.1: Comparison of average pressure for systems of different parameters. Pressure is given in kbar.

	128 atoms	250 atoms
1-k point	-1.53	31.13
8-k points	8.31	6.58

Table 7.2: CPUh comparison for systems with different parameters. The simulation with 250 atoms and 8 k-points is performed for 1800 steps.

	128 atoms	250 atoms
1-k point	1.9	7.7
8-k points	10.6	26.23

each case, since it provides a convenient thermodynamic indicator for characterizing the system. The results are summarized in Table 7.1.

The data show that finite-size effects have a pronounced impact on the predicted properties. At the same time, simulations using a 125-atom cell with a single k-point are expected to yield results consistent with significantly more expensive calculations employing denser k-point meshes and/or larger supercells. To illustrate the computational cost of such spin-polarized *ab initio* molecular dynamics, Table 7.2 also reports the corresponding CPU-hour requirements. Overall, the best compromise between accuracy and computational efficiency is achieved for cells containing on the order of one hundred atoms combined with single-k-point sampling.

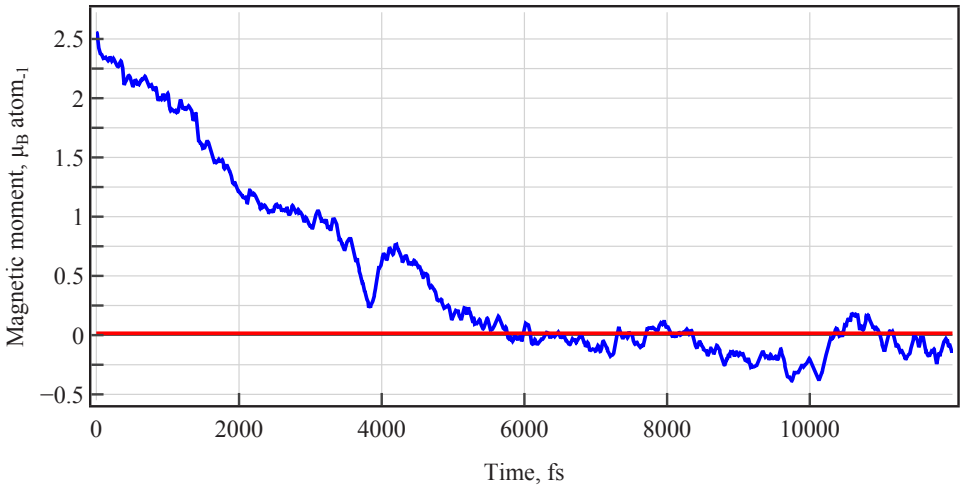

Figure 7.1: Evolution of the average magnetic moment during the DFT-MD simulation of fcc iron at 1600 K in NVT ensemble. The average value along the trajectory is marked with a red line and is approximately equal to zero.

The evolution of magnetic moments during the simulations is of particular interest. The magnetic subsystem relaxes on a much shorter timescale than can be resolved by molecular dynamics. Therefore, in spin-polarized *ab initio* MD the magnetic moment obtained at each time step should be understood as the instantaneous value that minimizes the electronic energy for the current atomic configuration, rather than as a dynamical trajectory of spins. Nevertheless, time-averaged magnetic moments provide meaningful information about the effective magnetic state of the material.

To analyse this behaviour, *ab initio* molecular-dynamics simulations are performed in the NVT ensemble using a Nosé–Hoover thermostat. The trajectory length was 6000 steps with an integration time step of 2 fs. At $T = 300$ K, the bcc phase is predicted to remain ferromagnetic, with an average magnetic moment of 2.33 μ_B per atom. By contrast, for the fcc lattice at $T = 1600$ K the simulations indicate an antiferromagnetic-like state, with a mean absolute magnetic moment of 2.14 μ_B.

Figure 7.1 shows the time evolution of the configuration-averaged magnetic moment. The simulations were initialized from a ferromagnetic state, with all moments constrained to be collinear. During the MD run, the signed average moment decreases nearly to zero, indicating that the moments become effectively disordered with respect to their orientation. At the same time, the average magnitude of the local moments remains close to the value characteristic of the ferromagnetic state (Fig. 7.2). Although such a state cannot be rigorously classified as paramagnetic within a purely collinear framework, the results clearly indicate that the fcc phase is not ferromagnetic under these conditions and instead favours a different magnetic arrangement.

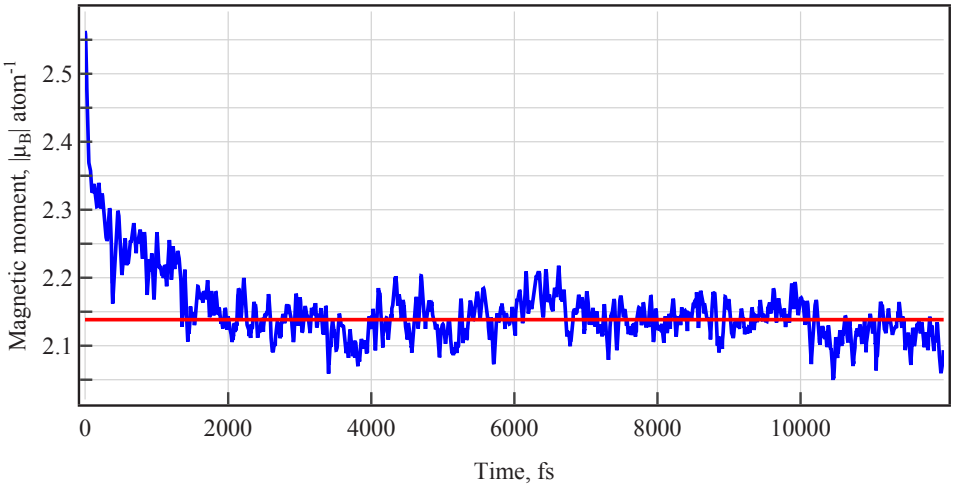

Figure 7.2: Evolution of the average absolute value of the magnetic moment during the DFT-MD simulation of fcc iron at 1600 K in NVT ensemble.

Experimentally, fcc iron is known to be paramagnetic in the relevant temperature range. Moreover, several studies have reported that treating the magnetic state of iron as paramagnetic improves the description of its phonon density of states and related thermodynamic properties.

7.3.1.2 Non-spin-polarized calculations

Because explicit magnetism, even within the collinear approximation, substantially increases the computational cost of *ab initio* molecular dynamics, it is instructive to quantify how spin polarization affects the thermodynamics of iron. To this end, the density was evaluated at ambient pressure and $T = 300$ K from a series of NVT simulations of bcc iron using a Nosé–Hoover thermostat. The density predicted by spin-polarized DFT–MD was found to be 8.125 g/cm^3, whereas non-spin-polarized simulations yield a significantly higher value of 8.934 g/cm^3. For reference, the experimental density is 7.87 g / cm^3, indicating that the inclusion of magnetic moments improves the agreement with the experiment.

However, when oxygen is introduced, self-consistent electronic minimization becomes markedly more demanding, and convergence slows down substantially. This raises practical concerns regarding the feasibility of DFT–MD for Fe–O systems. Therefore, simulations of a 108-particle system without spin polarization were conducted. Since our primary interest is the liquid phase in the temperature range 2000–3000 K, the thermodynamic and transport properties obtained with and without spin polarization are expected to be broadly similar.

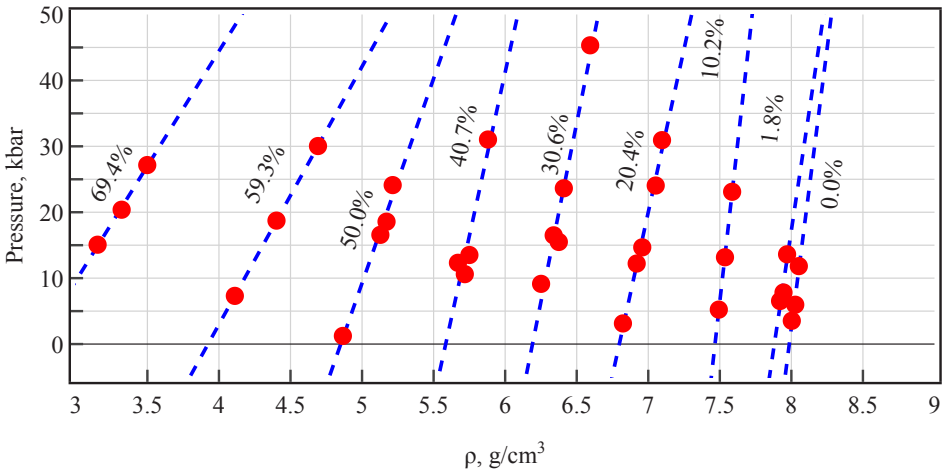

Figure 7.3: Calculation of the dependence of pressure on density at constant temperature of 2050 K. Each point corresponds to an independent DFT-MD simulation in NVT ensemble, from which the density and the mean pressure are extracted in order to determine the density at 1 atm.

In the following, the Fe–O system was investigated. For convenience, the composition is represented by the oxygen mole fraction x_{O}, such that the iron mole fraction is $1 - x_{\mathrm{O}}$. Accordingly, in the phase diagrams presented below the Fe-rich side is placed on the right, whereas iron oxides are located on the left.

This chapter focuses on obtaining thermodynamic properties from non-spin-polarized DFT–MD at (nominally) ambient pressure. Simulations were performed at $T = 2050$ K using a time step of 2 fs. Each trajectory comprised 5000 steps, corresponding to a total simulation time of 10 ps, which is sufficient to reach equilibrium and to extract the relevant observables. Because plane-wave DFT calculations depend on the simulation-cell geometry, electronic convergence can become noticeably more sensitive for non-orthogonal cells. As a result, performing simulations directly in the NpT ensemble is challenging. For this reason, the NVT ensemble was employed and thermodynamic properties were obtained at ambient pressure by extra- and interpolation of data computed at pressures different from the standard one.

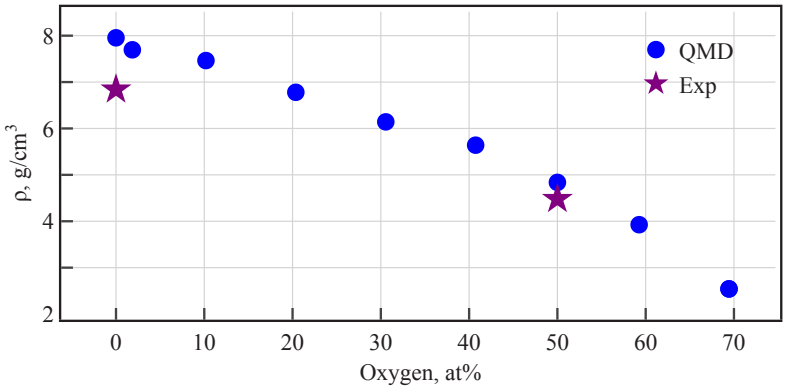

Figure 7.4: Density at 1 atm and 2050 K as a function of composition. The calculated data (QMD, blue circles) are compared with the experimental values (purple stars).[146,147]

Figure 7.3 shows the pressure–density relations for systems of fixed composition. For each composition, at least three simulations were carried out. The intersection with the zero-pressure line was taken as the condition corresponding to standard pressure. The resulting density–composition dependence is shown in the Fig 7.4. The discrepancy between the calculated and experimental densities is relatively large for liquid iron, whereas it becomes substantially smaller near the equimolar composition. This suggests that magnetic effects remain significant even in liquid iron, while their impact is considerably weaker for iron-oxide-rich compositions.

7.3.2 Training MLIP

Oxidation and reduction of iron and its oxides are, undoubtedly, highly complex and inherently multistep processes. An additional practical difficulty arises from the limited system sizes accessible when DFT is used as the primary tool for evaluating the potential energy. As discussed above, finite-size effects can be significant in molecular-dynamics simulations. This combination of factors motivates the use of a more computationally efficient approach to potential-energy evaluation. At the same time, it is desirable to retain DFT-level accuracy, since first-principles energetics constitute the central methodological foundation of this work.

Table 7.3: Sizes and root mean square deviations of the potential on the training and validation datasets.

	Train	Val
Size	1463	5041
RMSE of Energy, meV atom^{-1}	3.59	5.06
RMSE of Forces, meV Å^{-1}	205.3	196.7

In recent years, machine-learned interatomic potentials (MLIPs) have gained rapidly increasing popularity. While the existing approaches differ substantially in their architectures and engineering choices, they can be broadly grouped into three major classes: polynomial potentials, Bayesian-regression-based models, and neural-network potentials. In this work, a polynomial MLIP is employed, namely the Moment Tensor Potential (MTP). The functional form of MTP is constructed from tensor products of atomic position vectors; a detailed description is provided in a dedicated chapter 2.2.4. The implemented model is interfaced with LAMMPS, which enables efficient molecular-dynamics simulations.

As noted above, the central idea of MLIPs is to parameterize the potential energy as a function of the instantaneous atomic geometry. In principle, a wide range of input data can be used for training; here reference energies and forces were obtained from non-spin-polarized DFT calculations. The computational setup is consistent with the parameters described above; in this part of the work, the electronic convergence criterion was set to `EDIFF` $= 10^{-6}$.

An active-learning workflow was adopted in which new configurations are selected according to a criterion described in the referenced methodology. The initial training set contained a single configuration taken from the molecular-dynamics trajectory of the previous chapter. The training procedure was performed in parallel for compositions with $x_{\mathrm{O}} = 0\%$, 10%, 40%, 50%, and

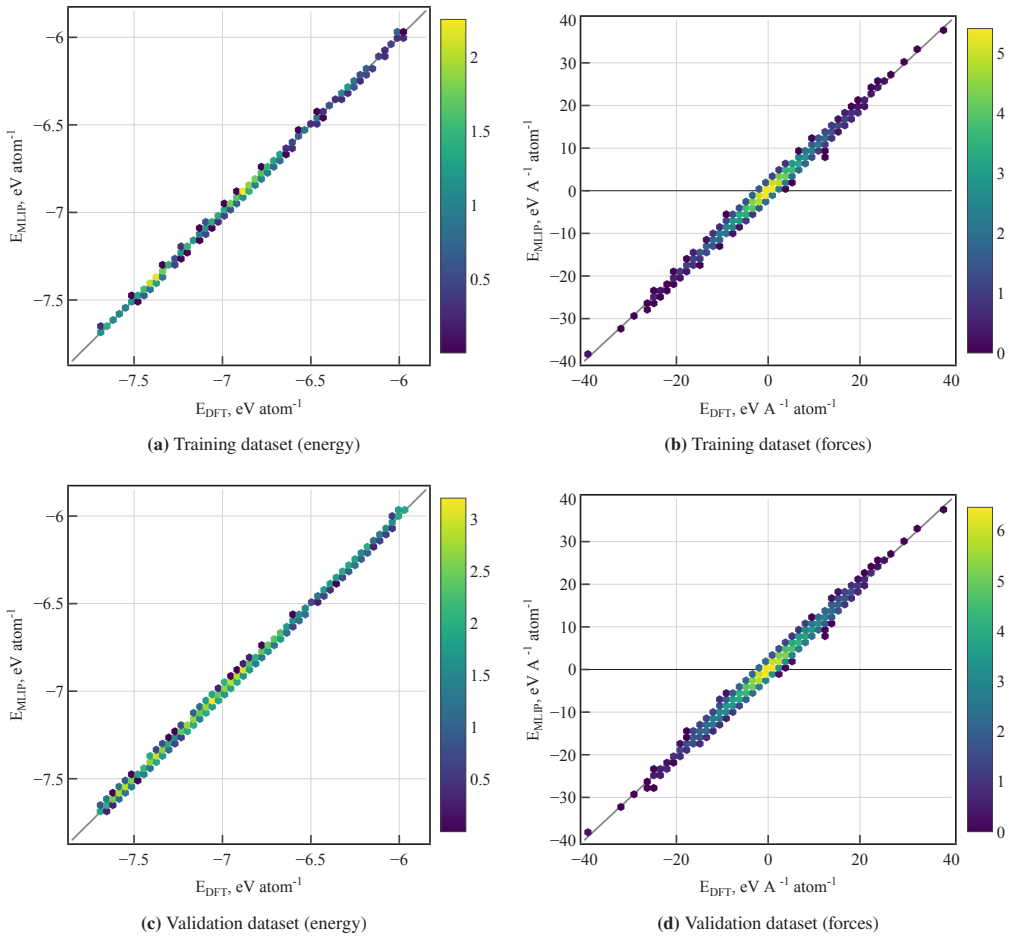

(a) Training dataset (energy)

(b) Training dataset (forces)

(c) Validation dataset (energy)

(d) Validation dataset (forces)

Figure 7.5: Accuracy of energy and force prediction using MLIP for training and validation datasets. The color bar on the right encodes $\log_{10}$ of the number of configurations in each bin, i.e., the color corresponds to $10^{(\text{colorbar value})}$ configurations.

60%, and subsequently extended to intermediate compositions. For each fixed composition, the active-learning campaign included NVT simulations with the following design:

- temperatures spanning 2000–3000 K in steps of 200 K;
- at $T = 2000$ K, additional runs with the system volume varied within $\pm 3\%$;
- slab configurations with an incoming oxygen molecule.

The active-learning loop produced training and validation datasets. The resulting training statistics are summarized in Table 7.3. Figures 7.5 illustrate the accuracy of the trained potential on both datasets. The heat map reports the base-10 logarithm of the number of configurations falling into each histogram bin.

During training, a large number of configurations were collected in parallel. However, it turns out that training a potential that is valid over the entire range of compositions of interest does not require using all configurations simultaneously. Within the active-learning procedure, only the necessary structures were selected from the full dataset for training, while the remaining configurations were reserved for validation. As a result, the constructed datasets exhibit a substantially larger validation set size (see Table 7.3).

7.3.3 Thermodynamic properties

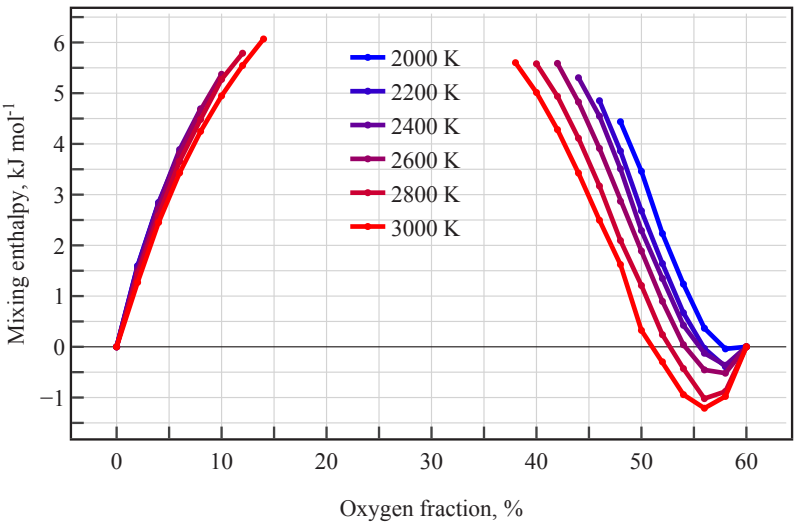

Figure 7.6: Mixing enthalpy of the liquid Fe–O system relative to the corresponding compound at 1 atm and temperatures from 2000 to 3000 K. Data were obtained from molecular dynamics simulations of a 4000-atom system.

To compute thermodynamic properties, a cubic simulation cell was populated by randomly distributing iron and oxygen atoms at the desired composition. The total system size was approximately 4000 atoms. Molecular-dynamics simulations were performed in the NpT ensemble using a time step of 0.5 fs. Each run comprised 200,000 steps, corresponding to a total simulation time of 100 ps.

To locate the boundaries of phase separation, An approach is used based on the Gibbs free energy of mixing, G_{mix}. Evaluating G_{mix} requires not only enthalpic data but also the entropy of the system. The entropy was computed using the two-phase thermodynamic (2PT) method described in the chapter 2. In practice, this procedure relies on the velocity autocorrelation function (VACF). The VACF was averaged over a time window of 50,000 MD steps, sampling the trajectory every 5 steps.

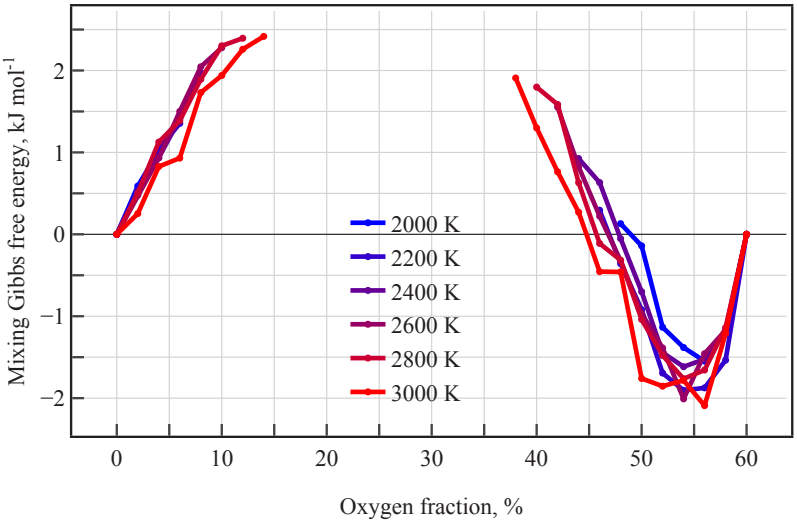

Figure 7.7: Gibbs free energy of the liquid Fe–O system relative to the corresponding compound at 1 atm and temperatures from 2000 to 3000 K. Data were obtained from molecular dynamics simulations of a 4000-atom system, with entropy evaluated using the two-phase thermodynamic (2PT) approach.

The resulting enthalpy of mixing is shown in Fig. 7.6. Within the investigated temperature range, the system exhibits clear non-ideal behaviour. Figure 7.7 further presents the composition dependence of the Gibbs free energy of mixing. The analysis shows that at $T = 3000$ K the Fe–O liquid displays a miscibility gap, i.e., a region of phase separation.

A particularly important feature of the Fe–O phase diagram is the immiscibility gap, which has attracted considerable attention in the literature. Within a certain temperature range, the system separates into two coexisting liquid phases: one is an Fe-rich melt containing only a small amount of dissolved oxygen (denoted L_1; for simplicity it is sometimes referred to as “liquid iron”), whereas the other is a near-equimolar Fe–O liquid (denoted L_2, i.e., liquid iron oxide). It is evident that this phase-separation behavior can strongly affect the oxidation and reduction processes of interest. Consequently, a quantitative understanding of liquid immiscibility in the Fe–O system is essential.

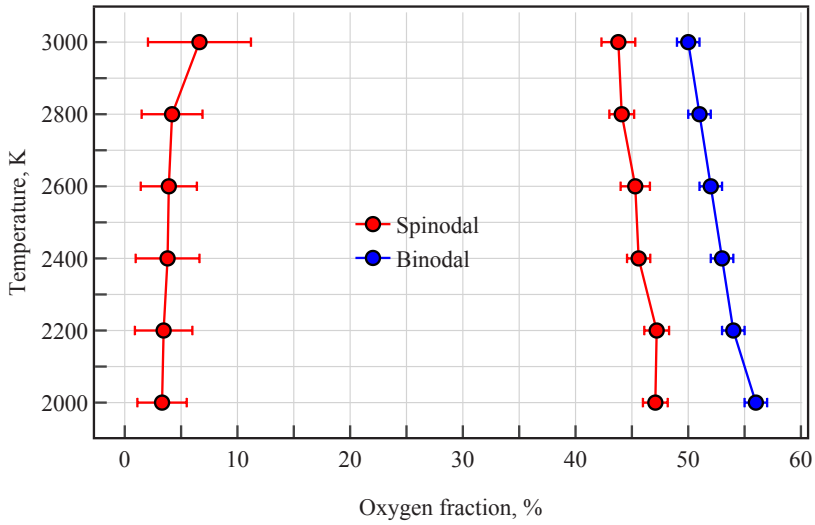

Figure 7.8: Binodal and spinodal curves in the iron–oxygen system obtained for temperatures in the range from 2000 to 3000 K. The binodal was determined using the common-tangent method, whereas the spinodal was evaluated using the thermodynamic stability criterion $(\partial^2 G_{mix}/\partial x_{\mathrm{O}}^2)_{T,P} > 0$, with the spinodal defined by $(\partial^2 G_{mix}/\partial x_{\mathrm{O}}^2)_{T,P} = 0$, where G_{mix} is the mixing Gibbs free energy and x_{O} is the oxygen mole fraction. The required second derivative was obtained via Gaussian-process regression of $G_{mix}(x_{\mathrm{O}})$.

7.3.4 Transport properties

The simulation settings used to evaluate transport properties are identical to those described in the previous chapter; here, however, the focus is on a different set of observables. Diffusion coefficients were determined from the Einstein relation based on the mean-squared displacement (MSD). The molecular-dynamics trajectories indicate that, under the present thermodynamic conditions, the ballistic and subdiffusive regimes are negligibly short. Consequently, the chosen trajectory lengths are sufficient to obtain well-converged diffusion coefficients. The results for iron and oxygen are summarized in Fig. 7.9. The data show that oxygen diffusion is more than twice as high in the oxygen-dilute regime (left side of the plot). Near the equimolar composition, the diffusion of iron—as the heavier species—remains only slightly slower.

Viscosities were additionally computed using the Green–Kubo formalism. Convergence of the time integral was ensured by employing MD trajectories substantially longer than the characteristic time scale L/v_s, where L is the simulation-cell size and v_s is the sound velocity. The results are shown in Fig. 7.10. As expected, the viscosity decreases with increasing temperature and with increasing oxygen content. These trends are consistent with the thermodynamic behaviour discussed above.

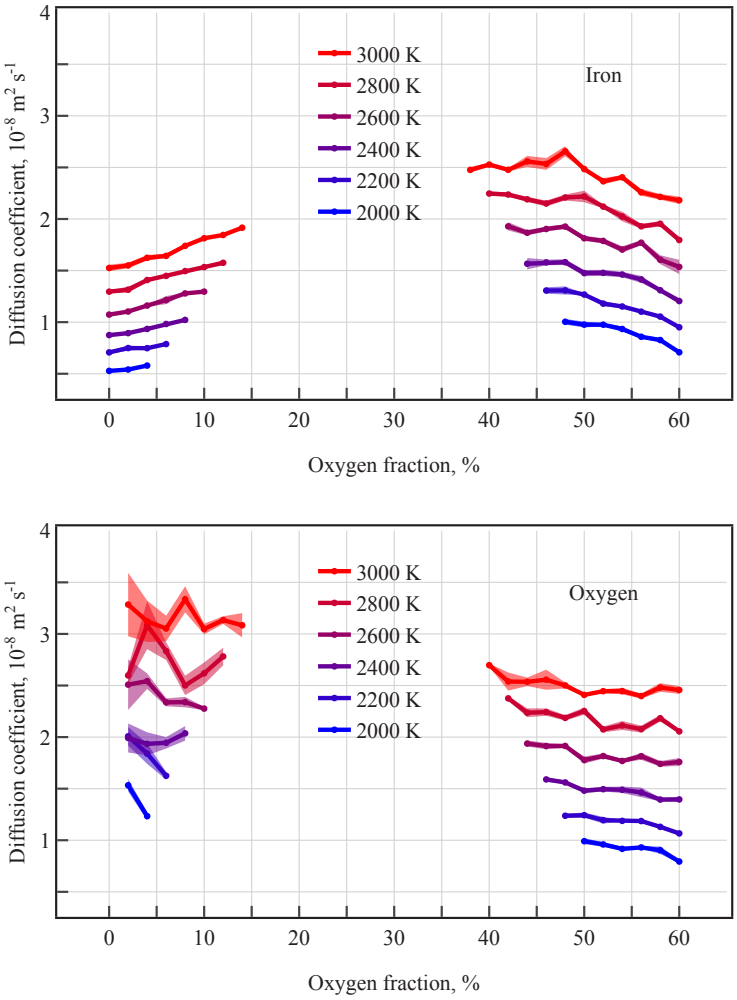

Figure 7.9: Diffusion coefficients of iron and oxygen for the liquid Fe–O system as functions of compound and temperature.

Finally, the composition dependence of the thermal conductivity of liquid Fe–O were calculated. Thermal conductivity was calculated using the reverse non-equilibrium Müller–Plathe method (rNEMD)[148], in which a kinetic-energy flux is imposed and the resulting temperature gradient is measured. The computed dependence is presented in Fig. 7.11. As is well known from the thermal-transport behaviour of the corresponding solids, similar tendencies persist in the liquid: increasing the oxygen content reduces the thermal conductivity. This suggests that liquid iron oxide acts as a thermal insulator in oxidation and reduction processes.

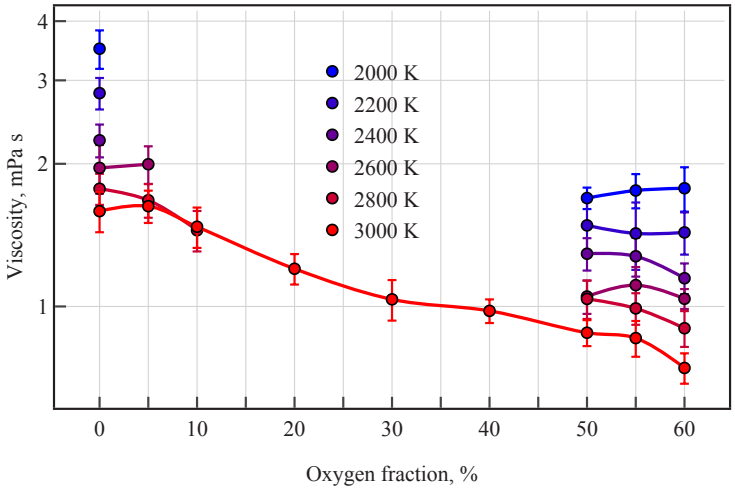

Figure 7.10: Viscosity of the Fe–O system as functions of compound and temperature.

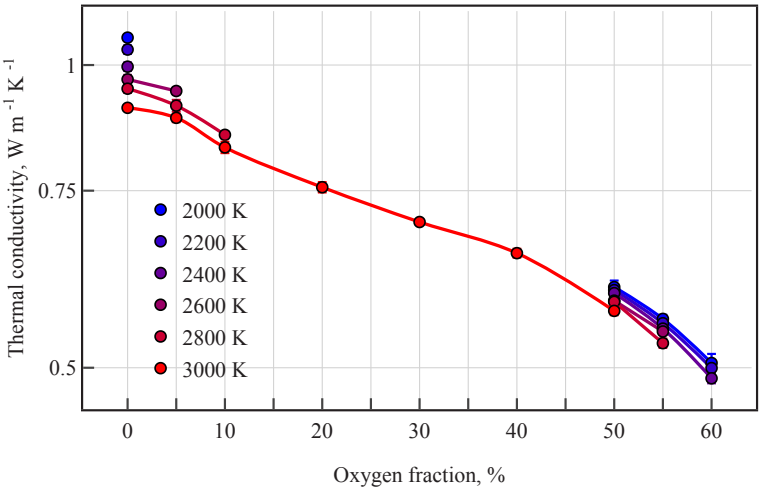

Figure 7.11: Thermal conductivity of the Fe–O system as functions of compound and temperature.

7.3.5 Immiscibility gap

As noted above, the Fe–O phase diagram exhibits an immiscibility gap. Its approximate boundaries can be inferred from the corresponding thermodynamic curves. Nevertheless, it remains of interest to examine how compositions within the nominal two-phase region behave during molecular-dynamics simulations, and whether the solubility limits can be extracted directly from an MD trajectory.

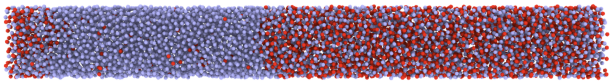

(a) Simulation cell after 1.25 ns of NpT molecular dynamics. Fe atoms are shown in purple and O atoms in red.

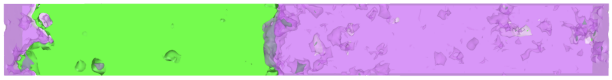

(b) Morphology of the structure. Iron phase (L1) is depicted in green and iron oxide (L2) one is shown purple. The simulation cell volume in panel (a) is discretized into polygons (equal-sized cubic voxels). For each voxel, the local fractions of oxygen and iron atoms are evaluated using a Gaussian-type weighting function. Based on these voxels, isosurfaces are then constructed: for L_1 at 90% iron and for L_2 at 45% oxygen.

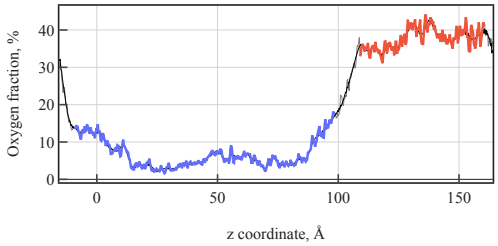

(c) Oxygen fraction over the z-coordinate based on simulations shown in (a).

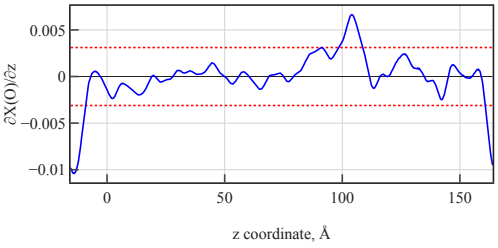

(d) Derivative of the oxygen fraction over the z-coordinate.

Figure 7.12: Determination of immiscibility gap. After 1.25 ns of molecular dynamics simulation in the NpT ensemble, the system reaches equilibrium. In the equilibrated configurations, the interface between liquid iron and iron oxide is clearly visible. The compositions of the respective phases can be determined from the MD trajectory.

A series of MD simulations was performed in the NpT ensemble with a time step of 0.5 fs. The initial configurations were constructed by combining two reference cells with $x_{\mathrm{O}} = 0\%$ and $x_{\mathrm{O}} = 60\%$, obtained from the thermodynamic calculations. The two cells were joined along the

z axis, resulting in strongly elongated simulation boxes, as illustrated in Fig. 7.12. In this way, nine target compositions were generated: 6%, 12%, 18%, 24%, 30%, 36%, 42%, 48%, and 54% oxygen. The total number of atoms exceeded 10,000, and the simulation time was approximately 1 ns.

During the molecular-dynamics simulations, the components redistribute within the simulation cell. Depending on the initial composition and temperature, iron and oxygen atoms migrate in response to gradients in chemical potential. As the system evolves, these gradients diminish; once the chemical potential becomes spatially uniform, the redistribution effectively ceases and the system reaches equilibrium. The primary observable extracted from the simulations is the oxygen concentration profile along the cell axis, $x_{\mathrm{O}}(z)$. For subsequent analysis, only the equilibrated portion of each trajectory were retained, i.e., the final 50 ps.

To determine the phase-separation boundaries, the resulting concentration profiles were smoothed using a Fourier-based filter, differentiated, and then an interfacial threshold was identified iteratively to define the phase boundary. This procedure provides a systematic way to extract the compositions of the coexisting liquids, L_1 and L_2. Figure 7.12 schematically illustrates the algorithm. The final output of the analysis is the mean composition of each phase together with its standard deviation.

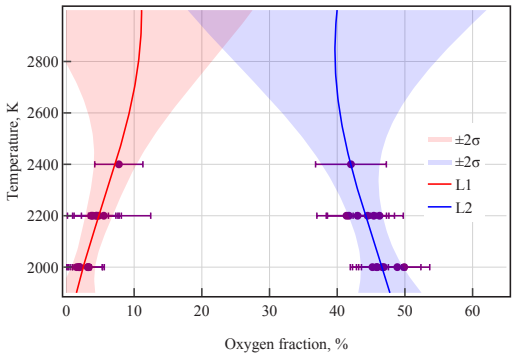

Figure 7.13: Phase diagramm of the Fe–O system. Molecular dynamics results are shown as purple points with standard deviation. The data were interpolated up to 3000 K using Gaussian process regression. The left and right branches correspond to L1 and L2, respectively. The shaded region represents twice the standard deviation.

The selected compositions were analyzed over the temperature range 2000–3000 K. It was found that the 48% and 54% oxygen systems remain fully homogeneous throughout this temperature interval. At temperatures below 2400 K, the coexistence compositions of L_1 and L_2 can be identified straightforwardly using the procedure described above. Starting from $\sim$2400 K, however, most compositions exhibit pronounced clustering, which prevents a robust determination of the immiscibility gap at higher temperatures because the medium becomes strongly heterogeneous.

This suggests that, during oxidation and reduction, phase separation may be accompanied by emulsion-like morphologies.

The simulation results are summarized in Fig. 7.13. In addition, the extracted coexistence data were post-processed using Gaussian-process regression. The large root-mean-square uncertainty of the extrapolated boundaries at elevated temperatures indicates that the miscibility limits cannot be predicted reliably in that regime.

7.4 Conclusions

In this chapter, thermodynamic and transport properties of liquid Fe–O were calculated. The study is deliberately comprehensive. The feasibility of molecular-dynamics simulations for extracting these properties under different first-principles settings was assessed, and the associated computational cost was evaluated. It was found that spin-polarised DFT–MD is impractical from the standpoint of efficiency, while the system sizes that are still computationally accessible are insufficient to capture the full range of phenomena relevant to oxidation and reduction of iron and its oxides. A primary bottleneck is the convergence of the electronic-structure problem at high temperatures, which becomes particularly severe upon introducing oxygen atoms into iron—a system in which Fe atoms largely carry local magnetic moments. In addition, DFT–MD is inherently affected by finite-size effects typical of statistical mechanics, further limiting convergence of the computed observables.

In this situation, the most promising strategy is to employ machine-learned interatomic potentials. Their flexible functional forms enable DFT reference data—in particular, energies and forces—to be parameterised as functions of the atomic configuration. In this study, the Moment Tensor Potential was employed, trained on configurations generated with DFT within an active-learning workflow. This approach produces an interatomic potential that is computationally efficient while retaining an accuracy close to that of the underlying DFT calculations. As a result, classical molecular dynamics can be adopted as the primary tool for exploring the Fe–O liquid.

Using the developed potential, thermodynamic and transport properties of the Fe–O system were computed. The study established composition-dependent trends of the relevant thermodynamic functions. The potential reproduces the presence of an immiscibility gap in the phase-equilibrium diagram, which results in the coexistence of two liquid phases: an Fe-rich phase (L_1) and a nearly equimolar Fe–O phase (L_2). Transport properties were also evaluated, revealing that, within the temperature range of interest, both the viscosity and thermal conductivity of L_2 are more than a factor of two lower than those of L_1. In addition, at temperatures above $\sim$2400 K the system

shows a tendency to form clusters, which likely reflects an emulsion-like morphology that may arise under practical conditions.

8 Molecular dynamics study of iron oxidation

8.1 Introduction

This chapter presents molecular dynamics simulations of oxygen uptake by liquid iron in two complementary geometries: a planar slab and a nanoscale droplet. These model systems are designed to bridge equilibrium descriptions of the Fe–O melt with the strongly non-equilibrium conditions relevant to high-temperature oxidation, where oxygen is supplied externally, and the reacting interface evolves in time.

By imposing a managed oxygen influx at the liquid surface, the time-resolved incorporation of oxygen, the formation of near-surface enrichment layers, and the subsequent redistribution of oxygen within the melt are tracked. The slab geometry enables a clean separation of the interfacial uptake from bulk transport, whereas the nanoparticle geometry captures curvature and finite-size effects that are directly relevant to particle oxidation experiments. The results are analysed in terms of uptake kinetics, transport-limited versus interface-limited regimes, and structural signatures of oxide-rich regions that can precede core–shell morphologies upon cooling.

This chapter is based on:

- **Aleksandr Maliugin**, Dmitry I. Sharapa, and Felix Studt. Liquid-state oxidation processes in the iron–oxygen system. In preparation, 2026.

8.2 Results

8.2.1 Mass and Thermal accommodation coefficients

Two important characteristics of gas–surface adsorption are the mass and thermal accommodation coefficients. The mass accommodation coefficient (MAC) can be defined as the probability that an incoming molecule impinging on a slab becomes adsorbed:

$$\mathrm{MAC} = \frac{n_{\mathrm{ads}}}{n_{\mathrm{total}}}, \tag{8.1}$$

where n_{ads} is the number of adsorbed molecules and n_{total} is the total number of incident molecules. The thermal accommodation coefficient (TAC) quantifies the fraction of thermal energy exchanged upon reflection when the incident molecule is not adsorbed, normalized by the maximum possible energy transfer at the slab temperature:

$$\mathrm{TAC} = \frac{T_{\mathrm{ref}} - T_{\mathrm{ins}}}{T_{\mathrm{slab}} - T_{\mathrm{ins}}}, \tag{8.2}$$

where T_{ins} is the temperature of the incident molecule, T_{ref} is the effective temperature of the reflected molecule, and T_{slab} is the slab temperature.

Both quantities can be evaluated using molecular dynamics in combination with the trained MLIP (the training procedure is described in the previous chapter). The simulations employed a slab containing 256 atoms at fixed composition, separated by 15 Å of vacuum on both sides. The slab temperature was set to 3000 K, whereas the incident molecule was initialized at 300 K. All trajectories were propagated in the NVE ensemble. For each composition, 1000 independent impact simulations were performed to obtain statistically meaningful averages. The resulting MAC and TAC values are shown in Fig. 8.1.

The trends are consistent with the expected adsorption behavior in the Fe–O system. Liquid iron exhibits a high MAC because the surface contains no oxygen and adsorption is therefore highly probable. As the oxygen mole fraction in the slab increases, MAC decreases, indicating that the impinging molecules are more likely to be reflected by oxygen-rich surface environments. It is possible that a slab containing 60% oxygen is thermodynamically unstable; however, this does not preclude transient adsorption events, since interfacial behavior is inherently dynamic. Moreover, a finite solubility of molecular oxygen in liquid Fe–O cannot be excluded.

Table 8.1: Mass and thermal accommodation coefficients.

Oxygen fraction, %	MAC, %	TAC, %
0	96.15	3.60
10	78.72	40.46
50	63.08	54.90
60	36.11	43.75

8.2.2 Oxidation of iron slab

Oxidation of an iron slab was simulated using molecular dynamics. The simulation cell is shown in Fig. 8.1. The bottom iron layers were kept fixed to represent a rigid substrate, whereas the remaining atoms were evolved in the NVT ensemble. An O_2 molecule was introduced above the slab every 2.5 ps and propagated in the NVE ensemble. During the simulation, the oxygen distribution was monitored as a function of height within the cell. The simulations were performed over the temperature range 2000–3000 K, and the results are summarized in Fig. 8.1.

At T = 2000 K, a well-defined reaction front is observed, separating the Fe-rich (L_1) and oxide-rich (L_2) liquid regions during oxidation. At $T = 3000$ K, no sharp front is visible, which may misleadingly suggest homogeneous oxidation. However, a more detailed analysis, together with the computed thermodynamic data, indicates that the system remains heterogeneous under these conditions. The apparent homogeneity in the height-resolved profile therefore reflects lateral inhomogeneity along the x and y directions, i.e., the formation of clusters at elevated temperatures.

When interpreting MD simulations, one should keep in mind that rare events occur much more frequently than in experiments. This is particularly evident for gas-phase simulations at low pressures, because the real volumetric concentration is far lower than what can be accommodated in a finite simulation cell. Consequently, the volumetric flux is artificially increased; in the present setup, at 1 atm and 3000 K it reaches 3640 m/s, which exceeds experimentally realistic fluxes by several orders of magnitude. This quantity approximately characterizes the collision rate of O_2 molecules with the slab and further highlights that oxidation proceeds much faster in MD than under real experimental conditions.

8.2.3 Oxidation of iron nanoparticle

In addition, molecular dynamics simulations of oxidation of a liquid-iron nanoparticle was performed. The simulations were carried out in the NVT ensemble at $T = 3000$ K. The nanoparticle

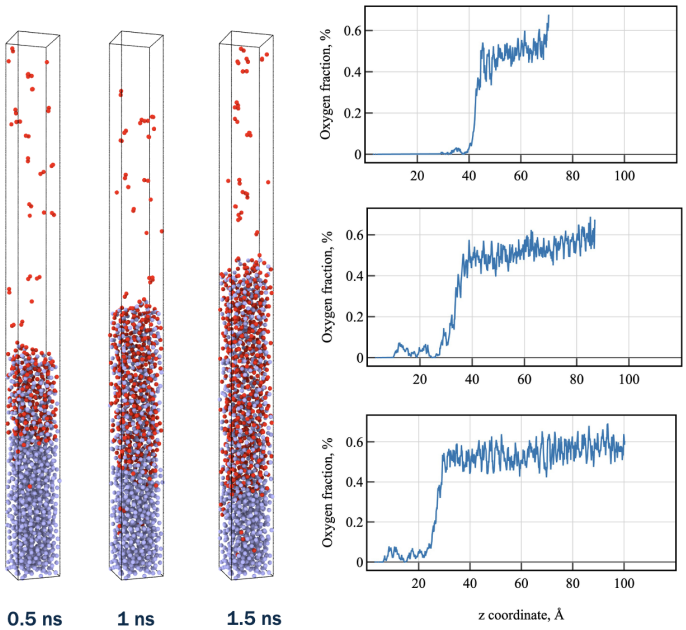

Figure 8.1: Molecular dynamics simulation of iron-slab oxidation by oxygen molecules at 2000 K. The figure shows snapshots taken 0.5, 1.0, and 1.5 ns after the start of the simulation. Iron atoms are coloured purple and oxygen atoms red. Under the simulation conditions, the oxygen volumetric flux is approximately 15 km/s. The right panel shows profiles of the oxygen atomic fraction along the z coordinate of the simulation cell.

was bombarded by O_2 molecules at a rate of one molecule every 0.25 ps, and the total simulation time was 3.5 ns. The higher oxygen-injection frequency compared with the slab-oxidation simulations arises because the nanoparticle simulation cell is much larger: it must expand not only along z, as in the slab case, but also along x and y. Since the available computational resources still limit the achievable trajectory length, the oxygen deposition rate was increased accordingly. Figure 8.4 shows the evolution of the total number of oxygen atoms in the system as a function of simulation time. This quantity can be interpreted as an approximate measure of oxygen uptake during oxidation.

The time trace exhibits a pronounced initial regime in which oxygen uptake is substantially higher than at later times. In this stage, intensive adsorption of oxygen molecules occurs, rapidly covering the entire surface of the liquid iron nanoparticle (schematically illustrated in Fig. 8.3). The subsequent stage corresponds to the formation of an oxide layer. This becomes possible because iron atoms intermittently protrude through the oxygen-covered interface and form transient Fe-rich clusters at the surface, which are then oxidized upon further oxygen impacts. As a result, a thin oxide shell emerges and subsequently thickens.

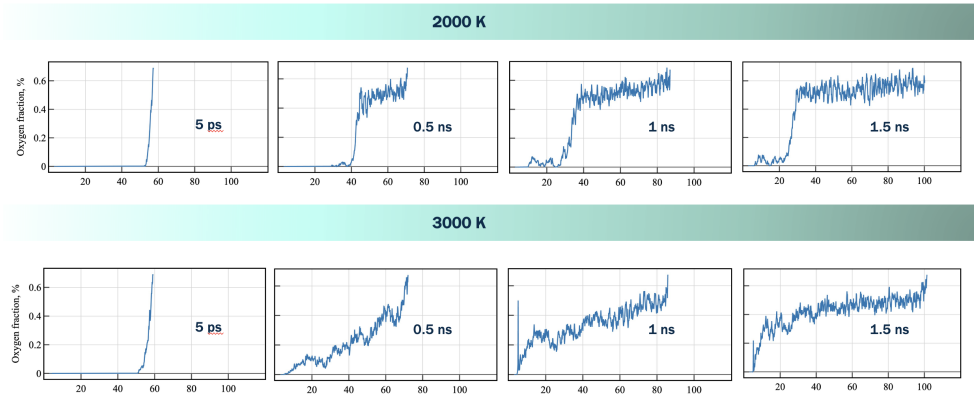

Figure 8.2: Profiles of the oxygen atomic fraction along the z coordinate of the simulation cell at 2000 K and 3000 K.

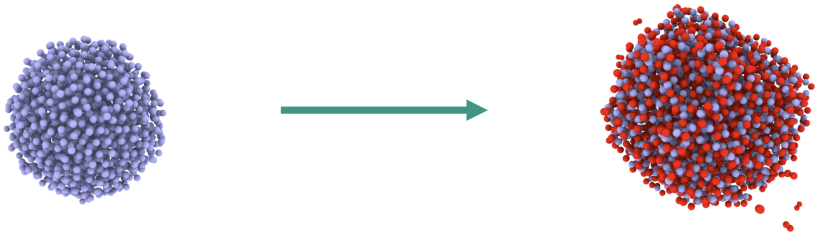

Figure 8.3: Simulation cell of the iron nanoparticle (left) and the iron oxide (right) obtained during oxidation in molecular-dynamics simulations.

As oxidation proceeds, the particle volume increases because oxide growth occurs both inward and outward relative to the original nanoparticle surface. A particularly notable intermediate regime is observed when the oxide volume is still insufficient to form a mechanically stable spherical shell: due to the viscosity contrast between the Fe-rich and oxide-rich liquids, the liquid oxide can flow over the iron-rich core. Finally, the process culminates in the formation of a closed oxide sphere and near-complete oxidation, where the remaining iron-rich phase becomes embedded within the liquid oxide. This final stage is the slowest step of the overall process.

In real experiments, the particle size is much larger and the volumetric flux is substantially lower. One may therefore expect oxidation to proceed closer to the slab-like scenario, i.e., via the formation of oxide clusters that can merge and develop into nuclei. However, these qualitative considerations are insufficient to determine how strongly such features affect the overall oxidation rate.

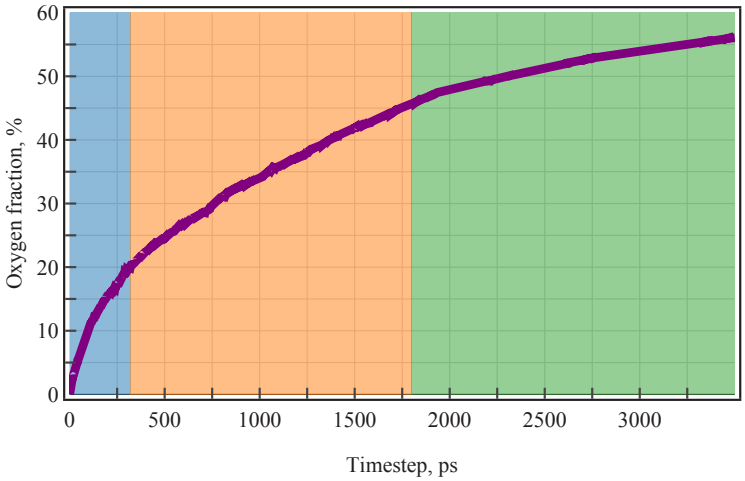

Figure 8.4: Consumption of oxygen atoms during the MD simulation of the oxidation of an iron slab. Three regions are identified schematically: the blue region corresponds to the adsorption stage, during which molecular oxygen dissociates and progressively covers the surface of the liquid iron nanoparticle. This is followed by the orange region, where rapid growth of the oxide-rich L_2 phase occurs. The process then slows down in the green region. It is assumed that the curve shown in the figure reaches a plateau upon complete oxidation. The figure illustrates that the formation of the oxide phase inhibits further oxidation.

8.3 Conclusions

In this chapter, adsorption and oxidation at Fe–O liquid interfaces were investigated using molecular dynamics with the trained machine-learned interatomic potential. The mass and thermal accommodation coefficients were employed as compact descriptors of interfacial uptake and energy exchange, and their evaluation was demonstrated using statistically converged ensembles of independent impact trajectories. The simulations show that liquid iron exhibits a high mass accommodation coefficient, consistent with efficient adsorption when the surface is free of oxygen. As the oxygen mole fraction in the slab increases, adsorption becomes less probable, and reflection events become more frequent, implying that oxygen-rich surface environments suppress sticking. Although oxygen-rich slabs with $x_O \approx 0.6$ may be thermodynamically unstable in bulk equilibrium, the interface remains intrinsically dynamic; therefore, transient adsorption remains feasible, and a finite solubility of molecular oxygen in liquid Fe–O cannot be excluded.

Direct simulations of slab oxidation under repeated O_2 impactsshow a pronounced temperature dependence of oxidation morphology. At 2000 K, the oxygen distribution along the surface normal displays a well-defined reaction front separating an Fe-rich liquid (L_1) from an oxide-rich liquid (L_2), consistent with two-liquid coexistence associated with the immiscibility gap. At 3000 K, no sharp front is apparent in the one-dimensional height profile, which could be misinterpreted

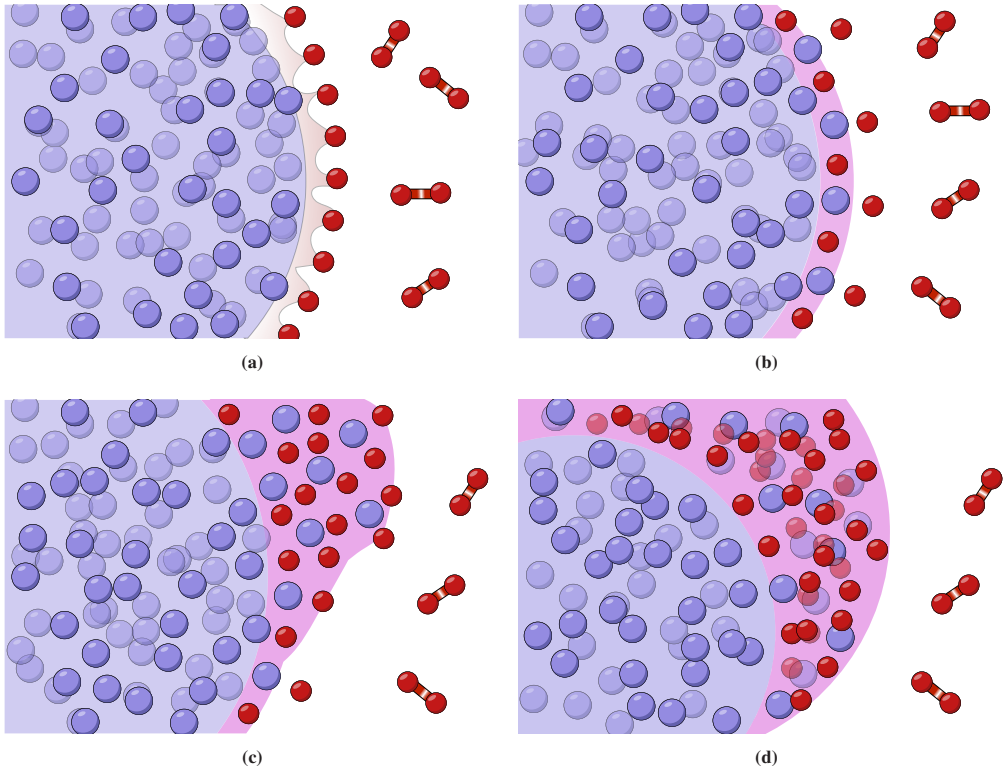

Figure 8.5: Oxidation mechanism of a liquid iron nanoparticle. First, molecular oxygen adsorbs on the particle surface and dissociates 8.5a. Subsequently, an oxide layer forms as oxygen atoms become incorporated into the iron layer, while adsorption and dissociation continue 8.5b. Next, an iron-oxide droplet develops and, due to the large viscosity contrast, migrates rapidly along the particle surface, promoting the growth of the oxide phase 8.5c. In the final stage, a liquid iron droplet remains and migrates within the newly formed iron-oxide nanoparticle 8.5d.

as homogeneous oxidation. A more detailed analysis, together with the thermodynamic trends established earlier, indicates that the system remains heterogeneous under these conditions; the apparent homogeneity along z reflects lateral inhomogeneity and clustering in the x–y directions at elevated temperature.

Oxidation of a liquid-iron nanoparticle at 3000 K further highlights the multistage nature of the process under intense oxygen flux. The time evolution of oxygen uptake exhibits an initial regime of rapid consumption, corresponding to extensive adsorption and near-complete coverage of the nanoparticle surface. This stage is followed by the emergence of an oxide layer, enabled by intermittent protrusion of iron atoms through the oxygen-covered interface and the formation of transient Fe-rich surface clusters that oxidise upon subsequent impacts. Once a thin oxide shell forms, continued oxidation leads to growth both inward and outward, resulting in a progressive

increase in particle volume. An intermediate regime is observed in which the oxide volume is insufficient to form a stable closed shell; in this case, the viscosity contrast between the Fe-rich and oxide-rich liquids promotes flow of liquid oxide over the particle surface. Ultimately, a closed oxide sphere forms andthe system reaches complete oxidation, with the remaining iron-rich phase embedded within the oxide-rich liquid. This final stage is the slowest step of the overall transformation.

9 Simulation of the liquid In-Me slab using machine learning force field

9.1 Introduction

Organic synthesis is generally performed at relatively low temperatures because many organic compounds are metastable with respect to thermal decomposition and, in extreme cases, ignition. An important exception is offered by low-melting metals, which are liquid under the conditions relevant here. Such liquid-metal environments are particularly attractive because they can act as unconventional catalytic media.

In modern petrochemical value chains, light olefins are key platform molecules that initiate multi-step pathways to a wide range of organic products.[149] Propane dehydrogenation (PDH) is strongly endothermic and therefore requires elevated reaction temperatures.[150] However, increasing temperature also promotes undesired pathways, including isomerisation, cracking, and coke formation, which together shorten the lifetime of the catalyst.[151] State-of-the-art Pt/γ-Al_2O_3 catalysts reduce these issues to some extent through the use of promoters. In particular, PDH is widely considered a structure-insensitive reaction, which implies that high activity can be achieved on very small ensembles—down to sub-nanometer clusters or even isolated metal atoms[152]. In contrast, the dominant side reactions are structure-sensitive and are closely linked to rapid deactivation via carbon deposition and associated catalyst degradation.[153]

A recently proposed and promising strategy is supported by catalytically active liquid metal solutions (SCALMS), which combines concepts from single-atom catalysis with enhanced resistance to coking[154–156]. In SCALMS, bimetallic liquid droplets are dispersed on a porous support; the droplet is enriched in a low-melting metal (e.g., Ga or In) that serves as a liquid matrix for a dilute, catalytically active transition metal[157,158]. To date, Rh, Pd, and Pt have been reported as active dopants for SCALMS-based dehydrogenation of light alkanes[159,160]. This architecture features a dynamic liquid–gas interface. A commonly invoked mechanistic picture is that the dopant atom undergoes cyclic migration between the droplet interior and the interface: in the absence of adsorbates, solvation in the bulk is thermodynamically favoured, whereas reactant molecules

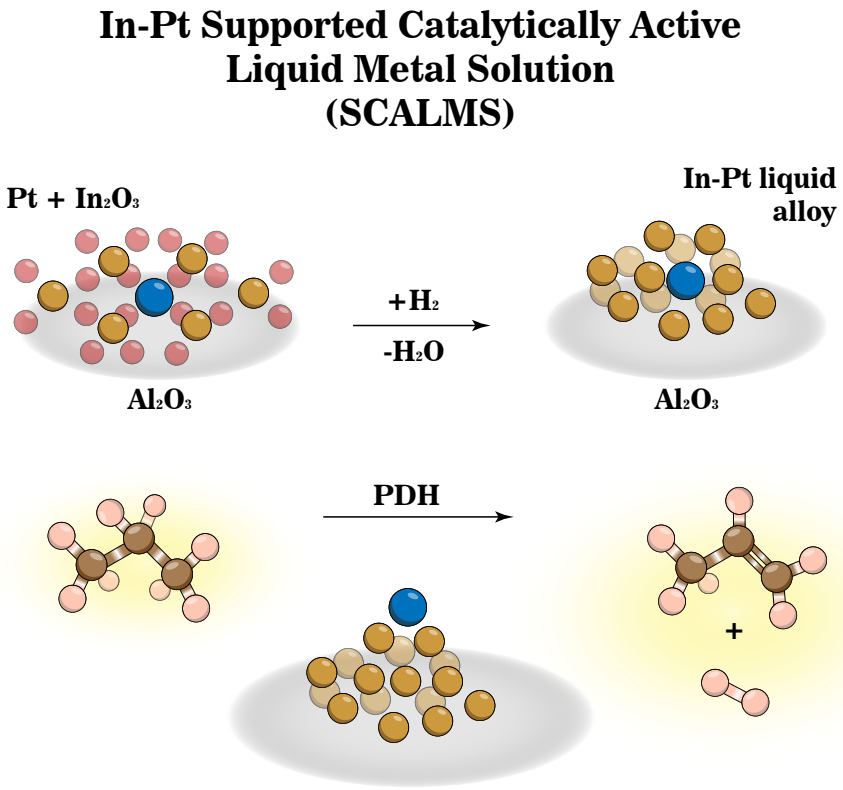

Figure 9.1: SCALMS concept. The method uses aluminium oxide as the support. The top panel shows a schematic of the catalyst preparation procedure, while the bottom panel illustrates the propane dehydrogenation (PDH) to propene. Indium atoms are shown in gold, oxygen atoms in red, the catalytically active atom in blue, the hydrocarbon species in brown, and hydrogen atoms in pale pink.

at the interface can transiently stabilise the dopant at or near the surface through complex formation. Subsequent C–H activation and β-hydride elimination are then proposed to yield the olefin and H_2, after which the olefin desorbs rapidly. Fast product removal is expected to suppress consecutive dehydrogenation and, consequently, reduce the propensity for coke formation.

In this chapter, first-principles simulation techniques are used to assess, at a mechanistic level, whether the proposed scenario is feasible. The behaviour of a bimetallic liquid slab is investigated at temperatures representative of propane dehydrogenation conditions, providing a qualitative analysis of adsorption and desorption processes at the liquid–gas interface.

This chapter is based on:

- Moritz Wolf, Thomas Gradl, Shaine Raseale, **Aleksandr Maliugin**, Narayanan Raman, Patrick Schühle, Nicola Taccardi, Michael Claeys, Dmitry I Sharapa, Felix Studt, et al. In-pt supported catalytically active liquid metal solutions for propane dehydrogenation–role of surface acidity of support. ChemCatChem, page e202402096, 2025.

9.2 Methodology

All electronic-structure calculations for the liquid surface were performed within density functional theory (DFT) as implemented in VASP[87,126,127,161]. Exchange–correlation effects were treated using the generalized gradient approximation (GGA) with the Perdew–Burke–Ernzerhof (PBE) functional.[96] The Kohn–Sham states were expanded in a plane-wave basis, and core–valence interactions were described using the projector augmented-wave (PAW) method[88,128]. The simulation cell (13 × 13 × 40 Å) contained an $In_{158}Pt_2$ slab with a thickness of 26.5 Å (see Fig.9.2). An energy cutoff of 300 eV and a 2×2×1 k-point mesh were employed to ensure total energy convergence. To minimize spurious interactions between periodic images along the surface normal, a vacuum spacing exceeding 10 Å was introduced.

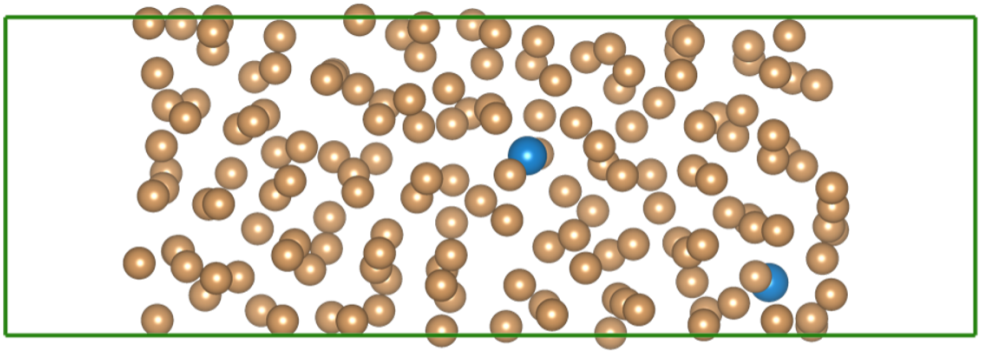

Figure 9.2: Snapshot of simulation cell with Pt atoms (blue) and In atoms (gold).

Because Pt is present at an extremely low concentration in liquid In (1:79), obtaining statistically meaningful information on the dopant distribution requires long molecular-dynamics (MD) trajectories. To make such sampling computationally tractable, a machine-learning force field (MLFF) approach was adopted[162], fitted to PBE reference energies and forces, which reduced the computational cost by approximately three orders of magnitude. MD simulations were carried out using a Nosé–Hoover thermostat[163] with a 10 fs time step at T=773 K. The force field was trained first on a pure In_{160} system and subsequently refined for $In_{158}Pt_2$.

9.2.1 MLFF training

Force-field training was carried out in two sequential stages. First a potential was trained on a pure In_{160} system and then continued training for the $In_{158}Pt_2$ slab (Fig. S1), yielding two dedicated potentials for the corresponding compositions. Importantly, the potential learned for pure In can be used as an initialization for related In-based liquid systems with comparable In-to-dopant ratios, thereby improving transferability and reducing the data requirements for subsequent fits.

To generate a representative liquid reference state, an In_{160} slab initially constructed in a bcc arrangement was melted in the NVT ensemble at 773 K using DFT-based MD for 10 ps. The resulting equilibrated liquid configuration was then employed as the starting point for on-the-fly MLFF training.

The learning curve for the first stage (pure In) is shown in Fig. 9.3. The final energy error reached 1.186 meV per atom, while the force error was 42.944 meV $Å^{-1}$ per atom. During this stage, 1272 local atomic environments were collected (note that these correspond to local configurations rather than full-cell geometries).

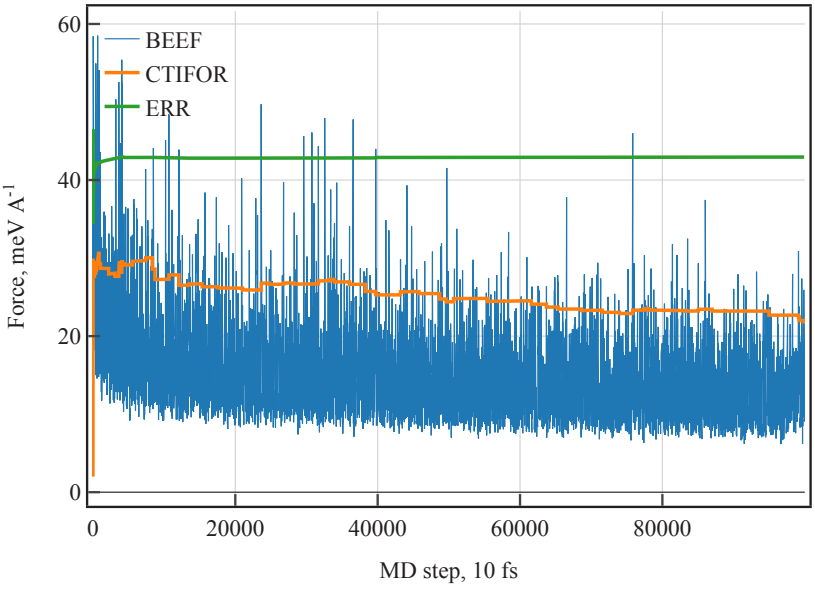

Figure 9.3: Training progress of the In_{160} system with BEEF (Bayesian error estimation of forces), CTIFOF (current value of threshold criterion), and ERR (root mean squared error of forces).

From the trained In potential, on-the-fly training was subsequently performed for the $In_{158}Pt_2$ slab using the same protocol, with errors increasing slightly to 1.302 meV per atom for energies

and 43.929 meV $Å^{-1}$ per atom for forces. At the same time, the number of sampled local configurations grew to 2918 for In and 896 for Pt.

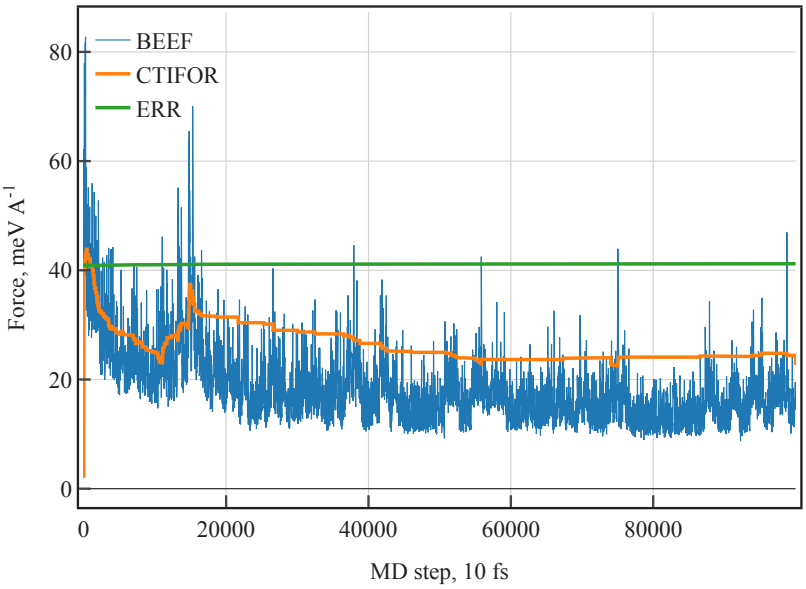

Figure 9.4: Training progress of the $In_{158}Pt_2$ system with BEEF (Bayesian error estimation of forces), CTIFOF (current value of threshold criterion), and ERR (root mean squared error of forces).

9.3 Results

9.3.1 Analysis of the position of the catalytically active center

To assess whether the catalytic scenario is feasible in principle, it is necessary to examine the behaviour of the dopant atom under thermodynamic equilibrium conditions. To this end, a series of relatively long molecular dynamics simulations was performed in the previously constructed simulation cell (see ref fig:inpt). Because the system of interest is a liquid slab that is symmetric and elongated along the z direction (normal to the slab surface), the z component of the dopant position—i.e., the dopant "height" relative to the slab, was monitored specifically. The resulting statistics are reported as the probability density of the dopant z-coordinate within the simulation box. Since a vacuum is present on both sides of the slab, the probability of finding atoms in those regions is zero.

As discussed above, dopant species of primary interest as catalytically active centres include Pt, Pd, Rh, and related transition metals. In this work, two model systems, $In_{158}Pt_2$ and $In_{158}Pd_2$ are considered. The corresponding probability density profiles are shown in the figures 9.6 and 9.5. In both cases, the indium distribution is nearly identical. Distinct peaks are observed, corresponding to the most probable In positions near the interface. This indicates that the liquid surface shows marked layering: regions near the interface resemble quasi-layered structures, reminiscent of crystalline planes with longer-range spatial organisation. The first and second layers are clearly resolved. In contrast, within the slab interior, the In distribution becomes almost uniform, implying efficient mixing and predominantly short-range order.

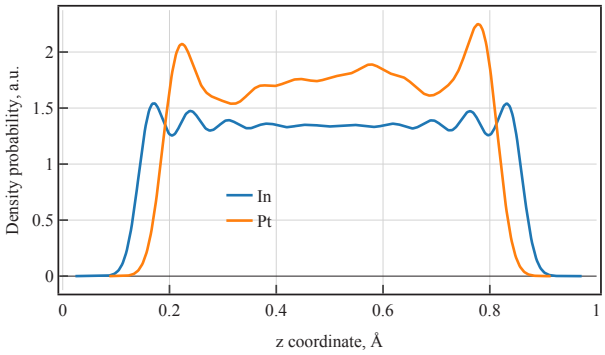

Figure 9.5: The density distribution function of particle detection relative to the direction orthogonal to the plane of the liquid surface for $In_{158}Pt_2$

The position distributions of the dopant atoms (Pt and Pd)—only two dopant atoms per simulation cell in each case—are noisier and visibly asymmetric. This distortion is a finite-size/statistics effect due to the small number of dopants; improved statistics would require a larger simulation cell. Nevertheless, the present data are sufficient to conclude that the dopant atoms reside predominantly in the slab interior, supporting the notion that the catalytically active species is, for most of the time, shielded from reactants in the ambient gas phase.

At the same time, there is a non-zero probability for a dopant atom to visit the slab surface. Such excursions are precisely the events during which an adsorption site for propane can form. A comparison of the near-surface maxima in the Pt and Pd probability profiles suggests that these events are not fully equivalent for the two dopants. In particular, the Pd maximum is shifted closer to the slab centre and nearly coincides with the second indium layer, whereas for Pt the first maximum lies between the first and second indium peaks. This trend implies that the probability of forming a surface-accessible adsorption centre may be somewhat lower for Pd than for Pt.

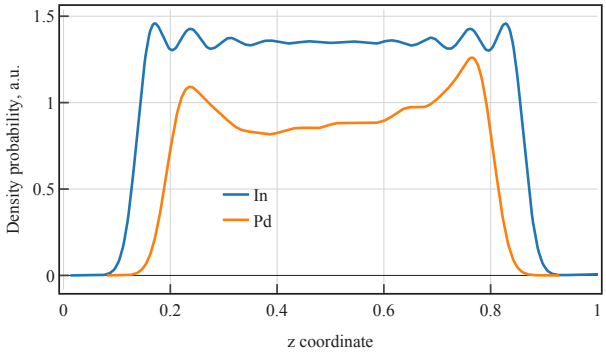

Figure 9.6: The density distribution function of particle detection relative to the direction orthogonal to the plane of the liquid surface for $In_{158}Pd_2$

9.3.2 Coordination number (CN) analysis

In order to estimate how frequently catalytically active atoms become surface-exposed, the time evolution of the coordination number as a function of the MD step was analyzed. The $In_{158}Pt_2$ system was examined in detail; it contains two Pt atoms, and a coordination number was evaluated for each of them. The CN analysis indicates that configurations that could, in principle, act as adsorption sites occur roughly once every 42.25 ps (Fig. 9.7). Visual inspection reveals that these events fall into two main categories: (i) undercoordinated Pt atoms located in the liquid bulk and (ii) Pt atoms exposed at the liquid surface. For the surface-exposed cases, adsorption is expected to be strongly suppressed by steric crowding from surrounding In atoms. Consequently, only a limited subset of the sampled configurations is likely to be able to bind a propylene molecule. In practice, therefore, events in which a Pt atom is truly accessible for adsorption occur even more rarely.

Overall, these observations support the hypothesis that the catalytically active center remains hidden from the reactant for most of the time, thereby suppressing coke formation. This shielding effect is critical for the technological relevance of the SCALMS concept.

9.3.3 Adsorption on the liquid surface

Propylene adsorption was examined using DFT-MD and found that the molecule desorbs spontaneously at both 473 K and 773 K. To quantify the adsorption energetics, it was proceeded as follows.

First, an MD snapshot of the $In_{158}Pt_2$ slab was seleted in which the target Pt atom exhibits a coordination number of 6 (identified as described above). A propylene molecule was then placed

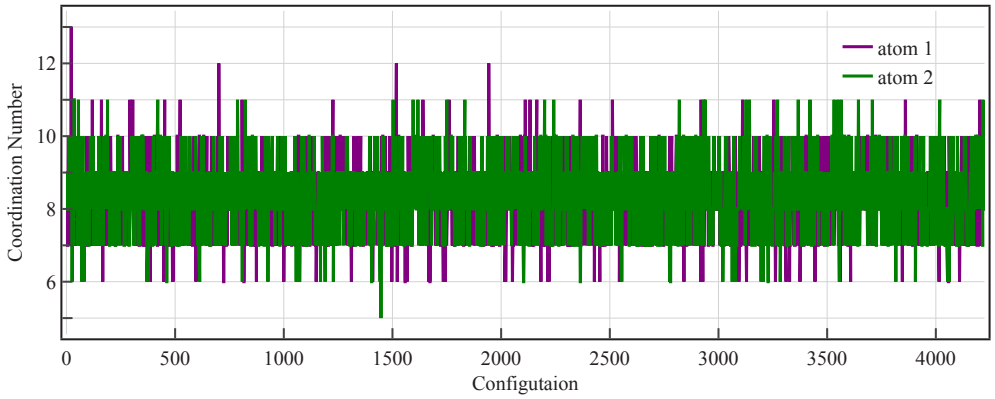

Figure 9.7: Coordination number of Pt atoms in $In_{158}Pt_2$ calculated during the MD simulation (trajectory length: 2 ns, snapshots each 500 fs, 1 occasion per (approx.) 42.25 ps).

on this Pt site in an adsorption-favorable orientation. A constrained geometry optimization was subsequently performed in which only the propylene molecule and the selected Pt atom were allowed to relax, while all remaining atoms ($In_{158}Pt_1$) were kept fixed. The resulting optimized adsorbed configuration is referred to as "Propylene*".

In addition, using the same underlying slab geometry, an analogous constrained optimization of the clean surface (i.e., without propylene) was carried out, relaxing only the same Pt atom and freezing all other atoms; this reference is denoted as "Slab". Finally, an isolated propylene molecule in the gas phase was optimized , denoted as "Propylene(g)". The desorption energy was then evaluated as:

$$E_{\mathrm{ads}} = E_{\mathrm{Propylene}*} - E_{\mathrm{Propylene(g)}} - E_{\mathrm{Slab}}. \tag{9.1}$$

The resulting value is approximately -0.17 eV for propylene. Even though this estimate is approximate, such a small magnitude indicates that the alkene does not form a stable adsorbed complex on the liquid surface. In contrast, the same protocol applied to propane yields an adsorption energy of about -2.69 eV, consistent with a strongly bound adsorbate.

Both trends were qualitatively corroborated by DFT-MD simulations. Propane remains associated with the catalytic surface and, importantly, tends to retain the Pt dopant at the interface. By comparison, propylene desorbs rapidly; once the surface is free of strongly bound adsorbates, the catalytically active Pt atom is more likely to migrate back into the liquid bulk. The C_3H_7–Pt–H complex was additionally simulated and it was found to be stable, persisting at the liquid surface over the simulated time window.

Taken together, these results suggest a thermodynamic driving force for adsorption of the reactant (propane) under the studied conditions, while the proposed intermediate C_3H_7–Pt–H is also stabilized at the interface. In contrast, the product (propylene) exhibits weak binding and readily desorbs from the surface, consistent with facile product removal in the SCALMS concept.

9.4 Conclusions

In this study, the atomistic feasibility of key elementary processes that are hypothesised to underpin catalysis in supported catalytically active liquid metal solutions (SCALMS) was assessed. In this concept, a low-melting metal (here In) forms a liquid matrix in which a dilute transition-metal dopant is dissolved and acts as the catalytic component. As a representative reaction system, propane dehydrogenation to propylene and hydrogen was considered. Because the relevant phenomena involve a liquid phase and a dynamically evolving liquid–gas interface, molecular dynamics (MD) is required to capture both structural fluctuations and rare surface-exposure events of the dopant. At the same time, conventional empirical interatomic potentials are typically not transferable across compositions and thermodynamic conditions and may not be reliable for bimetallic liquid interfaces. For this reason, a machine-learned interatomic potential was trained on reference data computed with DFT, enabling long-time sampling at a fidelity consistent with the underlying DFT description within the training domain.

A defining feature of SCALMS is the combination of (i) highly dispersed, atomically dilute active species—approaching the single-atom limit—and (ii) a liquid environment that can suppress unselective side reactions. Equilibrium MD simulations show that, in the absence of reactants (i.e., without propane), the dopant atoms (Pt and Pd) reside predominantly in the interior of the liquid slab. This observation supports the notion that catalytic centres are largely shielded from the gas phase for most of the time, which should reduce the likelihood of persistent surface-bound carbonaceous species and thereby mitigate deactivation pathways. Moreover, comparison of the near-surface maxima in the dopant z-probability density profiles suggests dopant-dependent differences in surface accessibility: Pt exhibits a higher propensity to occupy interfacial regions than Pd under the studied conditions, implying a greater likelihood of transiently forming an adsorption site. For the Pt-containing system, the characteristic time scale was additionally estimated on which a surface-accessible configuration emerges, providing a first measure of how frequently an adsorption centre can be generated.

To evaluate adsorption thermodynamics directly, a series of DFT-MD simulations and complementary constrained geometry optimisations for propane and propylene were performed. Propane was found to form a stable complex with Pt at the liquid interface, and the putative intermediate C3H7–Pt–H is also stabilised. Both species effectively pin the Pt dopant near the surface,

increasing the residence time of the active atom at the interface. In contrast, propylene does not form a stable surface complex and desorbs spontaneously from the doped liquid surface. The qualitative trends from DFT-MD are consistent with the quantitative adsorption/desorption energetics obtained from the constrained optimisation protocol.

Taken together, these results motivate the following mechanistic picture for propane dehydrogenation in SCALMS-like systems. Since catalysis requires both (i) the formation of a reactant–dopant adsorption complex and (ii) subsequent elementary steps such as C–H activation and hydrogen recombination, the overall turnover rate is expected to be sensitive to how often the dopant becomes surface-accessible. A sufficiently high propane partial pressure would therefore increase the probability of capturing the dopant during transient surface excursions and forming the strongly bound reactant complex. Once dehydrogenation proceeds and propylene is produced, the weak product binding promotes rapid desorption. After product release, the dopant can migrate back into the liquid bulk, thereby limiting the time spent in a surface-exposed state and suppressing consecutive dehydrogenation and coke-forming side reactions. This self-regulating relationship between transient site formation, strong reactant binding, and facile product desorption is consistent with the core rationale of the SCALMS concept.

10 Summary and Outlook

In this work, theoretical approaches for describing iron oxidation and the reduction of its oxides are examined. The principal objective was to develop a consistent methodology capable of providing both qualitative and quantitative insight into the trends and phenomena accompanying redox transformations in the Fe–O system in the solid and liquid states. The study includes calculations of thermodynamic (heat capacity, enthalpy, Gibbs free energy, etc.) and kinetic properties (diffusion coefficients, viscosity, thermal conductivity, etc.). To this end, state-of-the-art methods of electronic structure theory, statistical physics, and solid-state physics were employed. Finally, simulations based on machine-learned interatomic potentials were incorporated, enabling substantially larger system sizes and longer simulation times than are feasible with direct *ab initio* methods.

First-principles calculations constitute a powerful set of tools for predicting a broad range of properties of physicochemical systems. To assess the accuracy of the present approach, thermodynamic properties of iron and its oxides were calculated. The resulting set of thermodynamic functions defines the equation of state of the materials, thereby providing a comprehensive characterisation of the investigated system. The computed results were compared to experimental data and show good agreement. Phase-equilibrium diagrams for the Fe–O system under oxidising and reducing conditions were also constructed. These results demonstrate that *ab initio* calculations can predict the thermodynamic behaviour of the system with high accuracy.

One of the key conclusions of this work concerns diffusion coefficients in iron oxides. At the relatively high temperatures considered here, the dominant diffusion mechanism is vacancy-mediated transport, i.e., Schottky-type diffusion. To evaluate diffusion coefficients, first the temperature dependence of vacancy concentrations were determined, which governs the feasibility of atomic migration. For each oxide, all relevant migration pathways in the crystal lattice were systematically analysed. For each pathway, the corresponding transition state and activation barrier were identified. These quantities served as input for a Kinetic Monte Carlo code developed within this work, enabling the calculation of diffusion coefficients for both iron and oxygen in the considered oxides. In combination with the thermodynamic data, these results can be used for macroscopic kinetic modelling of redox transformations. Even at this stage, the calculations expose a clear imbalance in mass transport between iron and oxygen within a given oxide.

Specifically, iron migrates substantially faster in FeO and Fe_3O_4, whereas oxygen transport becomes dominant in Fe_2O_3. Based on these trends, plausible oxidation and reduction schemes were proposed. In addition, the computed data were used to estimate oxide-growth rate constants within Wagner's theory.

Despite the conventional theoretical picture of vacancy formation at elevated temperatures, one should also consider the possibility of atomic transport via interstitial positions, i.e., the Frenkel-type mechanism. In addition, it should be noted that the activation energies for atomic hops were evaluated for ideal crystals at fixed volume. A more rigorous treatment would require accounting, first, for the vacancy concentration and, second, for the temperature-dependent volume of the system. Incorporating these effects could, to some extent, improve the agreement of the calculated temperature dependence of diffusion coefficients.

The analysis of adsorption processes on iron and Fe_2O_3 surfaces indicates that oxygen coverage of iron is thermodynamically strongly favourable. At the same time, diffusion of oxygen and hydrogen through bulk iron is predicted to be fast. Further evidence that the solid–gas interface is not the rate-limiting stage is provided by the energetically accessible pathway for water formation on the Fe_2O_3 surface; the associated elementary steps are also relatively fast, particularly at elevated temperatures.

In parallel, the behaviour of water and hydrogen in interstitial regions of Fe_2O_3 was examined. The formation of a water molecule inside bulk Fe_2O_3 is found to be thermodynamically unfavourable, largely due to steric constraints. Nevertheless, hydrogen can penetrate into Fe_2O_3. This suggests that, if it occurs, bulk reduction is likely accompanied by mechanical disruption of the crystal lattice, promoting crack formation and increasing the porosity of the reduced product.

Another relevant oxidation regime involves high-temperature "burning" of iron particles. Under such conditions, particles melt and oxidation proceeds in the liquid state. Therefore thermodynamic and transport properties of liquid Fe–O were investigated. The feasibility of applying first-principles methods to the liquid was assessed, and DFT–MD was found to be computationally unfeasible regardless of whether spin polarisation is included. For this reason, a high-accuracy interatomic potential was trained on DFT reference data to enable large-scale modelling.

It is well known that the Fe–O phase diagram presents an immiscibility gap within the temperature range of interest, such that compositions in a certain interval separate into two coexisting liquids, L_1 and L_2. Using molecular dynamics driven by the trained MLIP, the solubility limits were determined, and additional thermodynamic and transport properties of both liquids were evaluated. The Fe-rich phase L_1 is found to be substantially more viscous, whereas the oxide-rich phase L_2 exhibits markedly decreased thermal conductivity and thus acts as a thermal insulator in oxidation and reduction processes.

Finally, molecular dynamics simulations of the oxidation of an iron slab and a liquid iron nanoparticle were performed. Several systematic features of the oxidation process were identified, and a schematic mechanism was proposed. In particular, at temperatures above approximately 2400 K, the system shows a strong tendency to form clusters, suggesting that, on macroscopic scales, the Fe–O liquid may develop emulsion-like morphologies.

However, the MTP potential still cannot capture all physicochemical phenomena inherent to this system. One key direction is to parameterize energies and forces using not only atomic coordinates but also magnetic moments, based on reference data obtained from collinear and potentially non-collinear DFT calculations. Such a potential would, first and foremost, substantially improve the agreement of the predicted density with experiment and would likely also correct some of the other thermodynamic and transport properties obtained from molecular dynamics. Explicit inclusion of magnetic moments could also affect oxidation simulations, because it would make it possible to track the O_2 dissociation mechanism in which radical and/or ionic atomic-oxygen species may form. This is not the only route toward a more physically faithful description. An alternative is to treat atomic charges explicitly, as proposed in [164]; in that case, magnetic effects would be incorporated implicitly, yet the overall agreement with experimental observables is also expected to improve relative to the present potential.

It is also important to emphasize processes involving hydrogen, such as oxidation of iron by water vapor and reduction of iron oxides by hydrogen. As is well known, classical molecular dynamics does not account for the quantum nature of hydrogen motion, which can substantially degrade the accuracy for hydrogen-containing systems. In such cases, more advanced approaches are required, for example path-integral molecular dynamics (PIMD), which explicitly incorporates quantum nuclear effects that are particularly pronounced for the extremely light hydrogen nucleus.

A particularly ambitious and scientifically attractive goal is the development of a single potential capable of describing all relevant materials and molecular species involved in iron oxidation and reduction. Such a potential would simultaneously cover both liquid and solid phases and would be able to predict melting and evaporation temperatures. Within this framework, it would become feasible to simulate the entire redox cycle—oxidation and reduction within a unified model—thereby rendering the proposed theoretical approach essentially comprehensive.

11 Appendix

11.1 Phase diagrams under oxidizing and reducing conditions in solid and gas phases

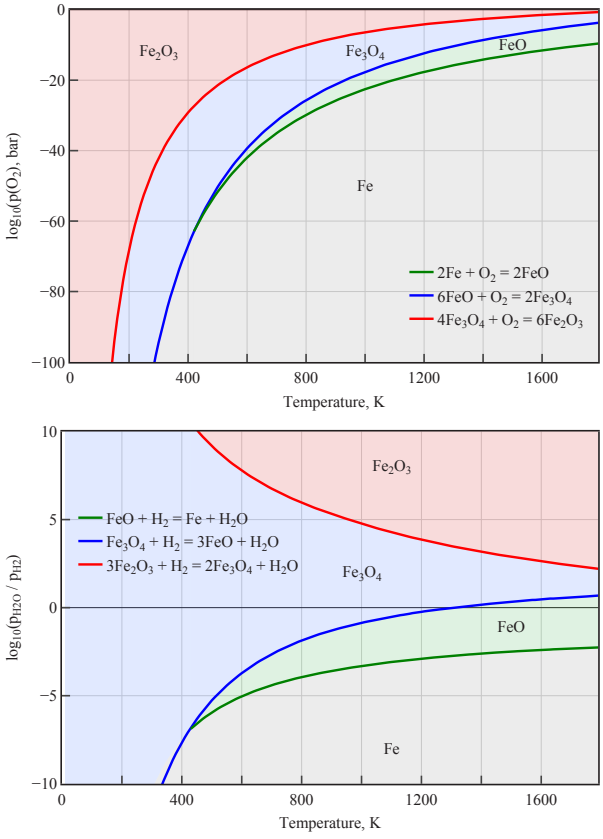

Figure 11.1: Phase diagrams under oxidising (top) and reducing (bottom) conditions in temperature-partial pressure coordinates of the gas components. Red indicates the stability region of Fe_2O_3, blue that of Fe_3O_4, green that of FeO, and gray that of bcc iron.

11.2 Migration pathways of iron atoms in Fe_3O_4

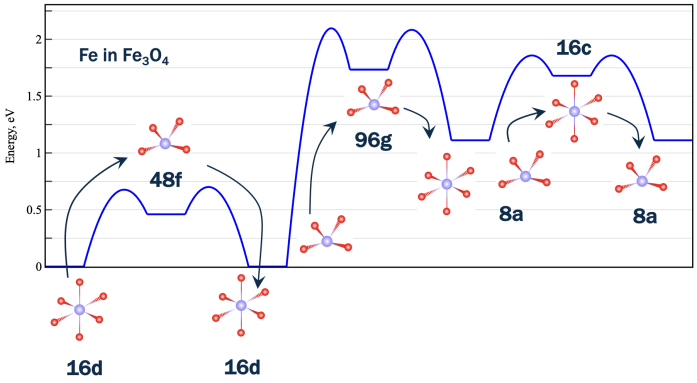

Figure 11.2: Migration pathways of iron atoms in Fe_3O_4. Sites are designated using Wyckoff positions: Octahedral site Fe_{oct} - 16d and tetrahedral site Fe_{tet} - 8a.

11.3 Oxidation of iron nanoparticle

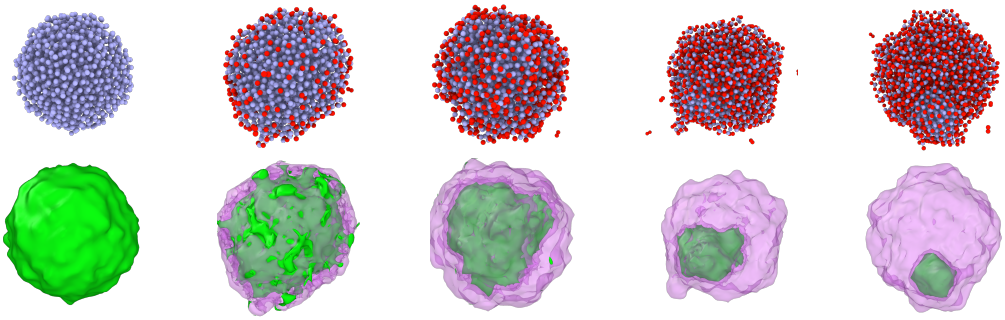

(a) 0.00 ns **(b)** 0.17 ns **(c)** 0.75 ns **(d)** 1.50 ns **(e)** 3.00 ns

Figure 11.3: Molecular dynamics simulation of the oxidation of liquid iron nanoparticle

The full molecular dynamics trajectory video is available at DOI: 10.5445/IR/1000190864.

11.4 Oxidation of iron slab

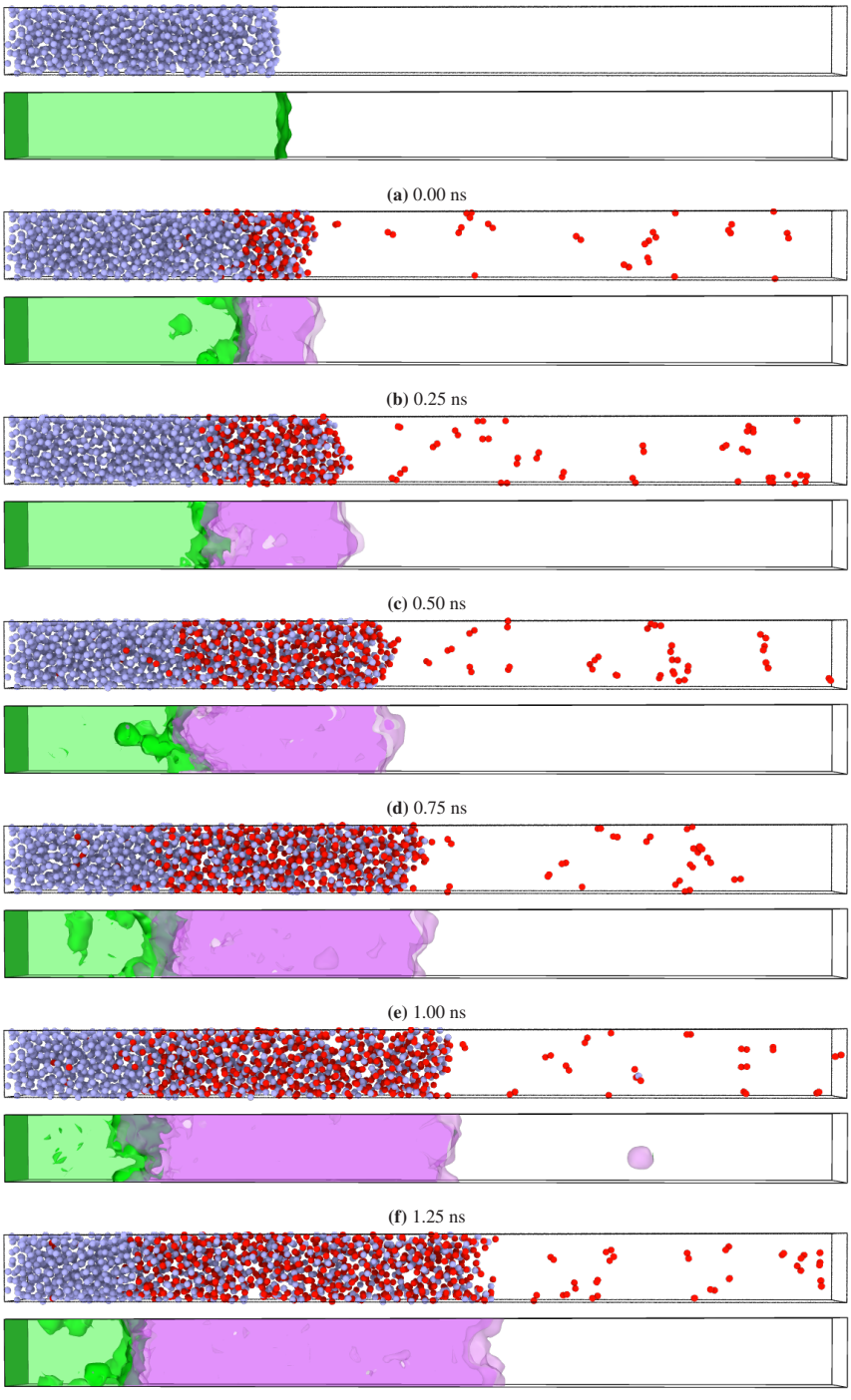

(a) 0.00 ns

(b) 0.25 ns

(c) 0.50 ns

(d) 0.75 ns

(e) 1.00 ns

(f) 1.25 ns

(g) 1.50 ns

Figure 11.4: 2000 K

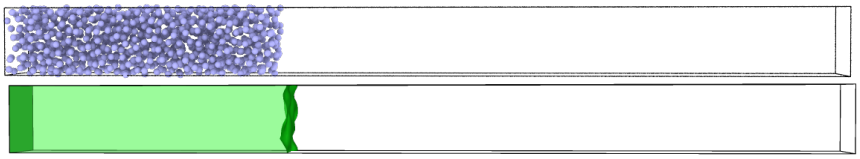

(a) 0.00 ns

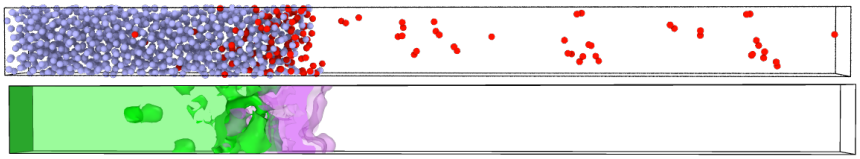

(b) 0.25 ns

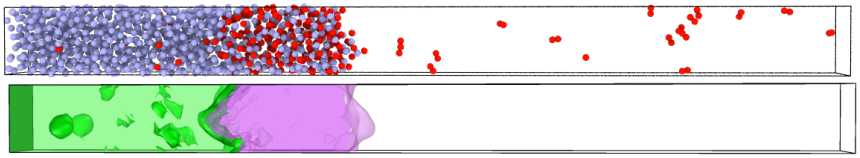

(c) 0.50 ns

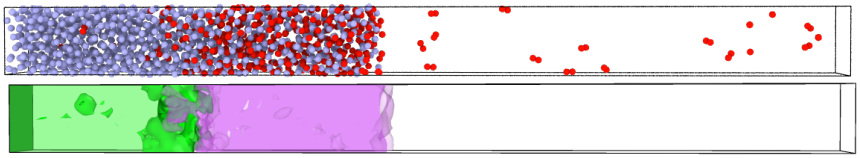

(d) 0.75 ns

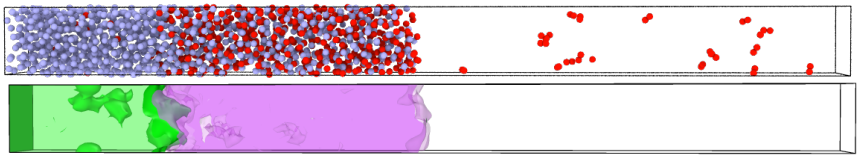

(e) 1.00 ns

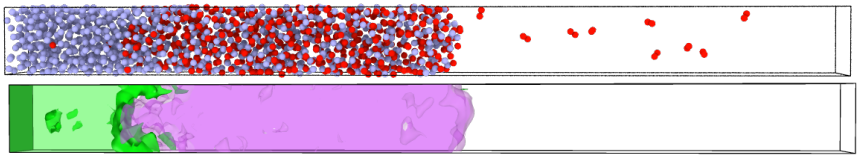

(f) 1.25 ns

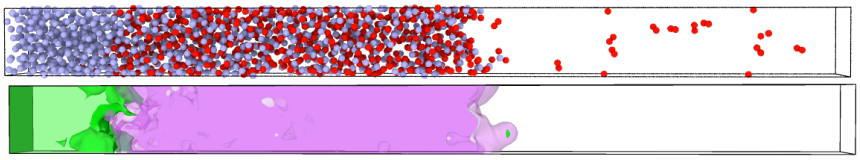

(g) 1.50 ns

Figure 11.5: 2200 K

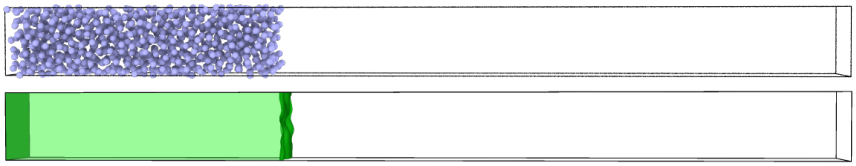

(a) 0.00 ns

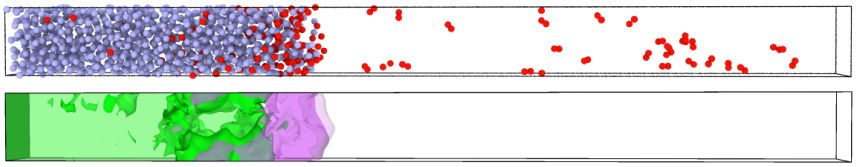

(b) 0.25 ns

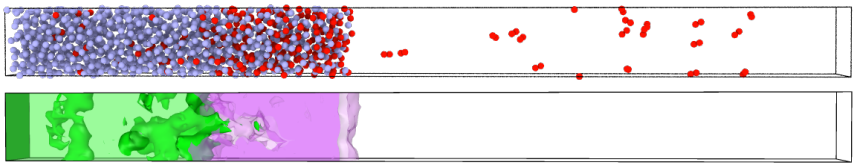

(c) 0.50 ns

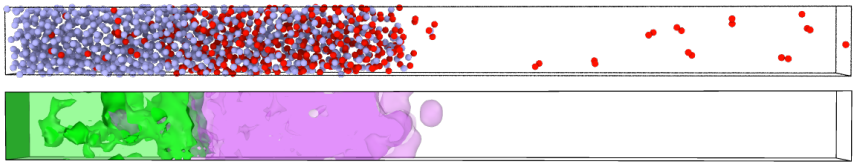

(d) 0.75 ns

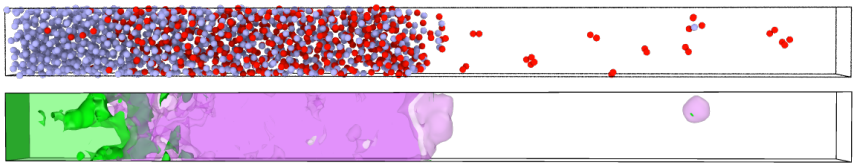

(e) 1.00 ns

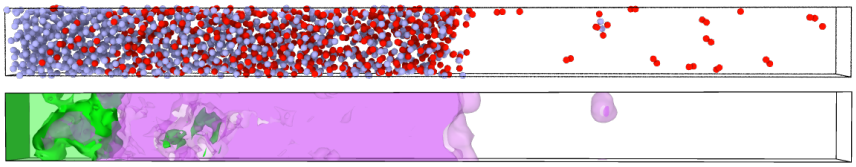

(f) 1.25 ns

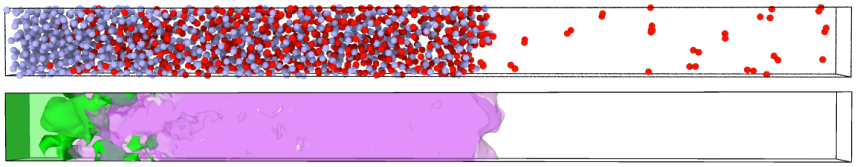

(g) 1.50 ns

Figure 11.6: 2400 K

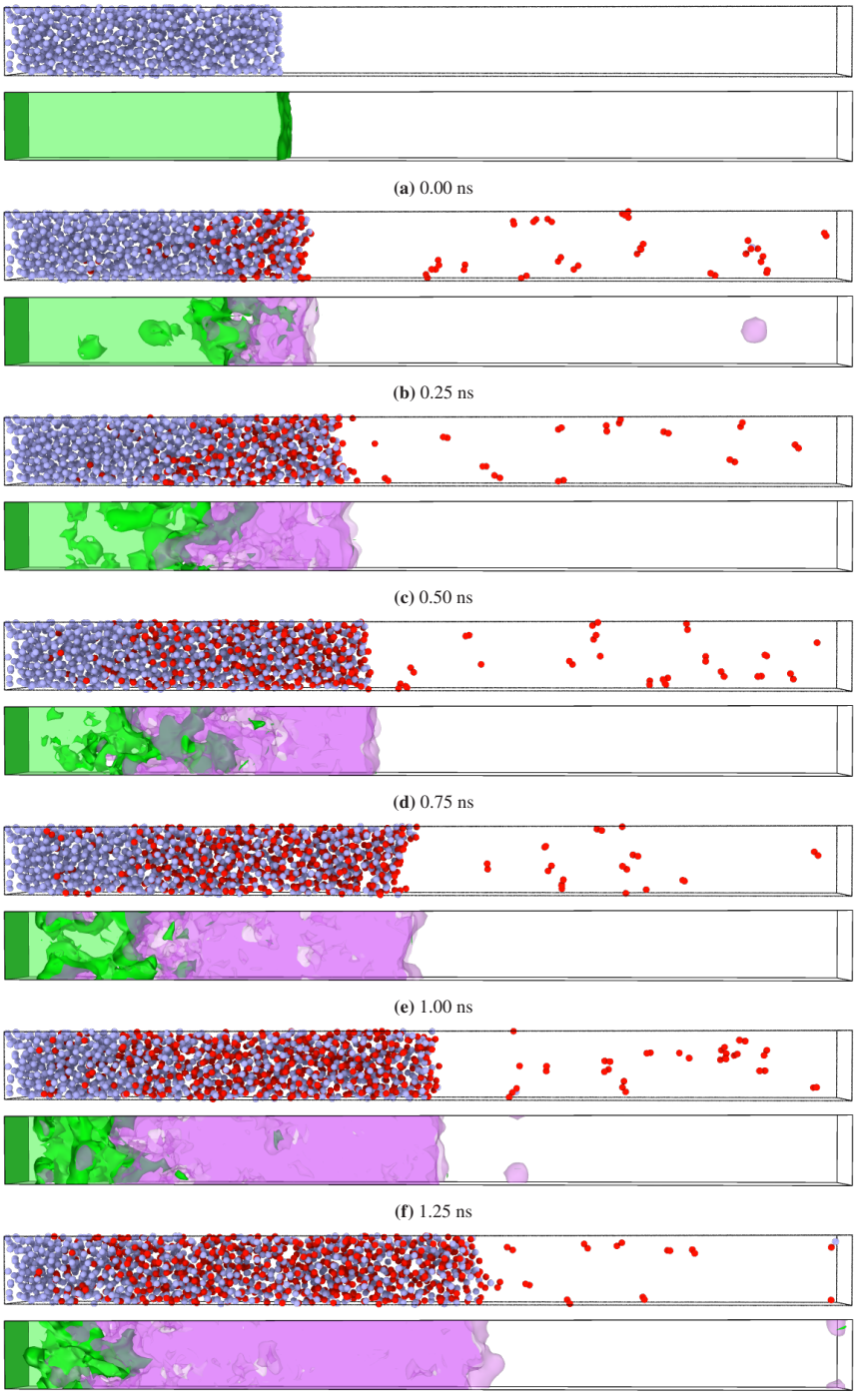

(a) 0.00 ns

(b) 0.25 ns

(c) 0.50 ns

(d) 0.75 ns

(e) 1.00 ns

(f) 1.25 ns

(g) 1.50 ns

Figure 11.7: 2600 K

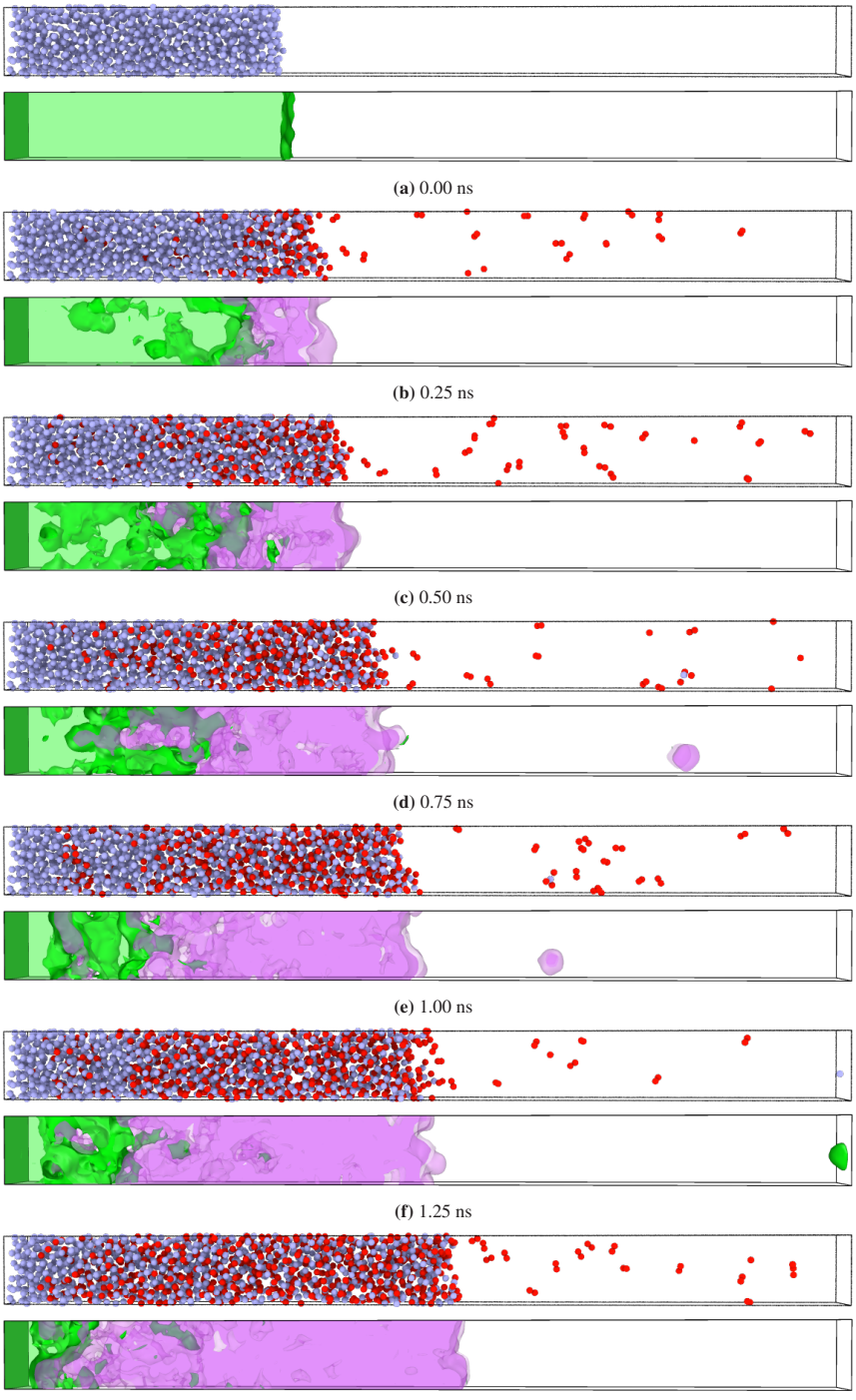

(a) 0.00 ns

(b) 0.25 ns

(c) 0.50 ns

(d) 0.75 ns

(e) 1.00 ns

(f) 1.25 ns

(g) 1.50 ns

Figure 11.8: 2800 K

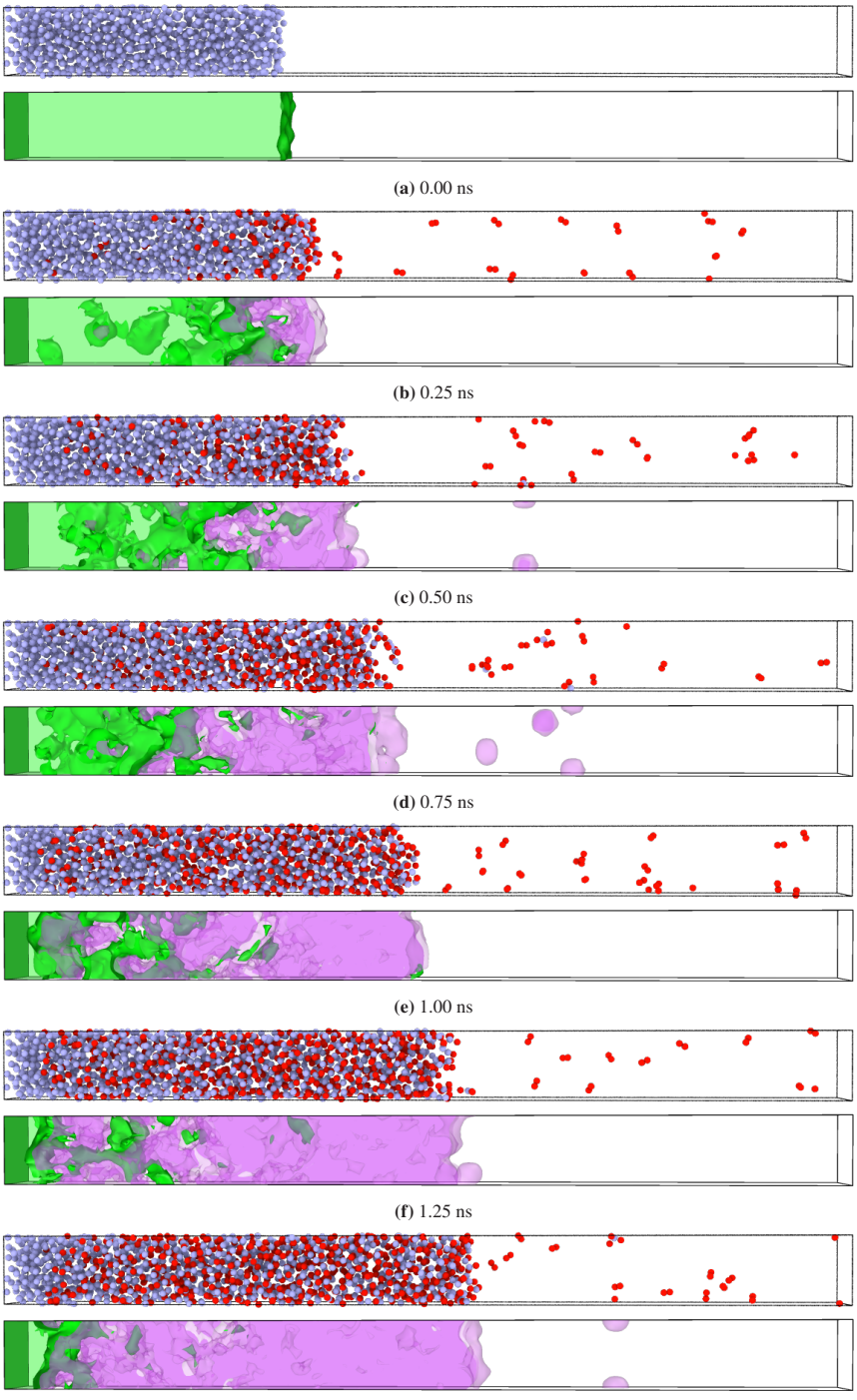

(a) 0.00 ns

(b) 0.25 ns

(c) 0.50 ns

(d) 0.75 ns

(e) 1.00 ns

(f) 1.25 ns

(g) 1.50 ns

Figure 11.9: 3000 K

List of Figures

1.1 Principle of a metal fuel cycle for energy storage and conversion based on iron. Energy is released through the oxidation of iron particles, and the generated heat can be used directly or converted into electricity. The energy carrier is regenerated via reduction with hydrogen produced by water electrolysis or other CO_2-free energy sources. The reduced particles are stored for subsequent use, thereby closing the cycle.[8] 2

2.1 Schematic illustration of the construction of the plane-wave basis set; $\vec{a_1}$ and $\vec{a_1}$ are Bravais-lattice vectors, $\vec{T}$ is a translation vector, and $\vec{b_1}$ and $\vec{b_2}$ are reciprocal-lattice vectors. 19

2.2 Illustration of the pseudopotential concept. The smooth pseudopotential is shown by the red solid line, while the Coulomb potential is shown by the blue dashed line. 21

2.3 Construction of the all-electron wave function within the PAW framework according to Eq. 2.14. 22

2.4 Schematic representation of the exchange–correlation hole 25

2.5 Schematic illustration of the local density approximation. 28

2.6 The difference between the two Monte Carlo methods. The illustration highlights the different goals of these two approaches: one for studying thermodynamic properties, the other for kinetic properties. 35

2.7 Schematic illustrations of the velocity autocorrelation function (VACF) and the corresponding vibrational density of states (VDOS) for the three states of matter: solid, liquid, and gas. 44

3.1 Calculation of the Gibbs free energy of bcc iron within the quasi-harmonic approximation (QHA). The blue lines represent the Helmholtz free energy over the temperature range from 0 to 1600 K in steps of 100 K, while the red line represents the Gibbs free energy obtained from the relation $p = -\left(\frac{dF}{dV}\right)_T$ where p is the pressure under consideration, F is the Helmholtz free energy, and V is the volume. 49

3.2 Thermodynamic properties of bcc iron: heat capacity calculated within with harmonic approximation (HA), quasi-harmonic approximation (QHA), and QHA including magnetic heat capacity computed with Eq. 3.4. The Gibbs free energy and heat capacity are compared to the experimental data (NIST).[136] 50
3.3 Calculated phonon band structure of bcc iron (red lines) compared to experimental data at 300 K (blue dots)[38]. For comparison, the computed data are presented for a volume corresponding to 300 K. 51
3.4 Thermodynamic properties of FeO. The red lines denote calculated data. The blue lines correspond to experimental NIST data.[136] 52
3.5 Thermodynamic properties of $\mathrm{Fe_3O_4}$. The red lines denote calculated data. The blue lines correspond to experimental NIST data.[136] 53
3.6 Thermodynamic properties of $\mathrm{Fe_2O_3}$. The red lines denote calculated data. The blue lines correspond to experimental NIST data.[136] 54
3.7 Gibbs free energy of formation of iron and iron oxides at oxidizing 3.7a and reducing 3.7b conditions. The graph shows the stability regions of the crystals studied. The dotted line indicates the region where the disproportionation reaction $4\mathrm{FeO} = \mathrm{Fe_3O_4} + \mathrm{Fe}$ proceeds, meaning that any FeO formed decomposes into $\mathrm{Fe_3O_4}$ and Fe. 55
3.8 Phase diagram of the Fe-O system representing the oxidation process. The branch of lines shaded with a gradient from green to yellow corresponds to the chemical potential of iron at the respective temperatures, ranging from the lowest (300 K, green) to the highest (1600 K, yellow). The other branch represents the chemical potential of oxygen over the same temperature range (300 K – purple, 1600 K – yellow). The graph shows the ranges over which chemical potentials vary for specific phases, taking into account the interfaces between adjacent phases. The X-axis represents some spatial variable, such as the radius of a spherical particle. 56
3.9 Phase diagram of the Fe-O system representing the oxidation process. The branch of lines shaded with a gradient from green to yellow corresponds to the chemical potential of iron at the respective temperatures, ranging from the lowest (300 K, green) to the highest (1600 K, yellow). The other branch represents the chemical potential of oxygen over the same temperature range (300 K – purple, 1600 K – yellow). The graph shows the ranges over which chemical potentials vary for specific phases, taking into account the interfaces between adjacent phases. As an example, the data are shown for a partial-pressure ratio of water to hydrogen of 10^{-4}. The X-axis represents some spatial variable, such as the radius of a spherical particle. 57

3.10 Schematic representation of the surface reduction process. The pink hexagons represent iron oxides, and the purple pentagons represent iron. It can be seen that the reduced iron is forced to form domains, as the overall particle size must decrease. For this reason, a fully formed particle with a sufficiently rapid reduction rate will always be porous. 59
4.1 Vacancy concentration of oxygen and iron as a function of chemical potential. The branches of lines shaded with a gradient from green to yellow and from purple to yellow correspond to the vacancy concentration at the respective temperatures, ranging from the lowest (600 K, green or purple) to the highest (1600 K, yellow). $\mathrm{Fe-Tet}$ denotes iron atom at the tetrahedral site and $\mathrm{Fe-Oct}$ represents iron atom located at the octahedral sites. The chemical potentials correspond to the oxidizing conditions illustrated in Fig. 3.8. The partial pressure of oxygen is 1 atm. 63
4.2 Algorithm of KMC code. In the first step, the initial geometry is generated and a nearest-neighbor list is constructed for each atom, thereby defining the set of possible migration pathways. In the second step, vacancies are distributed throughout the structure. Next, at the third step, a cumulative rate function is assembled and the event to be executed at the current step is selected stochastically. In the fourth step, the geometry is updated, after which steps 3 and 4 are repeated for a number of iterations equal to the prescribed number of KMC steps. 66
4.3 Comparison of the calculated iron diffusion coefficients with experimental data (open circles).[139] The figure shows the calculated iron diffusion coefficients as a function of vacancy concentration in FeO at constant temperatures and as a function of temperature for FeO, $\mathrm{Fe_3O_4}$, and $\mathrm{Fe_2O_3}$ at constant vacancy concentrations. 69
4.4 Temperature dependence of the diffusion coefficients. The calculations account for the vacancy concentration evaluated at the mean chemical potential of the corresponding species in the oxide. 71
4.5 Rational rate constants for iron-oxide formation as a function of temperature computed with Wagner's theory. The results are compared with the reference data.[139] 72
4.6 Mechanism of oxidation reaction. Oxygen adsorbs on the $\mathrm{Fe_2O_3}$ surface, after which the molecule dissociates, and atomic oxygen migrates into the bulk via oxygen vacancies. In contrast, in bcc iron, the chemical potential of iron is higher, which drives a flux of iron atoms. These atoms migrate through the FeO and $\mathrm{Fe_3O_4}$ layers via iron vacancies toward the $\mathrm{Fe_3O_4/Fe_2O_3}$ interface, where oxidation proceeds. 73

4.7 Mechanism of surface reduction reaction. Molecular hydrogen adsorbs on the bcc iron surface and subsequently dissociates. The high chemical potential of iron in the bcc phase induces a flux toward Fe_2O_3, causing iron atoms to migrate inward toward the Fe_3O_4/Fe_2O_3 boundary and thereby reduce Fe_2O_3 to Fe_3O_4. At the same time, iron migration within FeO releases oxygen, which diffuses from the oxide toward the gas phase, again driven by chemical-potential gradients. At the Fe/gas interface, water molecules form and then desorb into the gas phase. 73
5.1 The slab of the 110 iron surface with an adsorbed hydrogen atom. Atoms frozen from relaxation are colored blue. 76
5.2 Adsorption sites on (110) surface of bcc iron: th – three-fold hollow, sb – short bridge, lb - long bridge. 76
5.3 The adsorption energy profiles for hydrogen and oxygen on (110) surface of bcc iron: th (three fold hollow) – lb (long bridge) – th – sh (short bridge) – th. 77
5.4 The diffusion sites of hydrogen and oxygen in bcc iron: O – octahedral, T1 and T2 – tetrahedral, S – saddle point. 78
5.5 The diffusion energy profile for hydrogen (blue): tetrahedral site (T1) – saddle point (S) – tetrahedral site (T2); and oxygen (red): octahedral site (O1) – tetrahedral site (T) – octahedral site (O2). 79
5.6 Dependence of the adsorption energy of an iron atom on the coordination number. For each data point, the crystallographic plane from which an atom was eliminated (red) or to which an atom was added (blue) is indicated. The reference state was defined as a hexaquairon(II) ion ($Fe^{2+}(H_2O)$), together with the intact slab and water molecules. 79
5.7 Dependence of the adsorption energy of an iron atom on the generalized coordination number. For each data point, the crystallographic plane from which an atom was eliminated (red) or to which an atom was added (blue) is indicated. The reference state was defined as a hexaquairon(II) ion ($Fe^{2+}(H_2O)$), together with the intact slab and water molecules. 80
6.1 Gibbs free energy diagram of the reduction of the (0001) Fe_2O_3 surface at 673 K and hydrogen pressure of 1 atm with Fe–O–Fe termination. The reference system consists of a clean slab and a hydrogen molecule in the gas phase. Iron atoms are shown in purple, oxygen atoms in red, and hydrogen atoms in pale pink. The final state corresponds to a slab with one oxygen atom removed and a water molecule in the gas phase. Intermediate configurations and transition states are also schematically depicted in the figure. 85

6.2 Gibbs free energy diagram of the reduction of the (0001) Fe_2O_3 surface for the set of temperatures ranging from 673 K to 973 K. The reference system consists of a clean slab and a hydrogen molecule in the gas phase. 86
6.3 Gibbs free energy diagram for the hydrogen and water absorption in a hematite pore. Each state on the diagram (plateau) is accompanied by a schematic representation that qualitatively reflects the key features of the corresponding atomic configuration. Iron atoms are shown in purple, oxygen atoms in red, and hydrogen atoms in pale pink. The reference system consists of a bulk and a hydrogen molecule in the gas phase. . . . 87
6.4 Gibbs free energy diagram for the hydrogen and water absorption in a hematite pore at the temperature range from 673 K to 973 K. 88
7.1 Evolution of the average magnetic moment during the DFT-MD simulation of fcc iron at 1600 K in NVT ensemble. The average value along the trajectory is marked with a red line and is approximately equal to zero. 93
7.2 Evolution of the average absolute value of the magnetic moment during the DFT-MD simulation of fcc iron at 1600 K in NVT ensemble. 94
7.3 Calculation of the dependence of pressure on density at constant temperature of 2050 K. Each point corresponds to an independent DFT-MD simulation in NVT ensemble, from which the density and the mean pressure are extracted in order to determine the density at 1 atm. 95
7.4 Density at 1 atm and 2050 K as a function of composition. The calculated data (QMD, blue circles) are compared with the experimental values (purple stars).[146,147] 96
7.5 Accuracy of energy and force prediction using MLIP for training and validation datasets. The color bar on the right encodes $\log_{10}$ of the number of configurations in each bin, i.e., the color corresponds to $10^{(\text{colorbar value})}$ configurations. 98
7.6 Mixing enthalpy of the liquid Fe–O system relative to the corresponding compound at 1 atm and temperatures from 2000 to 3000 K. Data were obtained from molecular dynamics simulations of a 4000-atom system. 99
7.7 Gibbs free energy of the liquid Fe–O system relative to the corresponding compound at 1 atm and temperatures from 2000 to 3000 K. Data were obtained from molecular dynamics simulations of a 4000-atom system, with entropy evaluated using the two-phase thermodynamic (2PT) approach. 100

7.8 Binodal and spinodal curves in the iron–oxygen system obtained for temperatures in the range from 2000 to 3000 K. The binodal was determined using the common-tangent method, whereas the spinodal was evaluated using the thermodynamic stability criterion $(\partial^2 G_{mix}/\partial x_{\mathrm{O}}^2)_{T,P} > 0$, with the spinodal defined by $(\partial^2 G_{mix}/\partial x_{\mathrm{O}}^2)_{T,P} = 0$, where G_{mix} is the mixing Gibbs free energy and x_{O} is the oxygen mole fraction. The required second derivative was obtained via Gaussian-process regression of $G_{mix}(x_{\mathrm{O}})$. 101
7.9 Diffusion coefficients of iron and oxygen for the liquid Fe–O system as functions of compound and temperature. 102
7.10 Viscosity of the Fe–O system as functions of compound and temperature. 103
7.11 Thermal conductivity of the Fe–O system as functions of compound and temperature. 103
7.12 Determination of immiscibility gap. After 1.25 ns of molecular dynamics simulation in the NpT ensemble, the system reaches equilibrium. In the equilibrated configurations, the interface between liquid iron and iron oxide is clearly visible. The compositions of the respective phases can be determined from the MD trajectory. 104
7.13 Phase diagramm of the Fe–O system. Molecular dynamics results are shown as purple points with standard deviation. The data were interpolated up to 3000 K using Gaussian process regression. The left and right branches correspond to L1 and L2, respectively. The shaded region represents twice the standard deviation. 105
8.1 Molecular dynamics simulation of iron-slab oxidation by oxygen molecules at 2000 K. The figure shows snapshots taken 0.5, 1.0, and 1.5 ns after the start of the simulation. Iron atoms are coloured purple and oxygen atoms red. Under the simulation conditions, the oxygen volumetric flux is approximately 15 km/s. The right panel shows profiles of the oxygen atomic fraction along the z coordinate of the simulation cell. 112
8.2 Profiles of the oxygen atomic fraction along the z coordinate of the simulation cell at 2000 K and 3000 K. 113
8.3 Simulation cell of the iron nanoparticle (left) and the iron oxide (right) obtained during oxidation in molecular-dynamics simulations. 113

8.4 Consumption of oxygen atoms during the MD simulation of the oxidation of an iron slab. Three regions are identified schematically: the blue region corresponds to the adsorption stage, during which molecular oxygen dissociates and progressively covers the surface of the liquid iron nanoparticle. This is followed by the orange region, where rapid growth of the oxide-rich L_2 phase occurs. The process then slows down in the green region. It is assumed that the curve shown in the figure reaches a plateau upon complete oxidation. The figure illustrates that the formation of the oxide phase inhibits further oxidation. 114
8.5 Oxidation mechanism of a liquid iron nanoparticle. First, molecular oxygen adsorbs on the particle surface and dissociates 8.5a. Subsequently, an oxide layer forms as oxygen atoms become incorporated into the iron layer, while adsorption and dissociation continue 8.5b. Next, an iron-oxide droplet develops and, due to the large viscosity contrast, migrates rapidly along the particle surface, promoting the growth of the oxide phase 8.5c. In the final stage, a liquid iron droplet remains and migrates within the newly formed iron-oxide nanoparticle 8.5d. 115
9.1 SCALMS concept. The method uses aluminium oxide as the support. The top panel shows a schematic of the catalyst preparation procedure, while the bottom panel illustrates the propane dehydrogenation (PDH) to propene. Indium atoms are shown in gold, oxygen atoms in red, the catalytically active atom in blue, the hydrocarbon species in brown, and hydrogen atoms in pale pink. 118
9.2 Snapshot of simulation cell with Pt atoms (blue) and In atoms (gold). 119
9.3 Training progress of the In_{160} system with BEEF (Bayesian error estimation of forces), CTIFOF (current value of threshold criterion), and ERR (root mean squared error of forces). 120
9.4 Training progress of the $In_{158}Pt_2$ system with BEEF (Bayesian error estimation of forces), CTIFOF (current value of threshold criterion), and ERR (root mean squared error of forces). 121
9.5 The density distribution function of particle detection relative to the direction orthogonal to the plane of the liquid surface for $In_{158}Pt_2$ 122
9.6 The density distribution function of particle detection relative to the direction orthogonal to the plane of the liquid surface for $In_{158}Pd_2$ 123
9.7 Coordination number of Pt atoms in $In_{158}Pt_2$ calculated during the MD simulation (trajectory length: 2 ns, snapshots each 500 fs, 1 occasion per (approx.) 42.25 ps). 124

11.1 Phase diagrams under oxidising (top) and reducing (bottom) conditions in temperature-partial pressure coordinates of the gas components. Red indicates the stability region of Fe_2O_3, blue that of Fe_3O_4, green that of FeO, and gray that of bcc iron. 131
11.2 Migration pathways of iron atoms in Fe_3O_4. Sites are designated using Wyckoff positions: Octahedral site Fe_{oct} - 16d and tetrahedral site Fe_{tet} - 8a. 132
11.3 Molecular dynamics simulation of the oxidation of liquid iron nanoparticle 132
11.4 2000 K 133
11.5 2200 K 134
11.6 2400 K 135
11.7 2600 K 136
11.8 2800 K 137
11.9 3000 K 138

List of Tables

3.1 First-principles calculation parameters for iron and its oxides. 48
4.1 Input data for the KMC simulations calculated within PBE+U approach. 68
4.2 Results of the KMC simulations. The calculated values of diffusion coefficients were fitted using the Arrhenius equation, and the corresponding parameters are listed in the table. 70
7.1 Comparison of average pressure for systems of different parameters. Pressure is given in kbar. 93
7.2 CPUh comparison for systems with different parameters. The simulation with 250 atoms and 8 k-points is performed for 1800 steps. 93
7.3 Sizes and root mean square deviations of the potential on the training and validation datasets. 97
8.1 Mass and thermal accommodation coefficients. 111

List of Publications

Journal articles

[1] Lukas Braun, Jonas Spielmann, Dmitry E Doronkin, Carola Kuhn, Aleksandr Maliugin, Dmitry I Sharapa, Isabel Huck, Jianing Bao, Steffen Tischer, Felix Studt, et al. Following the structural changes of iron oxides during reduction under transient conditions. *ChemSusChem*, 17(24):e202401045, 2024.

[2] Aleksandr Maliugin, Dmitry I. Sharapa, and Felix Studt. Liquid-state oxidation processes in the iron–oxygen system. In preparation, 2026.

[3] Aleksandr Maliugin, Dmitry I. Sharapa, and Felix Studt. Molecular dynamics study of the liquid fe-o system using a machine learning interatomic potential. In preparation, 2026.

[4] Aleksandr Maliugin, Dmitry I. Sharapa, and Felix Studt. Theoretical study on iron oxidation and reduction of iron oxide. In preparation, 2026.

[5] Moritz Wolf, Thomas Gradl, Shaine Raseale, Aleksandr Maliugin, Narayanan Raman, Patrick Schühle, Nicola Taccardi, Michael Claeys, Dmitry I Sharapa, Felix Studt, et al. In-pt supported catalytically active liquid metal solutions for propane dehydrogenation–role of surface acidity of support. *ChemCatChem*, page e202402096, 2025.

Conference contributions

[1] Aleksandr Maliugin, Dmitry I. Sharapa, and Felix Studt. Theoretical investigation of iron oxidation and reduction of iron oxides. In *59th Symposium on Theoretical Chemistry (STC 2023)*, Zurich, Switzerland, September 2023. ETH Zurich. URL `https://stc2023.ch/`. September 11–14, 2023.

[2] Aleksandr Maliugin, Dmitry I. Sharapa, and Felix Studt. Theoretical investigation of iron oxidation and reduction of iron oxides. In *57. Jahrestreffen Deutscher Katalytiker*, Weimar,

Germany, March 2024. DECHEMA e.V. URL https://dechema.de/en/katalytiker2024.html. March 13–15, 2024; congress centrum weimarhalle.

[3] Aleksandr Maliugin, Dmitry I. Sharapa, and Felix Studt. Molecular dynamics study of the liquid fe-o system using a machine learning interatomic potential. In *Psi-k 2025 Conference*, Lausanne, Switzerland, August 2025. Psi-k Network. URL https://www.psik2025.net/.

[4] Aleksandr Maliugin, Dmitry I. Sharapa, and Felix Studt. Molecular dynamics study of the liquid fe-o system using a machine learning interatomic potential. In *VASP Workshop 2025*, Rennes, France, June 2025. VASP Workshop (Sciencesconf). URL https://vasp.sciencesconf.org/. June 30–July 4, 2025; ENSCR, Rennes.

Bibliography

[1] United Nations Framework Convention on Climate Change. Paris agreement, 2015. Adopted at the 21st Conference of the Parties (COP 21).

[2] Mark A Delucchi and Mark Z Jacobson. Providing all global energy with wind, water, and solar power, part ii: Reliability, system and transmission costs, and policies. *Energy policy*, 39(3):1170–1190, 2011.

[3] Yushu Sun, Zhenxing Zhao, Min Yang, Dongqiang Jia, Wei Pei, and Bin Xu. Overview of energy storage in renewable energy power fluctuation mitigation. *CSEE Journal of power and energy systems*, 6(1):160–173, 2019.

[4] Ingo Stadler and Michael Sterner. Urban energy storage and sector coupling. In *Urban Energy Transition*, pages 225–244. Elsevier, 2018.

[5] Philippe Julien and Jeffrey M Bergthorson. Enabling the metal fuel economy: green recycling of metal fuels. *Sustainable Energy & Fuels*, 1(3):615–625, 2017.

[6] Jeffrey M Bergthorson. Recyclable metal fuels for clean and compact zero-carbon power. *Progress in Energy and Combustion Science*, 68:169–196, 2018.

[7] Etienne Rivard, Michel Trudeau, and Karim Zaghib. Hydrogen storage for mobility: a review. *Materials*, 12(12):1973, 2019.

[8] Paulo Debiagi, Rodolfo Cavaliere Rocha, Arne Scholtissek, Johannes Janicka, and Christian Hasse. Iron as a sustainable chemical carrier of renewable energy: Analysis of opportunities and challenges for retrofitting coal-fired power plants. *Renewable and Sustainable Energy Reviews*, 165:112579, 2022.

[9] CJM Hessels, AHJ Smeets, Giulia Finotello, Niels G Deen, and Yali Tang. Sintering behavior of combusted iron powder in a packed bed reactor with nitrogen and hydrogen. *Particuology*, 83:8–17, 2023.

[10] Sofia D Angeli, Sabrina Gossler, Sven Lichtenberg, Gilles Kass, Anand Kumar Agrawal, Miriam Valerius, Klaus Peter Kinzel, and Olaf Deutschmann. Reduction of co2 emission from

off-gases of steel industry by dry reforming of methane. *Angewandte Chemie International Edition*, 60(21):11852–11857, 2021.

[11] Philipp Blanck, Gilles Kass, Klaus Peter Kinzel, and Olaf Deutschmann. Dry reforming of steelworks off-gases in a pilot plant integrated into a steel mill: influence of operating parameters. *Energy Advances*, 3(1):123–130, 2024.

[12] Norbert Auner and Sven Holl. Silicon as energy carrier—facts and perspectives. *Energy*, 31(10-11):1395–1402, 2006.

[13] Linda Barelli, Manuel Baumann, Gianni Bidini, Panfilo A Ottaviano, Rebekka V Schneider, Stefano Passerini, and Lorenzo Trombetti. Reactive metals as energy storage and carrier media: use of aluminum for power generation in fuel cell-based power plants. *Energy Technology*, 8(9):2000233, 2020.

[14] Luc Dirven, Niels G Deen, and Michael Golombok. Dense energy carrier assessment of four combustible metal powders. *Sustainable Energy Technologies and Assessments*, 30:52–58, 2018.

[15] Jeffrey M Bergthorson, S Goroshin, MJ Soo, P Julien, J Palecka, DL Frost, and DJ Jarvis. Direct combustion of recyclable metal fuels for zero-carbon heat and power. *Applied Energy*, 160:368–382, 2015.

[16] Thomas A Brzustowski and Irvin Glassman. Vapor-phase diffusion flames in the combustion of magnesium and aluminum: I. analytical developments. In *Progress in Astronautics and Rocketry*, volume 15, pages 75–115. Elsevier, 1964.

[17] Dongsheng Wen. Nanofuel as a potential secondary energy carrier. *Energy & Environmental Science*, 3(5):591–600, 2010.

[18] Russell A Ogle. *Dust explosion dynamics*. Butterworth-Heinemann, 2016.

[19] Jochem De Kwant, Robert Hekkenberg, Apostolos Souflis-Rigas, and Austin A Kana. Exploring the potential of iron powder as fuel on the design and performance of container ships. *International Shipbuilding Progress*, 70(1):3–28, 2023.

[20] Charalampos Mandilas, George Karagiannakis, Athanasios G Konstandopoulos, Carlo Beatrice, Maurizio Lazzaro, Gabriele Di Blasio, Santiago Molina, Jose V Pastor, and Antonio Gil. Study of oxidation and combustion characteristics of iron nanoparticles under idealized and enginelike conditions. *Energy & Fuels*, 30(5):4318–4330, 2016.

[21] Kasper T Møller, Torben R Jensen, Etsuo Akiba, and Hai-wen Li. Hydrogen-a sustainable energy carrier. *Progress in natural science: Materials International*, 27(1):34–40, 2017.

[22] Yongliang Li, Haisheng Chen, Xinjing Zhang, Chunqing Tan, and Yulong Ding. Renewable energy carriers: Hydrogen or liquid air/nitrogen? *Applied Thermal Engineering*, 30(14-15): 1985–1990, 2010.

[23] Calin Zamfirescu and IJJoPS Dincer. Using ammonia as a sustainable fuel. *Journal of Power Sources*, 185(1):459–465, 2008.

[24] Johannes Janicka, Paulo Debiagi, Arne Scholtissek, Andreas Dreizler, Bernd Epple, Reiner Pawellek, Alexander Maltsev, and Christian Hasse. The potential of retrofitting existing coal power plants: A case study for operation with green iron. *Applied Energy*, 339:120950, 2023.

[25] Carola Kuhn, Anna Knapp, Max P Deutschmann, Jonas Spielmann, Steffen Tischer, Ulrike I Kramm, Hermann Nirschl, and Olaf Deutschmann. Iron as recyclable metal fuel: Unraveling oxidation behavior and cyclization effects through thermogravimetric analysis, wide-angle x-ray scattering and mössbauer spectroscopy. *ChemSusChem*, 17(15):e202400351, 2024.

[26] Raffaele Cucciniello and Daniele Cespi. Recycling within the chemical industry: The circular economy era. *Recycling*, 3(2):22, 2018.

[27] Tom Keijer, Vincent Bakker, and J Chris Slootweg. Circular chemistry to enable a circular economy. *Nature chemistry*, 11(3):190–195, 2019.

[28] Manfred Fischedick, Joachim Marzinkowski, Petra Winzer, and Max Weigel. Techno-economic evaluation of innovative steel production technologies. *Journal of Cleaner Production*, 84:563–580, 2014.

[29] Valentin Vogl, Max Åhman, and Lars J Nilsson. Assessment of hydrogen direct reduction for fossil-free steelmaking. *Journal of cleaner production*, 203:736–745, 2018.

[30] Abhinav Bhaskar, Mohsen Assadi, and Homam Nikpey Somehsaraei. Decarbonization of the iron and steel industry with direct reduction of iron ore with green hydrogen. *Energies*, 13(3):758, 2020.

[31] Quentin Fradet, Mohammed Liaket Ali, and Uwe Riedel. Development of a porous solid model for the direct reduction of iron ore pellets. *steel research international*, 93(12):2200042, 2022.

[32] Max Weigel, Manfred Fischedick, Joachim Marzinkowski, and Petra Winzer. Multicriteria analysis of primary steelmaking technologies. *Journal of cleaner production*, 112:1064–1076, 2016.

[33] Katharina Rechberger, Andreas Spanlang, Amaia Sasiain Conde, Hermann Wolfmeir, and Christopher Harris. Green hydrogen-based direct reduction for low-carbon steelmaking. *steel research international*, 91(11):2000110, 2020.

[34] Jue Tang, Man-sheng Chu, Feng Li, Cong Feng, Zheng-gen Liu, and Yu-sheng Zhou. Development and progress on hydrogen metallurgy. *International Journal of Minerals, Metallurgy and Materials*, 27(6):713–723, 2020.

[35] RR Wang, YQ Zhao, Alexander Babich, Dieter Senk, and XY Fan. Hydrogen direct reduction (h-dr) in steel industry—an overview of challenges and opportunities. *Journal of Cleaner Production*, 329:129797, 2021.

[36] Lauri Holappa. A general vision for reduction of energy consumption and co2 emissions from the steel industry. *Metals*, 10(9):1117, 2020.

[37] Zbigniew Stanislaw Basinski, William Hume-Rothery, and AL Sutton. The lattice expansion of iron. *Proceedings of the Royal Society of London. Series A. Mathematical and Physical Sciences*, 229(1179):459–467, 1955.

[38] Matthew Heine, Olle Hellman, and David Broido. Effect of thermal lattice and magnetic disorder on phonons in bcc fe: A first-principles study. *Physical Review B*, 100(10):104304, 2019.

[39] Chao-Sheng Lian, Jian-Tao Wang, and Changfeng Chen. Ab initio study of the anharmonic lattice dynamics of iron at the γ-δ phase transition. *Physical Review B*, 92(18):184110, 2015.

[40] Ivan Leonov, AI Poteryaev, VI Anisimov, and Dieter Vollhardt. Calculated phonon spectra of paramagnetic iron at the α-γ phase transition. *Physical Review B—Condensed Matter and Materials Physics*, 85(2):020401, 2012.

[41] Fritz Körmann, Alexey Dick, Blazej Grabowski, B Hallstedt, T Hickel, and J Neugebauer. Free energy of bcc iron: Integrated ab initio derivation of vibrational, electronic, and magnetic contributions. *Physical Review B—Condensed Matter and Materials Physics*, 78(3):033102, 2008.

[42] L Mauger, MS Lucas, JA Muñoz, SJ Tracy, M Kresch, Yuming Xiao, Paul Chow, and B Fultz. Nonharmonic phonons in α-iron at high temperatures. *Physical Review B*, 90(6): 064303, 2014.

[43] IK Razumov, Yu N Gornostyrev, and MI Katsnelson. Towards the ab initio based theory of phase transformations in iron and steel. *Physics of Metals and Metallography*, 118(4): 362–388, 2017.

[44] Jindřich Kolorenč and Lubos Mitas. Quantum monte carlo calculations of structural properties of feo under pressure. *Physical review letters*, 101(18):185502, 2008.

[45] Zhen Zhang, Yang Sun, and Renata M Wentzcovitch. Pbe-gga predicts the b8 b2 phase boundary of feo at earth's core conditions. *Proceedings of the National Academy of Sciences*, 120(28):e2304726120, 2023.

[46] Kenji Ohta, Ronald E Cohen, Kei Hirose, Kristjan Haule, Katsuya Shimizu, and Yasuo Ohishi. Experimental and theoretical evidence for pressure-induced metallization in feo with rocksalt-type structure. *Physical review letters*, 108(2):026403, 2012.

[47] Motohiko Murakami, Kei Hirose, Shigeaki Ono, Taku Tsuchiya, Maiko Isshiki, and Tetsu Watanuki. High pressure and high temperature phase transitions of feo. *Physics of the earth and planetary interiors*, 146(1-2):273–282, 2004.

[48] Svein Stolen, Ronny Glockner, Fredrik Gronvold, Tooru Atake, and Satoru Izumisawa. Heat capacity and thermodynamic properties of nearly stoichiometric wustite from 13 to 450 k. *American Mineralogist*, 81(7-8):973–981, 1996.

[49] Robina Ashraf, Tariq Mahmood, Saira Riaz, and Shahzad Naseem. Study of the structural and electronic properties of feo at the lda and gga level. *Chinese journal of physics*, 55(4): 1135–1141, 2017.

[50] N Yahi, Yahia Azzaz, Mohammed Ameri, M Benouis, D Bensaid, Omar Arbouche, M Yamani, and N Moulay. Anti-ferromagnetic structure and magnetic properties of feo with gga+ u+ soc study. *Physics of the Solid State*, 62(3):472–479, 2020.

[51] Jingping Dong, Xun-Wang Yan, and Fengjie Ma. Strongly correlated electronic properties of feo studied by the scan+ u functional. *The Journal of Physical Chemistry C*, 127(11): 5513–5518, 2023.

[52] A Schrön, Claudia Rödl, and Friedhelm Bechstedt. Crystalline and magnetic anisotropy of the 3 d-transition metal monoxides mno, feo, coo, and nio. *Physical Review B—Condensed Matter and Materials Physics*, 86(11):115134, 2012.

[53] Roland Gillen and John Robertson. Accurate screened exchange band structures for the transition metal monoxides mno, feo, coo and nio. *Journal of Physics: Condensed Matter*, 25(16):165502, 2013.

[54] C Rödl, F Fuchs, J Furthmüller, and F Bechstedt. Quasiparticle band structures of the antiferromagnetic transition-metal oxides mno, feo, coo, and nio. *Physical Review B—Condensed Matter and Materials Physics*, 79(23):235114, 2009.

[55] Iván Bernal-Villamil and Silvia Gallego. Electronic structure and polaronic charge distributions of fe vacancy clusters in fe _{$1 - x$} o. *arXiv preprint arXiv:1411.5511*, 2014.

[56] Urszula D Wdowik, Przemysław Piekarz, Krzysztof Parlinski, Andrzej M Oleś, and Józef Korecki. Strong effects of cation vacancies on the electronic and dynamical properties of feo. *Physical Review B—Condensed Matter and Materials Physics*, 87(12):121106, 2013.

[57] Nikita A Fominykh, Vsevolod P Nikolskiy, and Vladimir V Stegailov. Atomistic model of an oxide film in contact with a liquid metal coolant: defects concentrations and chemical potentials of dissolved fe–o. *Computational Materials Science*, 220:112061, 2023.

[58] Zeng Liang, Kejiang Li, Jianliang Zhang, and Alberto N Conejo. Insights into defect cluster formation in non-stoichiometric wustite (fe1- x o) at elevated temperatures: accurate force field from deep learning. *npj Computational Materials*, 11(1):32, 2025.

[59] Kurt E Sickafus, John M Wills, and Norman W Grimes. Structure of spinel. *Journal of the American Ceramic Society*, 82(12):3279–3292, 1999.

[60] EJWhttps Verwey. Electronic conduction of magnetite (fe3o4) and its transition point at low temperatures. *Nature*, 144(3642):327–328, 1939.

[61] Rochelle M Cornell and Udo Schwertmann. *The iron oxides: structure, properties, reactions, occurrences and uses*. John Wiley & Sons, 2003.

[62] Zdzislawa Szotek, Walter M Temmerman, Axel Svane, Leon Petit, George Malcolm Stocks, and H Winter. Ab initio study of charge order in fe 3 o 4. *Physical Review B*, 68(5):054415, 2003.

[63] Hongsheng Liu and Cristiana Di Valentin. Band gap in magnetite above verwey temperature induced by symmetry breaking. *The Journal of Physical Chemistry C*, 121(46):25736–25742, 2017.

[64] Junghyun Noh, Osman I Osman, Saadullah G Aziz, Paul Winget, and Jean-Luc Brédas. A density functional theory investigation of the electronic structure and spin moments of magnetite. *Science and technology of advanced materials*, 15(4):044202, 2014.

[65] A Roldan, David Santos-Carballal, and Nora H de Leeuw. A comparative dft study of the mechanical and electronic properties of greigite fe3s4 and magnetite fe3o4. *The Journal of Chemical Physics*, 138(20), 2013.

[66] David Santos-Carballal, Alberto Roldan, Ricardo Grau-Crespo, and Nora H de Leeuw. A dft study of the structures, stabilities and redox behaviour of the major surfaces of magnetite fe 3 o 4. *Physical Chemistry Chemical Physics*, 16(39):21082–21097, 2014.

[67] Adam Kiejna, Tomasz Ossowski, and Tomasz Pabisiak. Surface properties of the clean and au/pd covered fe 3 o 4 (111): Dft and dft+ u study. *Physical Review B—Condensed Matter and Materials Physics*, 85(12):125414, 2012.

[68] Junghyun Noh, Osman I Osman, Saadullah G Aziz, Paul Winget, and Jean-Luc Bredas. Magnetite fe3o4 (111) surfaces: impact of defects on structure, stability, and electronic properties. *Chemistry of Materials*, 27(17):5856–5867, 2015.

[69] Mine Konuk, Kai Sellschopp, Gregor B Vonbun-Feldbauer, and Robert H Meißner. Modeling charge redistribution at magnetite interfaces in empirical force fields. *The journal of physical chemistry C*, 125(8):4794–4805, 2021.

[70] Diego Tozini, Mariano Forti, Pablo Gargano, Paula R Alonso, and GH Rubiolo. Charge difference calculation in fe/fe3o4 interfaces from dft results. *Procedia Materials Science*, 9: 612–618, 2015.

[71] Emre Gursoy, Gregor B Vonbun-Feldbauer, and Robert H Meißner. Oxidation-state dynamics and emerging patterns in magnetite. *The Journal of Physical Chemistry Letters*, 14(30): 6800–6807, 2023.

[72] Christopher L Muhich, Victoria J Aston, Ryan M Trottier, Alan W Weimer, and Charles B Musgrave. First-principles analysis of cation diffusion in mixed metal ferrite spinels. *Chemistry of materials*, 28(1):214–226, 2016.

[73] Linus Pauling and Sterling B Hendricks. The crystal structures of hematite and corundum. *Journal of the American Chemical Society*, 47(3):781–790, 1925.

[74] Jung-Fu Lin, John S Tse, Esen E Alp, Jiyong Zhao, Michael Lerche, Wolfgang Sturhahn, Yuming Xiao, and Paul Chow. Phonon density of states of fe 2 o 3 across high-pressure structural and electronic transitions. *Physical Review B—Condensed Matter and Materials Physics*, 84(6):064424, 2011.

[75] G Rollmann, Adrian Rohrbach, Peter Entel, and Juergen Hafner. First-principles calculation of the structure and magnetic phases of hematite. *Physical Review B*, 69(16):165107, 2004.

[76] Zachary D Pozun and Graeme Henkelman. Hybrid density functional theory band structure engineering in hematite. *The Journal of chemical physics*, 134(22), 2011.

[77] Nelson Naveas, Ruth Pulido, Carlo Marini, Jacobo Hernández-Montelongo, and Miguel Manso Silván. First-principles calculations of hematite (α-fe2o3) by self-consistent dft+ u+ v. *Iscience*, 26(2), 2023.

[78] Christian S Ahart, Kevin M Rosso, and Jochen Blumberger. Electron and hole mobilities in bulk hematite from spin-constrained density functional theory. *Journal of the American Chemical Society*, 144(10):4623–4632, 2022.

[79] AH Hill, F Jiao, PG Bruce, A Harrison, W Kockelmann, and C Ritter. Neutron diffraction study of mesoporous and bulk hematite, α-fe2o3. *Chemistry of Materials*, 20(15):4891–4899, 2008.

[80] Richard B Wang and Anders Hellman. Surface terminations of hematite (α-fe2o3) exposed to oxygen, hydrogen, or water: dependence on the density functional theory methodology. *Journal of Physics: Condensed Matter*, 30(27):275002, 2018.

[81] Jiachen Chen, Dmitry I Sharapa, and Philipp N Plessow. Stability of hydroxylated α-fe2o3 (0001) surfaces. *ACS omega*, 9(33):35449–35457, 2024.

[82] Cynthia S Lo, Kunaljeet S Tanwar, Anne M Chaka, and Thomas P Trainor. Density functional theory study of the clean and hydrated hematite (1 1 02) surfaces. *Physical Review B—Condensed Matter and Materials Physics*, 75(7):075425, 2007.

[83] Richard Baochang Wang and Anders Hellman. Hybrid functional study of the electro-oxidation of water on pristine and defective hematite (0001). *The Journal of Physical Chemistry C*, 123(5):2820–2827, 2019.

[84] Pierre Hohenberg and Walter Kohn. Inhomogeneous electron gas. *Physical review*, 136 (3B):B864, 1964.

[85] Walter Kohn and Lu Jeu Sham. Self-consistent equations including exchange and correlation effects. *Physical review*, 140(4A):A1133, 1965.

[86] Felix Bloch. Quantum mechanics of electrons in crystal lattices. *Z. Phys*, 52:555–600, 1928.

[87] Georg Kresse and Jürgen Furthmüller. Efficient iterative schemes for ab initio total-energy calculations using a plane-wave basis set. *Physical review B*, 54(16):11169, 1996.

[88] Peter E Blöchl. Projector augmented-wave method. *Physical review B*, 50(24):17953, 1994.

[89] Wolfram Koch and Max C Holthausen. *A chemist's guide to density functional theory*. John Wiley & Sons, 2015.

[90] June Gunn Lee. *Computational materials science: an introduction*. CRC press, 2016.

[91] RK Nesbet and R Colle. Does an exact local exchange potential exist? *Journal of Mathematical Chemistry*, 26(1):233–242, 1999.

[92] David M Ceperley and Berni J Alder. Ground state of the electron gas by a stochastic method. *Physical review letters*, 45(7):566, 1980.

[93] Seymour H Vosko, Leslie Wilk, and Marwan Nusair. Accurate spin-dependent electron liquid correlation energies for local spin density calculations: a critical analysis. *Canadian Journal of physics*, 58(8):1200–1211, 1980.

[94] John P Perdew and Yue Wang. Accurate and simple analytic representation of the electron-gas correlation energy. *Physical review B*, 45(23):13244, 1992.

[95] Lars Hedin and Bengt I Lundqvist. Explicit local exchange-correlation potentials. *Journal of Physics C: Solid state physics*, 4(14):2064, 1971.

[96] John P Perdew, Kieron Burke, and Matthias Ernzerhof. Generalized gradient approximation made simple. *Physical review letters*, 77(18):3865, 1996.

[97] Elliott H Lieb and Stephen Oxford. Improved lower bound on the indirect coulomb energy. *International Journal of Quantum Chemistry*, 19(3):427–439, 1981.

[98] John P Perdew, Adrienn Ruzsinszky, Gábor I Csonka, Oleg A Vydrov, Gustavo E Scuseria, Lucian A Constantin, Xiaolan Zhou, and Kieron Burke. Restoring the density-gradient expansion for exchange in solids and surfaces. *Physical review letters*, 100(13):136406, 2008.

[99] IG Austin and NF Mott. Metallic and nonmetallic behavior in transition metal oxides: Electron correlation effects in narrow d bands and polarons are discussed. *Science*, 168 (3927):71–77, 1970.

[100] John Hubbard. Electron correlations in narrow energy bands. *Proceedings of the Royal Society of London. Series A. Mathematical and Physical Sciences*, 276(1365):238–257, 1963.

[101] John Hubbard. Electron correlations in narrow energy bands. ii. the degenerate band case. *Proceedings of the Royal Society of London. Series A. Mathematical and Physical Sciences*, 277(1369):237–259, 1964.

[102] John Hubbard. Electron correlations in narrow energy bands iii. an improved solution. *Proceedings of the Royal Society of London. Series A. Mathematical and Physical Sciences*, 281(1386):401–419, 1964.

[103] John Hubbard. Electron correlations in narrow energy bands-iv. the atomic representation. *Proceedings of the Royal Society of London. Series A. Mathematical and Physical Sciences*, 285(1403):542–560, 1965.

[104] John Hubbard. Electron correlations in narrow energy bands v. a perturbation expansion about the atomic limit. *Proceedings of the Royal Society of London. Series A. Mathematical and Physical Sciences*, 296(1444):82–99, 1967.

[105] John Hubbard. Electron correlations in narrow energy bands vi. the connexion with many-body perturbation theory. *Proceedings of the Royal Society of London. Series A. Mathematical and Physical Sciences*, 296(1444):100–112, 1967.

[106] Vladimir I Anisimov, Jan Zaanen, and Ole K Andersen. Band theory and mott insulators: Hubbard u instead of stoner i. *Physical Review B*, 44(3):943, 1991.

[107] Vlasdimir I Anisimov, IV Solovyev, MA Korotin, MT Czyżyk, and GA Sawatzky. Density-functional theory and nio photoemission spectra. *Physical Review B*, 48(23):16929, 1993.

[108] IV Solovyev, PH Dederichs, and VI Anisimov. Corrected atomic limit in the local-density approximation and the electronic structure of d impurities in rb. *Physical Review B*, 50(23): 16861, 1994.

[109] Sergei L Dudarev, Gianluigi A Botton, Sergey Y Savrasov, CJ Humphreys, and Adrian P Sutton. Electron-energy-loss spectra and the structural stability of nickel oxide: An lsda+ u study. *Physical Review B*, 57(3):1505, 1998.

[110] Richard M Martin. *Electronic structure: basic theory and practical methods*. Cambridge university press, 2020.

[111] Daan Frenkel and Berend Smit. *Understanding molecular simulation: from algorithms to applications*. elsevier, 2023.

[112] Martin T Dove. *Introduction to lattice dynamics*. Number 4. Cambridge university press, 1993.

[113] Yvon Le Page and Paul Saxe. Symmetry-general least-squares extraction of elastic data for strained materials from ab initio calculations of stress. *Physical Review B*, 65(10):104104, 2002.

[114] M Gajdoš, Kerstin Hummer, G Kresse, J Furthmüller, and FJPRB Bechstedt. Linear optical properties in the projector-augmented wave methodology. *Physical Review B—Condensed Matter and Materials Physics*, 73(4):045112, 2006.

[115] Xifan Wu, David Vanderbilt, and DR Hamann. Systematic treatment of displacements, strains, and electric fields in density-functional perturbation theory. *Physical Review B—Condensed Matter and Materials Physics*, 72(3):035105, 2005.

[116] Ivan S Novikov, Konstantin Gubaev, Evgeny V Podryabinkin, and Alexander V Shapeev. The mlip package: moment tensor potentials with mpi and active learning. *Machine Learning: Science and Technology*, 2(2):025002, 2020.

[117] Alexander V Shapeev. Moment tensor potentials: A class of systematically improvable interatomic potentials. *Multiscale Modeling & Simulation*, 14(3):1153–1173, 2016.

[118] Alexander Shapeev. Accurate representation of formation energies of crystalline alloys with many components. *Computational Materials Science*, 139:26–30, 2017.

[119] Evgeny V Podryabinkin and Alexander V Shapeev. Active learning of linearly parametrized interatomic potentials. *Computational Materials Science*, 140:171–180, 2017.

[120] Lars Onsager. Reciprocal relations in irreversible processes. i. *Physical review*, 37(4):405, 1931.

[121] Shiang-Tai Lin, Prabal K Maiti, and William A Goddard III. Two-phase thermodynamic model for efficient and accurate absolute entropy of water from molecular dynamics simulations. *The Journal of Physical Chemistry B*, 114(24):8191–8198, 2010.

[122] Min-Hsien Lin and Shiang-Tai Lin. A robust and automated approach for the calculation of absolute entropy from the two-phase thermodynamic model with gaussian memory function. In *Computational Materials, Chemistry, and Biochemistry: From Bold Initiatives to the Last Mile: In Honor of William A. Goddard's Contributions to Science and Engineering*, pages 89–114. Springer, 2021.

[123] Michael P Desjarlais. First-principles calculation of entropy for liquid metals. *Physical Review E*, 88(6):062145, 2013.

[124] Grégory Robert, Philippe Legrand, Philippe Arnault, Nicolas Desbiens, and Jean Clérouin. Simple calculation of ab initio melting curves: Application to aluminum. *Physical Review E*, 91(3):033310, 2015.

[125] Shiang-Tai Lin, Mario Blanco, and William A Goddard III. The two-phase model for calculating thermodynamic properties of liquids from molecular dynamics: Validation for the phase diagram of lennard-jones fluids. *The Journal of chemical physics*, 119(22):11792–11805, 2003.

[126] Georg Kresse and Jürgen Hafner. Ab initio molecular-dynamics simulation of the liquid-metal–amorphous-semiconductor transition in germanium. *Physical Review B*, 49(20):14251, 1994.

[127] Georg Kresse and Jürgen Furthmüller. Efficiency of ab-initio total energy calculations for metals and semiconductors using a plane-wave basis set. *Computational materials science*, 6(1):15–50, 1996.

[128] Georg Kresse and Daniel Joubert. From ultrasoft pseudopotentials to the projector augmented-wave method. *Physical review b*, 59(3):1758, 1999.

[129] Graeme Henkelman, Blas P Uberuaga, and Hannes Jónsson. A climbing image nudged elastic band method for finding saddle points and minimum energy paths. *The Journal of chemical physics*, 113(22):9901–9904, 2000.

[130] Aliaksandr V Krukau, Oleg A Vydrov, Artur F Izmaylov, and Gustavo E Scuseria. Influence of the exchange screening parameter on the performance of screened hybrid functionals. *The Journal of chemical physics*, 125(22), 2006.

[131] Xavier Gonze and Changyol Lee. Dynamical matrices, born effective charges, dielectric permittivity tensors, and interatomic force constants from density-functional perturbation theory. *Physical Review B*, 55(16):10355, 1997.

[132] Atsushi Togo, Laurent Chaput, Terumasa Tadano, and Isao Tanaka. Implementation strategies in phonopy and phono3py. *J. Phys. Condens. Matter*, 35(35):353001, 2023. doi: 10.1088/1361-648X/acd831.

[133] Atsushi Togo. First-principles phonon calculations with phonopy and phono3py. *J. Phys. Soc. Jpn.*, 92(1):012001, 2023. doi: 10.7566/JPSJ.92.012001.

[134] Mats Hillert and Magnus Jarl. A model for alloying in ferromagnetic metals. *Calphad*, 2 (3):227–238, 1978.

[135] Ling Fan, Chen Shen, Kun Hu, Huashan Liu, and Hongbin Zhang. Dft calculations and thermodynamic re-assessment of the fe-y binary system. *Journal of Phase Equilibria and Diffusion*, 42(3):348–362, 2021.

[136] Malcolm W Chase et al. Nist-janaf thermochemical tables. *Journal of physical and chemical reference data*, 28:1951, 1998.

[137] Igor A Abrikosov, AV Ponomareva, Peter Steneteg, SA Barannikova, and Björn Alling. Recent progress in simulations of the paramagnetic state of magnetic materials. *Current Opinion in Solid State and Materials Science*, 20(2):85–106, 2016.

[138] George H. Vineyard. Frequency factors and isotope effects in solid state rate processes. *Journal of Physics and Chemistry of Solids*, 3(1):121–127, 1957. ISSN 0022-3697. doi: https://doi.org/10.1016/0022-3697(57)90059-8. URL `https://www.sciencedirect.com/science/article/pii/0022369757900598`.

[139] Lawrence Himmel, RF Mehl, and C E_ Birchenall. Self-diffusion of iron in iron oxides and the wagner theory of oxidation. *Jom*, 5(6):827–843, 1953.

[140] Karl Hauffe. *Oxidation of metals*. Springer Science & Business Media, 2012.

[141] Stefan Grimme, Jens Antony, Stephan Ehrlich, and Helge Krieg. A consistent and accurate ab initio parametrization of density functional dispersion correction (dft-d) for the 94 elements h-pu. *The Journal of chemical physics*, 132(15), 2010.

[142] Andreas Heyden, Alexis T Bell, and Frerich J Keil. Efficient methods for finding transition states in chemical reactions: Comparison of improved dimer method and partitioned rational function optimization method. *The Journal of chemical physics*, 123(22), 2005.

[143] Federico Calle-Vallejo. The abc of generalized coordination numbers and their use as a descriptor in electrocatalysis. *Advanced Science*, 10(20):2207644, 2023.

[144] Zhaohui Zhou, Pengju Huo, Liejin Guo, and Oleg V Prezhdo. Understanding hematite doping with group iv elements: a dft+ u study. *The Journal of Physical Chemistry C*, 119 (47):26303–26310, 2015.

[145] Alfonso Baldereschi. Mean-value point in the brillouin zone. *Physical Review B*, 7(12): 5212, 1973.

[146] RS Hixson, MA Winkler, and ML Hodgdon. Sound speed and thermophysical properties of liquid iron and nickel. *Physical Review B*, 42(10):6485, 1990.

[147] YE Lee and DR Gaskell. The densities and structures of melts in the system cao-"feo"-sio2. *Metallurgical transactions*, 5(4):853–860, 1974.

[148] Florian Müller-Plathe. A simple nonequilibrium molecular dynamics method for calculating the thermal conductivity. *The Journal of chemical physics*, 106(14):6082–6085, 1997.

[149] Tatiana Otroshchenko, Guiyuan Jiang, Vita A Kondratenko, Uwe Rodemerck, and Evgenii V Kondratenko. Current status and perspectives in oxidative, non-oxidative and co 2-mediated dehydrogenation of propane and isobutane over metal oxide catalysts. *Chemical Society Reviews*, 50(1):473–527, 2021.

[150] Gerhard Ertl, Helmut Knözinger, Jens Weitkamp, et al. *Handbook of heterogeneous catalysis*, volume 2. VCH Weinheim, 1997.

[151] Randy D Cortright, Josephine M Hill, and James A Dumesic. Selective dehydrogenation of isobutane over supported pt/sn catalysts. *Catalysis Today*, 55(3):213–223, 2000.

[152] Hien N Pham, Jesper JHB Sattler, Bert M Weckhuysen, and Abhaya K Datye. Role of sn in the regeneration of pt/γ-al2o3 light alkane dehydrogenation catalysts. *ACS catalysis*, 6(4): 2257–2264, 2016.

[153] Moritz Wolf, Narayanan Raman, Nicola Taccardi, Marco Haumann, and Peter Wasserscheid. Coke formation during propane dehydrogenation over ga- rh supported catalytically active liquid metal solutions. *ChemCatChem*, 12(4):1085–1094, 2020.

[154] Narayanan Raman, Sven Maisel, Mathias Grabau, Nicola Taccardi, Jonas Debuschewitz, Moritz Wolf, Haiko Wittkamper, Tanja Bauer, Mingjian Wu, Marco Haumann, et al. Highly effective propane dehydrogenation using ga–rh supported catalytically active liquid metal solutions. *ACS catalysis*, 9(10):9499–9507, 2019.

[155] Moritz Wolf, Narayanan Raman, Nicola Taccardi, Raimund Horn, Marco Haumann, and Peter Wasserscheid. Capturing spatially resolved kinetic data and coking of ga–pt supported catalytically active liquid metal solutions during propane dehydrogenation in situ. *Faraday discussions*, 229:359–377, 2021.

[156] Moritz Wolf, Ana Luiza de Oliveira, Nicola Taccardi, Sven Maisel, Martina Heller, Sharmin Khan Antara, Alexander Søgaard, Peter Felfer, Andreas Görling, Marco Haumann, et al. Dry reforming of methane over gallium-based supported catalytically active liquid metal solutions. *Communications Chemistry*, 6(1):224, 2023.

[157] Günther Rupprechter. Popping up to the surface. *Nature Chemistry*, 9(9):833–834, 2017.

[158] JM Herman, APAF Rocourt, PJ Van den Berg, PJ Van Krugten, and JJF Scholten. The industrial hydroformylation of olefins with rhodium-based supported liquid phase catalyst (slpc): Part vi. general predesign of a large-scale slpc plant for the hydroformylation of propylene. *The Chemical Engineering Journal*, 35(2):83–103, 1987.

[159] Tanja Bauer, Sven Maisel, Dominik Blaumeiser, Julia Vecchietti, Nicola Taccardi, Peter Wasserscheid, Adrian Bonivardi, Andreas Gorling, and Jorg Libuda. Operando drifts and dft study of propane dehydrogenation over solid-and liquid-supported ga x pt y catalysts. *ACS catalysis*, 9(4):2842–2853, 2019.

[160] Narayanan Raman, Moritz Wolf, Martina Heller, Nina Heene-Wurl, Nicola Taccardi, Marco Haumann, Peter Felfer, and Peter Wasserscheid. Gapt supported catalytically active liquid metal solution catalysis for propane dehydrogenation–support influence and coking studies. *ACS catalysis*, 11(21):13423–13433, 2021.

[161] Georg Kresse and Jürgen Hafner. Ab initio molecular dynamics for liquid metals. *Physical review B*, 47(1):558, 1993.

[162] Ryosuke Jinnouchi, Jonathan Lahnsteiner, Ferenc Karsai, Georg Kresse, and Menno Bokdam. Phase transitions of hybrid perovskites simulated by machine-learning force fields trained on the fly with bayesian inference. *Physical review letters*, 122(22):225701, 2019.

[163] Shuichi Nosé. A unified formulation of the constant temperature molecular dynamics methods. *The Journal of chemical physics*, 81(1):511–519, 1984.

[164] Olga Chalykh, Mikhail Polovinkin, Dmitry Korogod, Nikita Rybin, and Alexander Shapeev. Active learning and explicit electrostatics enable accurate modeling of electrolytes. *arXiv preprint arXiv:2510.03479*, 2025.

[165] Conrad Book. *Title of Book*. Publisher, Address, 2nd edition, 2021.

[166] Anna Journal. Title of article. *Name of Journal*, 6(3–4):371–378, 2000. doi: 10.1017/S1754078714006221.

[167] Haijun Pan, Xiangying Meng, Dongyan Liu, Song Li, and Gaowu Qin. (ti/zr, n) codoped hematite for enhancing the photoelectrochemical activity of water splitting. *Physical Chemistry Chemical Physics*, 17(34):22179–22186, 2015.

[168] Frank Jensen. *Introduction to computational chemistry*. John wiley & sons, 2017.

[169] Jianmin Tao, John P Perdew, Viktor N Staroverov, and Gustavo E Scuseria. Climbing the density functional ladder: Nonempirical meta–generalized gradient approximation designed for molecules and solids. *Physical Review Letters*, 91(14):146401, 2003.

[170] Jianwei Sun, Adrienn Ruzsinszky, and John P Perdew. Strongly constrained and appropriately normed semilocal density functional. *Physical review letters*, 115(3):036402, 2015.

[171] Albert P Bartók and Jonathan R Yates. Regularized scan functional. *The Journal of chemical physics*, 150(16):161101, 2019.

[172] James W Furness, Aaron D Kaplan, Jinliang Ning, John P Perdew, and Jianwei Sun. Accurate and numerically efficient r2scan meta-generalized gradient approximation. *The journal of physical chemistry letters*, 11(19):8208–8215, 2020.

[173] A. P. Thompson, H. M. Aktulga, R. Berger, D. S. Bolintineanu, W. M. Brown, P. S. Crozier, P. J. in 't Veld, A. Kohlmeyer, S. G. Moore, T. D. Nguyen, R. Shan, M. J. Stevens, J. Tranchida, C. Trott, and S. J. Plimpton. LAMMPS - a flexible simulation tool for particle-based materials modeling at the atomic, meso, and continuum scales. *Comp. Phys. Comm.*, 271:108171, 2022. doi: 10.1016/j.cpc.2021.108171.